**A final report for the Phase-II SBIR project**

**Physical Model Development and Benchmarking for MHD Flows in Blanket Design**

**DOE Contract # DE-FG02-04ER83977**

submitted by

Ramakanth Munipalli, P.-Y. Huang, Carlos Chandler, Chris Rowell
HyPerComp Inc.,

Mingjiu Ni, Neil Morley, Sergey Smolentsev, Mohamed Abdou
TEXCEL, UCLA

## Abstract

An advanced simulation environment to model incompressible MHD flows relevant to blanket conditions in fusion reactors has been developed at HyPerComp in research collaboration with TEXCEL. The goals of this phase-II project are two-fold: The first is the incorporation of crucial physical phenomena such as induced magnetic field modeling, and extending the capabilities beyond fluid flow prediction to model heat transfer with natural convection and mass transfer including tritium transport and permeation. The second is the design of a sequence of benchmark tests to establish code competence for several classes of physical phenomena in isolation as well as in select (termed here as "canonical",) combinations. No previous attempts to develop such a comprehensive MHD modeling capability exist in the literature, and this study represents essentially uncharted territory. During the course of this Phase-II project, a significant breakthrough was achieved in modeling liquid metal flows at high Hartmann numbers. We developed a unique mathematical technique to accurately compute the fluid flow in complex geometries at extremely high Hartmann numbers (10,000 and greater), thus extending the state of the art of liquid metal MHD modeling relevant to fusion reactors at the present time. These developments have been published in noted international journals. A sequence of theoretical and experimental results was used to verify and validate the results obtained. The code was applied to a complete DCLL module simulation study with promising results.

**Table of contents**



**Appendices**

## 1. List of Symbols

φ .....Level set
φ .....Electric potential
t .....Time
T .....Temperature
$\vec{V}$ .....Velocity
ρ .....Density
p .....Pressure
B .....Magnetic Field
$\mu_m$ .....Permeability
$\mu_v$ .....Viscosity
k .....Thermal conductivity
g .....Acceleration due to gravity
Gr .....Grashof number
Ha .....Hartmann number
Pe .....Peclet number
Pr .....Prandtl number
Ra .....Rayleigh number
Re .....Reynolds number
$Re_m$ .....Magnetic Reynolds number
Fr .....Froude number
J .....Electric current density
E .....Electric field
σ .....Electrical conductivity
τ .....Shear stress
$u_i$, .....velocity component
Ω .....Control volume
∂Ω .....Control volume boundary
Cp .....Specific heat capacity
n .....normal vector or direction
c .....wall conductance
t .....conducting wall thickness
$\nu$ .....kinematic viscosity
$\nu_t$ .....eddy viscosity
Pr .....Prandtl number
$B_{0i}$ .....applied magnetic field
$N$ interaction parameter ($= Ha^2 / \mathrm{Re}$)

$\boldsymbol{Gr} = \dfrac{\boldsymbol{L}^3 \rho^2 \boldsymbol{g} \eta \Delta \boldsymbol{T}}{\mu^2}$ Grashof number

$\boldsymbol{Ha} = \boldsymbol{BL}\sqrt{\dfrac{\sigma}{\mu}}$ Hartmann number

$\boldsymbol{Nu} = \dfrac{\boldsymbol{q}_w \boldsymbol{L}}{\boldsymbol{k}\left(\boldsymbol{T}_w - \boldsymbol{T}_{ref}\right)}$ Nusselt number

$\boldsymbol{Pe} = \dfrac{\mu_{ref} \boldsymbol{L} \boldsymbol{c}_p}{\boldsymbol{k}}$ Peclet number

$\mathrm{Pr} = \dfrac{\mu \boldsymbol{c}_p}{\boldsymbol{k}}$ Prandtl number

$\mathrm{Re} = \dfrac{\rho U L}{\mu}$ Reynolds number

## 2. A summary of the Phase-II project

We are developing a high performance computing framework, wherein incompressible MHD problems may be studied in a self-consistent manner in a reasonable time-frame. Recent advances in models for turbulence, natural convection and Tritium transport are generalized to a multi-dimensional, arbitrary geometry situation. In order to perform a methodical benchmarking of the numerics, we have selected key results from the literature in each relevant physical discipline, and form unit problems to which they are applicable.

A sequence of elementary benchmark problems were studied for single phase MHD and strategies were developed to overcome certain key limitations in HyPerComp Incompressible MHD solver for Arbitrary Geometries (HIMAG). Some of these methods are equally applicable to a wider set of MHD codes. Applications to DCLL geometries were successfully made. Graphical interfaces have been developed to assist a novice user in setting up canonical tests, and thus in learning the code. A preliminary training session was conducted and a series of notes and documentation for the code were prepared. Various publications have appeared containing the approaches developed under this SBIR in DCLL related modeling, benchmarking and analysis. In Ni et al [37, 39] we describe canonical benchmark problems in free surface and single phase flow (related to DCLL) MHD and results from HIMAG. In Ni et al [38] we present a unique numerical method developed under this SBIR project which enables for the first time in literature, high Hartmann number computations in complex geometries. Applications to inlet manifolds (Morley et al [30]), free surface flows (Narula et al [35]) and a broad overview of blanket modeling (Smolentsev et al [50]) have been published.

The primary goals of the phase-II research were: 1) Incorporating recent advances in MHD fluid flow, eg. turbulence, heat transfer including natural convection, and mass transfer including tritium transport and permeation, 2) Perform a well designed set of validation exercises to enhance confidence in the accuracy of the code's predictive capability, and 3) Transition HIMAG into a physical module that can be included in the Virtual TBM as it develops, with this module serving the function of predicting MHD fluid flow and heat and mass transfer. In this report, we first describe the challenges that were overcome, followed by a detailed description of technical accomplishments in phase-II and Phase-I.

## 3. Modeling High Hartmann Number MHD: Significance and Challenges

There are critical aspects of three dimensional magnetohydrodynamics (MHD) flow fields in complex geometries (including conducting walls and multiple fluids in conduits,) which are beyond popular engineering intuition and convenient analysis, thus requiring high fidelity numerical tools. HyPerComp is developing a simulation environment to study flows of this nature, primarily driven by the needs of the fusion community in developing blanket modules for major international projects such as ITER. Tentatively named as HIMAG (**H**yPerComp **I**ncompressible **M**HD solver for **A**rbitrary **G**eometry,) this code is able to model (at the present time,) multiphase laminar MHD flows using unstructured/hybrid meshes across parallel processors, thus enabling the computation of fairly large scale and complex flows in acceptable wall-clock time.

In our work, we sought to extend the scope of HIMAG by incorporating models of newer and critical physical phenomena, as well as improve user confidence in the solver by designing a sequence of canonical benchmarks. Our intention then, was to enable the code to participate in a multi-physical simulation suite, referred to here as a Virtual Test Blanket Module (VTBM) simulation environment. It is hoped that such an environment will be a convenient and economical means to simulate the performance of test blanket module designs being performed for various reactor concepts, particularly the international project ITER (see Abdou et al[2] for a contemporary account of this research).

In this chapter we present first the goals of a virtual test blanket module and an outline of a possible design for such a concept. We then present a summary of our interest in developing advanced physics for MHD flows relevant to test blanket modules, and a protocol to validate these modules by an appropriate choice of benchmark problems. Indeed, the phenomena of natural convection and high Hartmann number turbulence have attained prominence in blanket studies very recently, and by all indications, seem to have a tremendous impact on conceptual design. A comprehensive code development activity at the scale investigated here has not been carried out hitherto, and there is to date, a lack of a well accepted set of benchmark problems in this area. The design of unit problems in multi-physical MHD flows is of contemporary interest, as expressed in various survey articles in the literature (Morley et al[31], Kirilov et al[25], Brooks et al[8], and Molokov et al[28]).

## 3.1 Multiphysics in blanket modeling and the development of a VTBM

International Thermonuclear Experimental Reactor (ITER) is an international project that aims to test burning plasma physics in a prototypical fusion reactor environment. One of the objectives of ITER is to test and evaluate blanket modules. Test Blanket Modules (TBM) from various international collaborating groups will be inserted in three specifically designed ports (see Fig [1]). The primary functions of the blanket are to extract heat at high temperatures and breed tritium at a rate sufficient for tritium self-sufficiency. The blanket includes various materials and interfaces: breeder, coolant, structure, neutron multiplier, and depending on the blanket concept, thermal and MHD insulators. The blanket is exposed to surface heat flux from plasma radiation and neutrons that interact with materials generating volumetric heating and causing radiation effects. Many technical disciplines are involved in analysis and design of the blankets, for example, neutronics, fluid mechanics, heat transfer, structural mechanics, chemistry, materials science and plasma-material interactions.

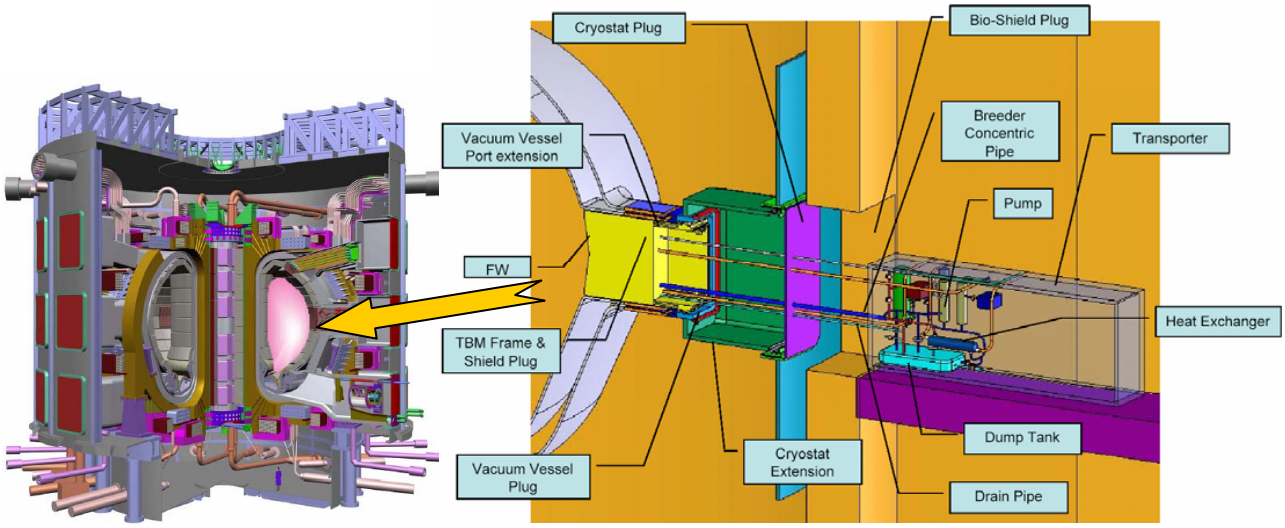


**Figure 1:** Conceptual sketch of ITER with detail showing a test port and TBM assembly

The actual behavior of the TBM in a fusion environment is indeed extremely complex. Neutron and other forms of radiation emerging from the plasma core of the reactor are incident upon the first wall – TBM assembly. The effects of plasma radiation and fusion neutrons include heating of the components; production, transport and permeation of Tritium; and global deformation of the structure. The presence of 3-component magnetic fields results in additional important effects. Structural deformation in its turn influences flow and heat transfer, and results in strong coupling of physics. The flowing liquid metal breeder experiences magnetohydrodynamic (MHD) forces that are felt by the structure in the form of hoop stresses. Natural convection processes result in property gradients that influence heat distribution

and species (neutron, Tritium) concentrations. All of these processes are essentially developed in time to steady or quasi-steady state. The response of the TBM to unsteady loads can be often rather severe. Plasma disruptions can produce very strong eddy currents and electromagnetic forces that can significantly warp and cause permanent damage to the structure.

HyPerComp has an active interest in developing a Virtual Test Blanket Module (VTBM) program that can interface these various physics in a large-scale computational test facility. The idealized functioning of a VTBM environment is depicted in fig [2]. A conceptual TBM design is analyzed by an integrated computer model and its performance parameters are deduced. Several choices are typically made through the course of the simulation, particularly concerning the fidelity of the numerical models used, and the level of accuracy sought in high fidelity models. As described by Kingsley et al[24] and Townsend et al[56], the management of multi-scale, multi-fidelity and multi-disciplinary simulations such as these can benefit from effective software engineering practices. There are mathematical constraints that the integrated code must satisfy, as discussed by Farhat et al[12], that will satisfy conservation of various quantities when transferring across models and grids. Samareh et al[46] have presented techniques by which data transfer across physical phenomena may be performed using simple transformation metrics. The intent of this project is to transition HIMAG into a physical module that can support the VTBM as it develops.

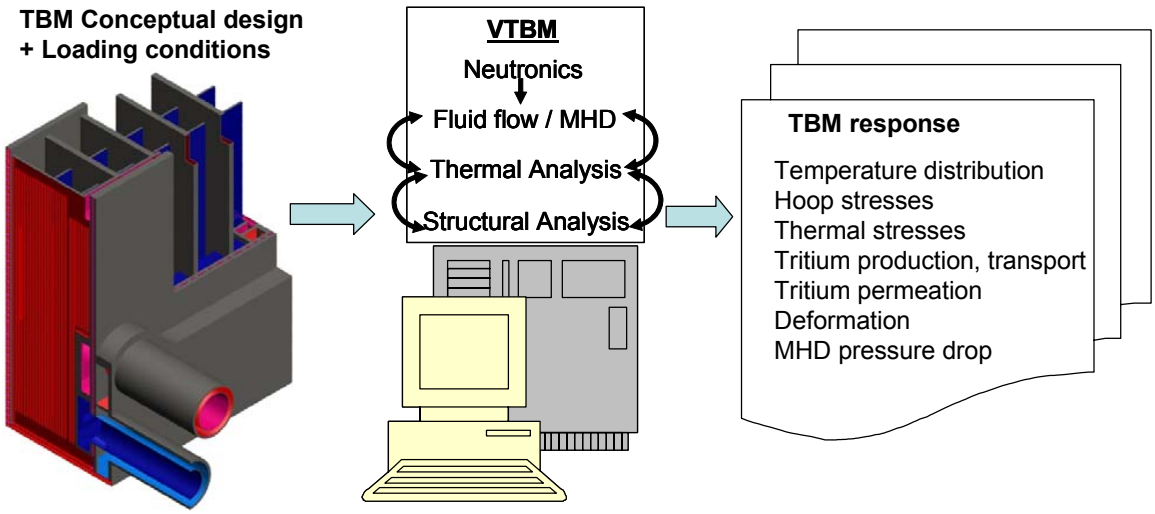


**Figure 2:** A simplified representation of the function of the Virtual TBM

## 3.2 HIMAG: Code status

HyPerComp is developing a unique computational environment named HIMAG (**H**yPerComp **I**ncompressible **M**HD solver for **A**rbitrary **G**eometries,) intended as a design tool for incompressible (high Hartmann number) MHD flows with free surfaces for complex geometries on parallel computers. HIMAG has inherited a parallel unstructured code environment from an existing electromagnetics solver, and has essentially replaced the solver and code integration strategies. In its present form, the following capabilities are available in HIMAG:

- Three dimensional incompressible flow solver (2nd order accurate in space and time)
- Free surface capture using level set technique
- Arbitrary mesh structure (hex / tetrahedral / prismatic cells)

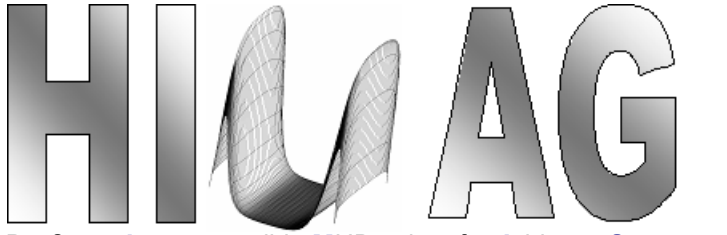

- Well tested parallel code environment
- Electric potential as well as induced magnetic field formulations for MHD
- Point implicit scheme, solved in an iterative manner
- Multiple strategies to account for mesh skewness (non-orthogonality)
- Ability to include multiple solid walls of different conductivity

Besides the development of the solver, significant effort was expended in studying alternate MHD models (based on induced magnetic field and induced current,) to overcome certain limitations of the Inductionless approach. These limitations tend to be chiefly numerical and become progressively more prominent at higher Hartmann numbers and magnetic field intensities. Much experience in the simulation of free surface flows on unstructured meshes has been gained. Parallel execution of the code for problems involving solid walls has been initiated and applied to several cases. High Hartmann number (up to 10,000) single phase MHD flows were studied. Very close to linear scaling of performance with respect to computer nodes, has been attained for large problems when HIMAG is run in the parallel mode.

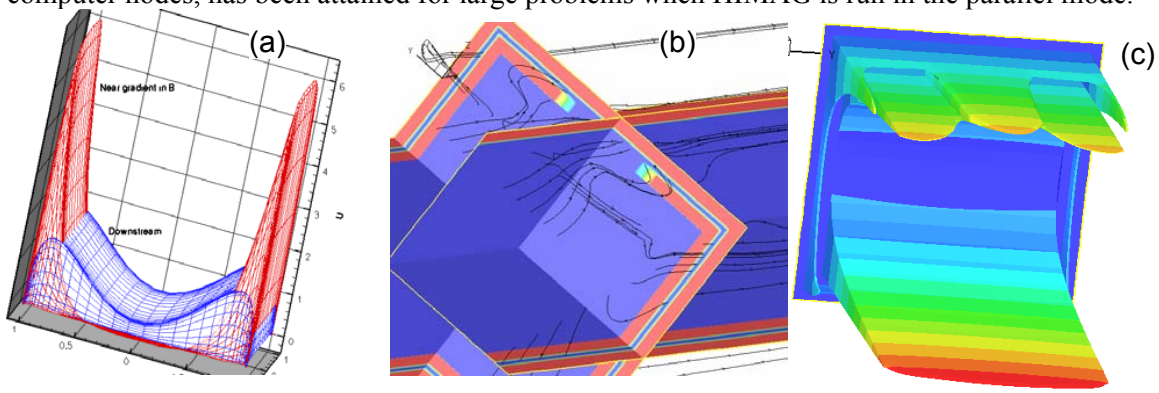


**Figure 3:** Preliminary MHD modeling results from HIMAG for fusion relevant flows. From left, (a) High Hartmann number closed channel flow; (b) and (c) Pb-Li coolant with Si-C flow channel insert encased in a steel pipe (b) shows streamlines in the side-channels, and (c) shows velocity profile at a cross section

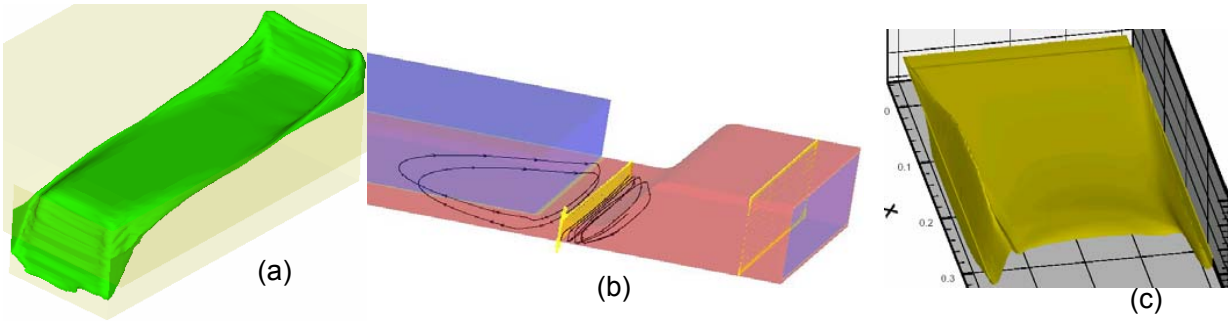


**Figure 4**: Free surface MHD simulations from HIMAG. (a) Electromagnetic sloshing of liquid metal exposed to plasma, (b)Current paths in NSTX liquid metal film injection channel, and (c) Computed MHD altered free surface shape corresponding to the MTOR experiments at UCLA

HIMAG is able to model complex geometries, such as curved surfaces, multiple solid obstacles, sharp corners, etc., by using arbitrary mesh topologies (tetrahedral, hexahedral elements). It is able to economically resolve thin Hartmann layers and cracks in insulated walls using appropriate mesh-blocking strategies. So far, the code has shown great potential to overcome basic technological hurdles such as high Hartmann numbers and current leakage through extremely slender cracks in wall insulation.

The code is built on a robust iterative implicit solver, and can be run in parallel across a network of processors, and is primarily intended for use in PC based clusters running LINUX. With the low cost of building and operating these clusters, this is proving to be an inexpensive design strategy for researchers

and engineers in this area. A network of 200 PC nodes at processor speeds of about 2 GHz across gigabit Ethernet is currently available for this research at UCLA. This will provide the ability to simulate very large scale problems such as encountered in real life, involving tens of millions of mesh points. Figures [3] and [4] show sample recent applications of HIMAG.

### 3.3 Enhanced operability of HIMAG and the role of methodical benchmarking

With the increased global participation in the ITER project in recent times, there has been a concerted effort to focus studies and narrow down blanket design choices to a few that are most likely to succeed. Fundamental research in the MHD aspects of liquid breeders in the European HCLL and the US DCLL concepts have revealed some critical aspects that can influence performance predictions significantly. Among these are:

(1) Wall conductivity and imperfections in insulation: Small cracks in insulating coatings have been estimated to cause large changes in pressure gradients, potentially affecting concept feasibility. (Ref. Sze et al)

(2) Pressure and electric current distributions in the flow channel insert (FCI) concept: Channel inserts made of slotted Silicon-Carbide conduits encased by Ferritic Steel outer walls have been proposed as means to overcome partially the large MHD-based pressure gradients. The low strength of the SiC structure is offset by pressure equalization slots which essentially transfer the mechanical stresses to the Steel casing. These designs involve rather high Hartmann numbers, and the complexity in the structure makes the computations rather expensive and complex. (Ref, Smolentsev et al [50])

(3) Heat transfer estimates in dual-cooled structures: Multiple conduits are provided for the flow of Helium, and liquid metal (PbLi) in the liquid breeder concept. Modeling these conduits simultaneously can be a challenge to codes that are based on the "single fluid" assumption. (We note that by construction, HIMAG can handle multiple solid materials and two fluids.)

(4) Turbulence models: A range of turbulence models (see Moreau et al, Thess et al, Smolentsev et al,) have been developed in the past decade to study turbulent flow typically in fully developed channels. Models range from Reynolds Averaged Navier-Stokes (RANS) equations with two-equation models, to algebraic models based on high Hartmann number considerations. Much progress has been reported in Direct numerical simulations and Large eddy simulations of MHD channel flows. Albeit their expense, these studies have led to the development of better turbulence models. It is believed that turbulence models are essential in modeling forced convection, and even thermal convection in MHD flows relevant to blanket conditions.

(5) Natural convection and flow stability: It has been estimated that in DCLL and HCLL concepts, natural convection can result in flow speeds that are several times the forced convection speeds (Authie et al, Buhler et al). There is an associated stability concern in these flows, wherein the convective flow exhibits oscillations at lower Hartmann numbers, and in directions transverse to Hartmann walls.

(6) Ferromagnetic effects of wall materials: Ferritic steel is used in various concepts as the principal load bearing material that are able to bear the hoop-stresses caused by the large pressure gradients caused by MHD. A model for MHD including ferromagnetic walls presented by Buhler et al [10] is being presently incorporated in HIMAG. Buhler acknowledges the concern that a complete mathematical representation of ferromagnetic material properties is virtually impossible, particularly when dealing with induced currents. Under conditions relevant to the present application, the effects of hysteresis are neglected. The formulation differs from the more conventional models of the induced magnetic field by introducing a field dependent magnetic

permeability when the applied field $\boldsymbol{B_0}$ is less than a certain critical value $\boldsymbol{M_s}$. For a solid wall, we may write:

$$\boldsymbol{J} = \frac{1}{\mathrm{Re}_m}\nabla\times\frac{\boldsymbol{B}}{\mu_r},\ \text{where}\ \frac{1}{\mu_r} = \frac{\boldsymbol{B}}{\boldsymbol{B}_0} = \begin{cases} \mu_{r,1}^{-1} & \text{Ferromagnetic regime, B} \le \boldsymbol{M_s} \\ 1 - \dfrac{\boldsymbol{M_s}}{\boldsymbol{B}} & \text{Saturated regime, B} >> \boldsymbol{M_s} \end{cases}$$

The quantity is $\mu_{r,1}$ is obtained from curve-fits or tabulated data. The most important ferromagnetic effect that can be encountered is that of magnetic field shielding by the structure, which can cause an incorrect estimate of the effective magnetic field felt by the liquid metal.

(7) Tritium inventory and permeation: The liquid metal used in blankets serves two major purposes. The first is to convect heat and radiation away for wall protection and power generation. The second is to act as a "breeder," whereby Lithium present in the liquid metal reacts with the incoming neutron radiation to form Tritium, which may then be regeneratively used as fuel in the reactor. Tritium permeation is a very important safety issue. Modeling of it, is therefore crucial in the reactor. This modeling is possible by extending the methodology for predicting mass transfer.

The current state of the art in fusion relevant MHD modeling, as reviewed by Reed and Molokov[28], Kirillov et al[25], Morley et al[31], faces serious limitations in the range of attainable Hartmann numbers (not larger than $10^3$ usually reported for 3D computations,) free surface modeling, and the treatment of walls in complex geometries, while all of the items 1-7 mentioned above represent a new breed of physical issues that must be addressed. Items 3,4,5 and 7 are studied here as code enhancements to HIMAG. Other items are being investigated in a separate contract. The Phase-II project has resulted in a code that is rather unprecedented in the history of liquid metal MHD, and has demonstrated flow solutions that have been hitherto not conceived.

The direction we choose to adopt for the development of HIMAG is to prepare the code into a series of modules to be integrated eventually into a VTBM.

### 3.4 Development of a canonical approach to MHD

This component of the proposed work is an outcome of recent concerns in developing appropriate benchmark and canonical problems in incompressible MHD in which various physical phenomena may be numerically simulated in isolation or in user-selected combinations. There is a massive wealth of literature pertaining to idealized situations in MHD flows, while their actual relevance to non-ideal situations is not always very clear. By the term "non-ideal" we refer to attributes such as:

(1) Complex geometry with non-smooth and multiply connected domain boundaries,
(2) Three dimensional fields with strong gradients in multiple directions,
(3) Developing flows in which the steady state (fully developed) flow solution is non-unique,
(4) Multi-scale processes such as turbulence with natural convection, tritium transport and heat transfer,
(5) Problems in which domain boundaries may be changing (deforming structure).

Indeed, the dire lack of test data or a commonly accepted set of validation data in such flows reduces the user community's faith in complex flow modeling software, and our ability to interpret and scale results obtained from simulations. Recent reviews of the present status of modeling and experiments in liquid metal MHD pertaining to fusion and metallurgy were made by Morley et al.[31], Kirillov et al.[25], and Davidson[11]. While lamenting upon the lack of reliable computational or analytical techniques for flow prediction for realistic problems[11], the need for modeling complex geometry and imperfect wall insulations[25], and, for a substantial benchmarking process in experiments and computations[31] has been identified by these authors. We believe that this Phase-II project addressed this need substantially.

## 4. Technical Description of Phase-II Accomplishments

The investigations in this SBIR have resulted in the development and application of mainstream CFD techniques in incompressible MHD, as evidenced by the unique abilities to model all of the following features: (References [36-39] may be consulted for a detailed description of the technical approach.)

1. High Hartmann Number Flows: Canonical Problems on Arbitrary Meshes
2. Comparison against experiments (ALEX)
   - Square and circular ducts and the effect of pressure-taps
3. Applications to the Dual Coolant Lead-Lithium (DCLL) blanket concept
   - Study of Flow Channel Inserts
   - Entry Effects
   - Increase in flow development length
   - Divided Flow Channel Insert
   - Inlet Manifold
4. Tritium permeation and transport
5. Summary of canonical testing approach from Phase-I (in section-5)

### 4.1 High Hartmann Number Flows: Canonical Problems on Arbitrary Meshes

HIMAG has been extremely successful at modeling problems that were not even attempted thus far using full flow-field solutions. Semi-analytical approaches based on core-flow assumptions, and various reduced dimension models are in popular usage. However, none of these methods will be able to provide a complete, self-consistent solution to MHD flows in realistic geometries, to the extent that even the relevant qualitative flow features are largely unknown prior to gaining more knowledge via detailed testing. The primary issue facing computer simulations based on full Navier-Stokes equations with appropriate MHD effects, as discussed in section [3], revolve around the extreme demands placed on the accuracy of numerical schemes in fusion relevant MHD, and the computational time that can run into several months at times for realistic problems. Given that there is an enormous scope for applications and improvements in contemporary numerical methods in this area, we set out to improve upon the code structure in HIMAG. HIMAG has thus far been applied to internal and external flows. Figure [5] in the next page shows some highlights from verification and validation studies performed using HIMAG on a few interesting problems.

Figures [ 5a, 5b] show flow solutions from square and circular ducts with conducting walls. Very encouraging comparisons with analytical solutions were obtained for high Hartmann number (10,000) flow in the square duct, compared here across 2-D, 3-D and analytical solutions. Severely stretched meshes were used, thus making the total number of cells fairly affordable (typically, 40x40 cells in a square duct cross section, even at extreme Hartmann numbers). The circular duct solution in [ 5b] uses a polar grid (which is numerically non-orthogonal) and corrections for mesh skewness. Figures [ 5c,d] show comparisons of numerical solutions from HIMAG against experiments made by Reed et al [43]. These, again, are highly encouraging, and indeed represent the first time a full-CFD approach has been used to model such a flow at high MHD interaction conditions. Figure [5e] shows a Hartmann number 1,000 flow modeled in a square duct with conducting walls, demonstrating the flexibility of HIMAG to model a computational domain with non-hexahedral cells at high Ha, and still recover accurate solutions.

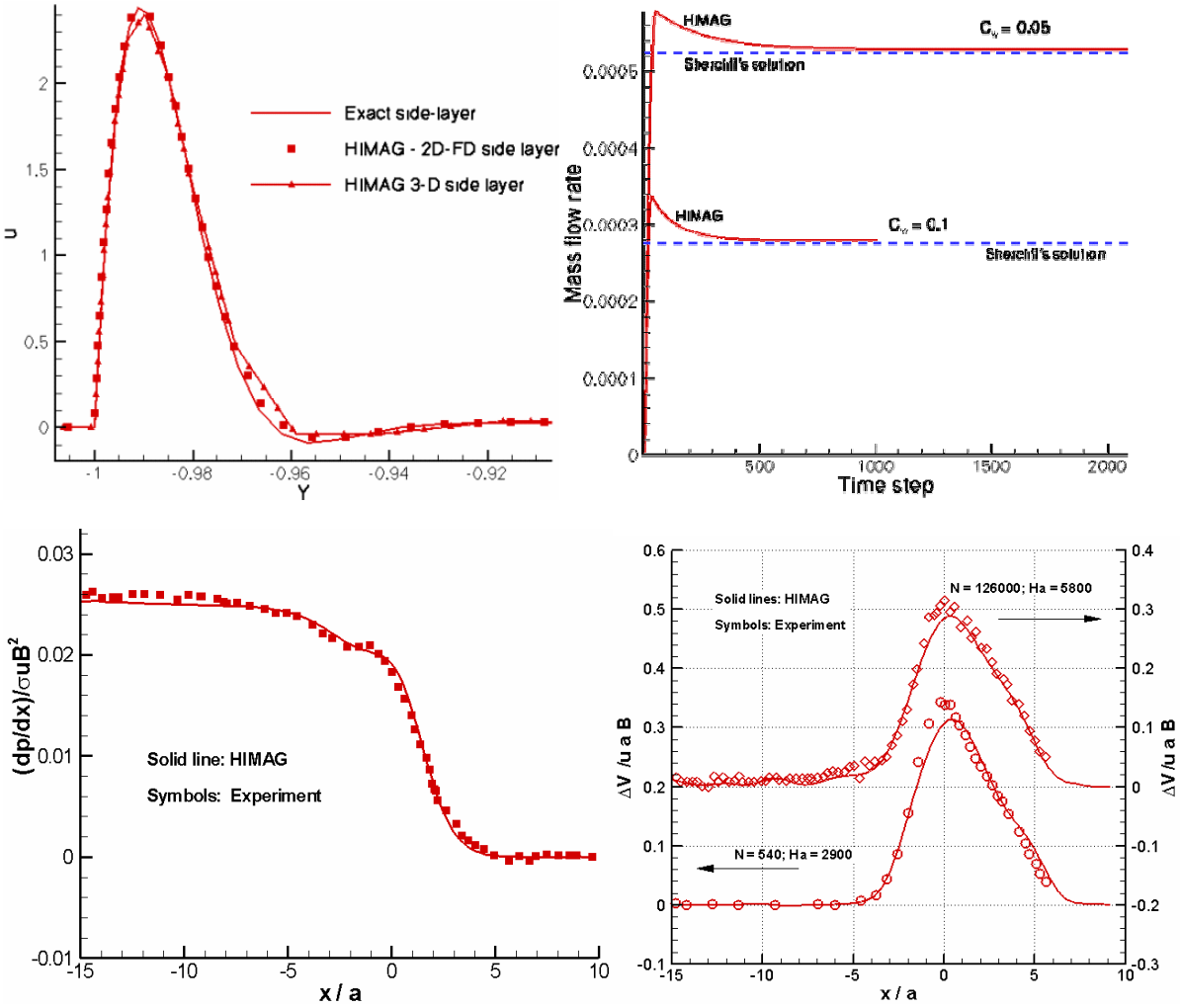


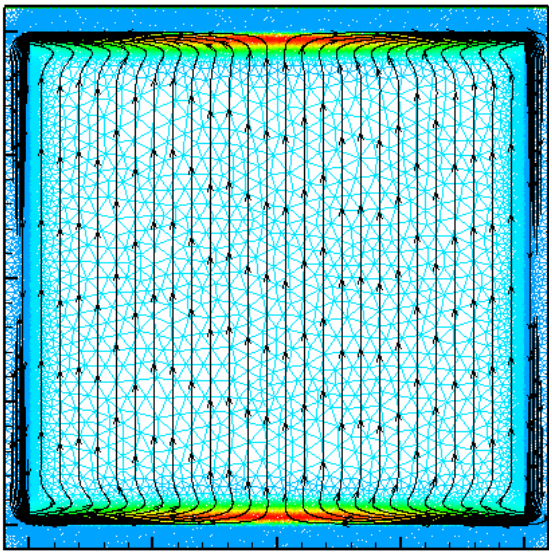

**Figure 5:** (a, top-left) Side-layer velocity in Ha=10,000 flow in a rectangular duct computed by HIMAG, comparing theory, 2-D and 3-D computations, (b,top-right) Mass flow rate in Ha=1,000 flow in a circular duct, comparing theory and HIMAG results, (c, above left) Pressure gradient in a circular duct flow at Ha=6,640 comparison with measurements, (d. above right) Hartmann-wall to side-wall electric potential drop, compared with experiments in a square duct, (e, left) Ha = 10,000 flow in a square duct computed with a completely unstructured mesh

### 4.2 Comparison against experiments (ALEX[43])

We attempted to validate HIMAG against the experimental data where experimental studies and core-flow computations were used in understanding liquid metal flow in conducting ducts with a gradient in applied magnetic field. Cases studied were at high Hartmann numbers and displayed strong non-uniformities and measurable three-dimensional features. Such comparisons with a full Navier-Stokes solver have hitherto not been made in the literature due to limitations on MHD solvers, particularly on curved geometry such as the cylindrical duct.

**Square duct**

We begin by describing the flow in a duct with a square cross section. Figure [6] shows a summary of geometry and flow parameters.

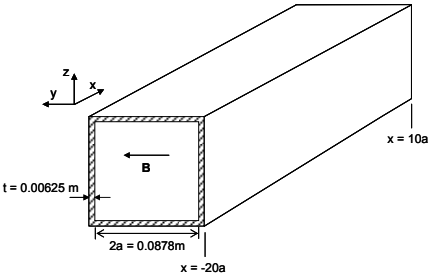


| Case-1 | Case-2 |
|---|---|
| $B_{max}$ = 2.252 T | $B_{max}$ = 1.1 T |
| Ha = 5800 | Ha = 2900 |
| N = 126000 | N = 540 |
| Re = 266.984 | Re = 15574.07 |
| U = 0.005776 m/s | U = 0.337 m/s |
| $c_w$ = 0.08 | $c_w$ = 0.075 |

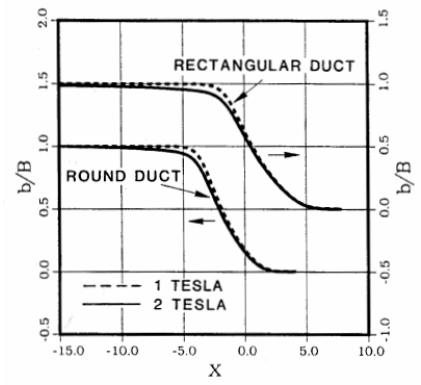


$$\rho = 865\,\mathrm{kg/m^3},$$
$$a = 0.0439\,m,$$
$$\sigma = 2.82754\times10^{6}\,/(\Omega m),$$
$$\mu = 8.2175\times10^{-4}\,\frac{kg}{m\cdot s},$$
$$c_w \approx 0.075,$$
$$t_w = 6.2511\times10^{-3}\,m,$$
$$\sigma_w = 1.51479\times10^{6}\,/(\Omega m)$$

**Figure 6**: Clockwise from top left (a) Channel geometry, (b) Flow parameters, (c) Applied magnetic field distribution, and (d) Physical properties used, and (e) below, streamlines computed by HIMAG

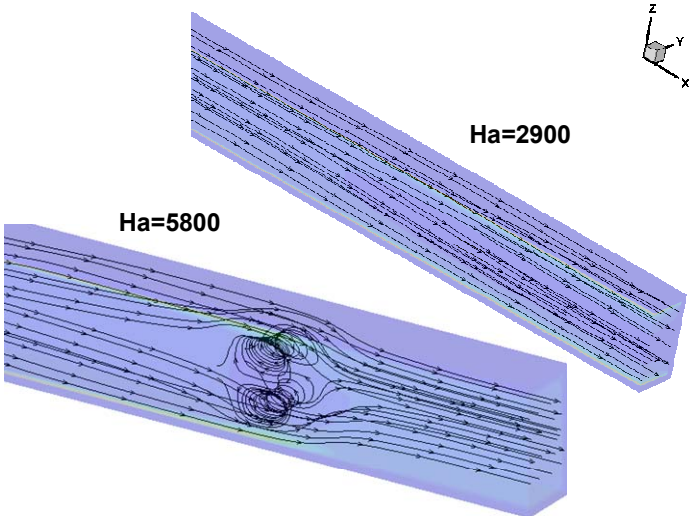

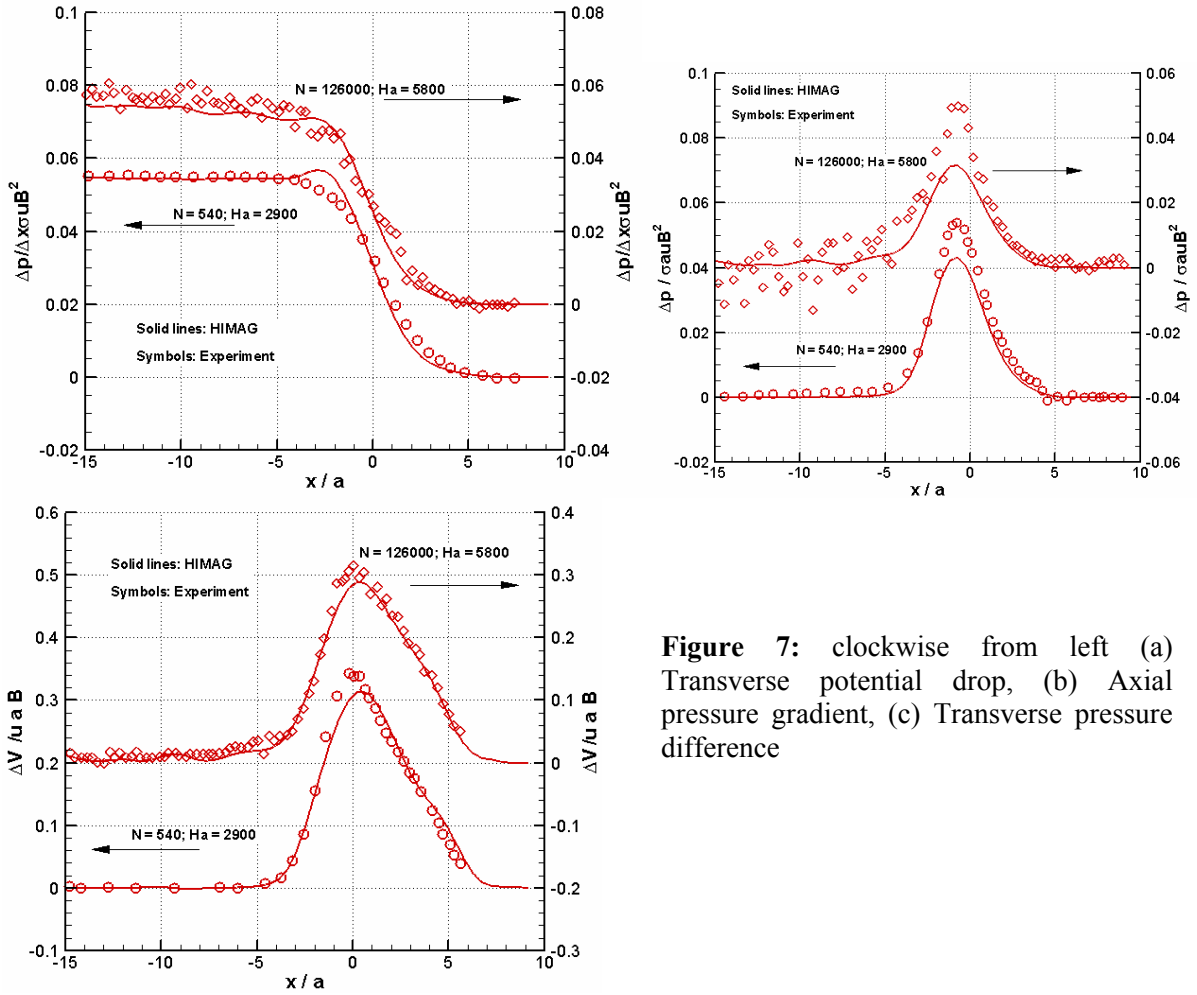


**Figure 7:** clockwise from left (a) Transverse potential drop, (b) Axial pressure gradient, (c) Transverse pressure difference

In figures [6e] and [7] we show results from HIMAG simulations matched against data from the experiments of Reed et al [43]. Considering the extreme values of Hartmann number (2900 and 5800) and the interaction parameter (540 and 126000) we feel that these results from full Navier Stokes modeling represent a unique landmark in MHD modeling, even for rectilinear geometries.

**Role of pressure taps**

Pressure taps were used to measure static pressure along the length of the channel in ref [43]. However, the presence of these taps itself induces a local flow and large local values of pressure gradient. These were accounted for in the data presented in ref [43]. We present here our computations of this effect, to obtain a feel for its magnitude. Fig [8] shows various views relevant to this effect, concluding in a pressure gradient diagram where we see about 80 – 90 % variation in pressure gradient near the pressure tap.

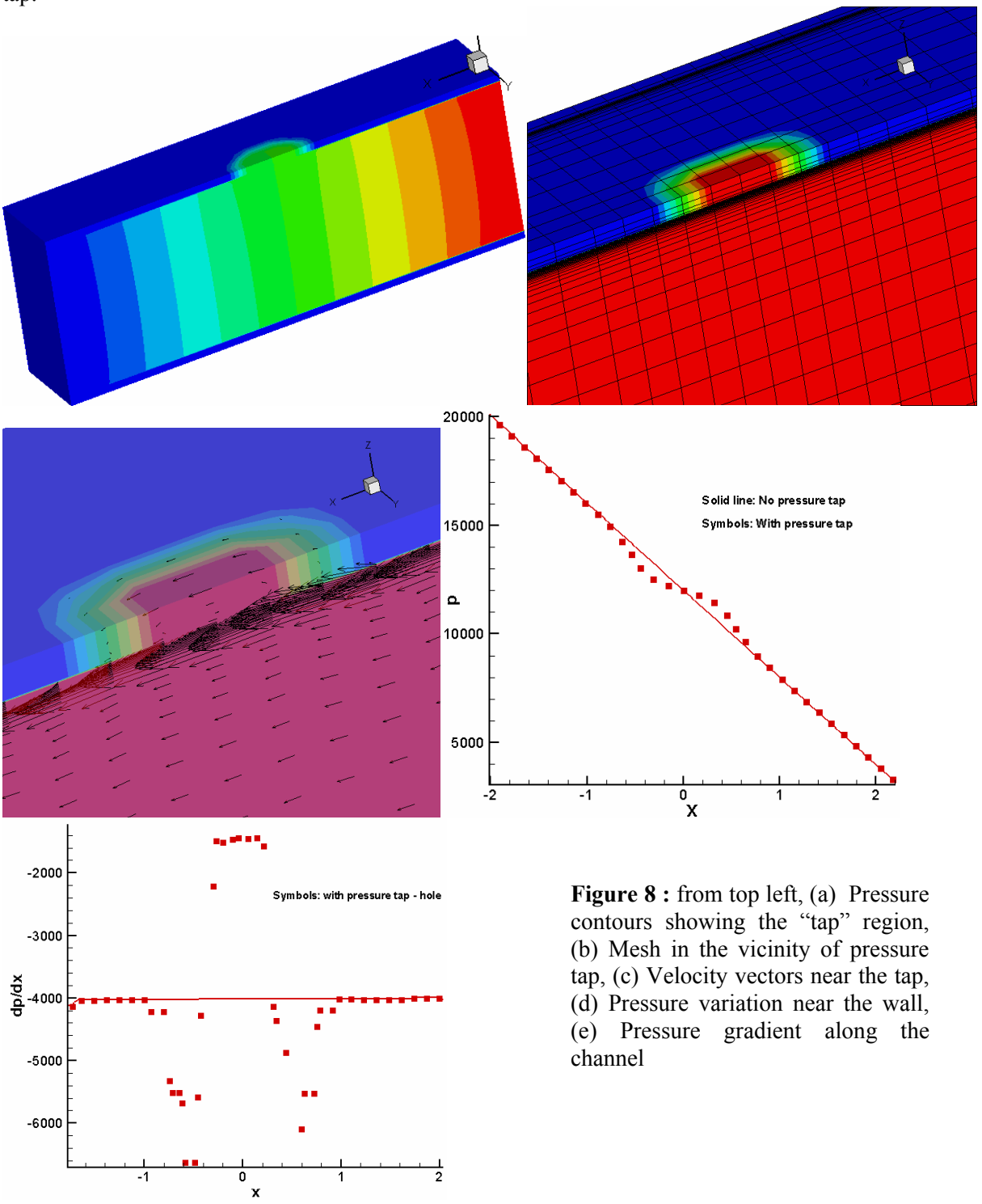


**Figure 8 :** from top left, (a) Pressure contours showing the "tap" region, (b) Mesh in the vicinity of pressure tap, (c) Velocity vectors near the tap, (d) Pressure variation near the wall, (e) Pressure gradient along the channel

## Circular Duct

We present here comparable results for the flow in a circular duct. It must be noted here that the geometry here, being somewhat simple, is numerically quite complex due to the need for a non-rectangular coordinate system. Due corrections were made for mesh-non-orthogonality, and as seen in the following figures, HIMAG has been spectacularly successful in modeling this flow at such a high Ha range.

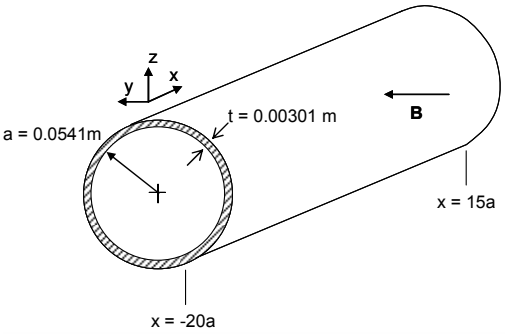


| Case-1 | Case-2 |
|---|---|
| $B_{max}$ = 2.08 T | $B_{max}$ = 1.103 T |
| Ha = 6640 | Ha = 3500 |
| N = 11061 | N = 770 |
| Re = 3986 | Re = 15909.1 |
| U = 0.07 m/s | U = 0.2794 m/s |

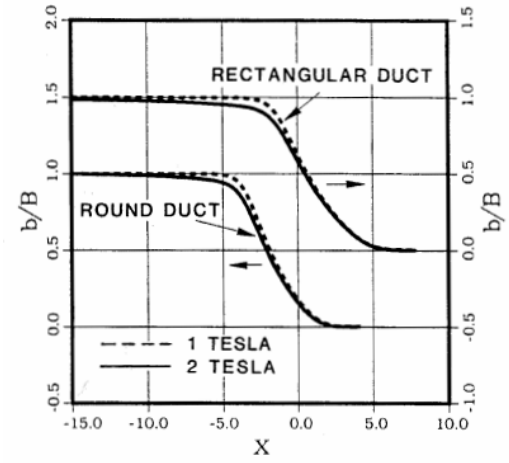


$$\rho = 865\,\mathrm{kg/m^3},$$
$$a = 0.0541 m,$$
$$\sigma = 2.86\times10^{6}\,/(\Omega m),$$
$$\mu = 8.2175\times10^{-4}\,\frac{kg}{m\cdot s},$$
$$c_w = 0.027,$$
$$t_w = 3.01\times10^{-3} m,$$
$$\sigma_w = 1.39\times10^{6}\,/(\Omega m)$$

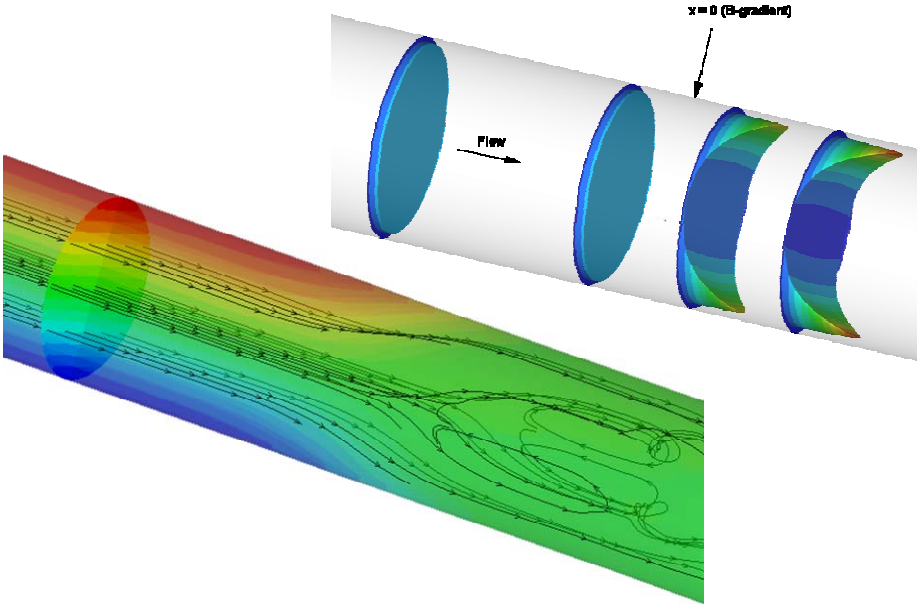


**Figure 9**: Circular duct experiment (a) Channel geometry, (b) Flow parameters and Applied magnetic field distribution, and (c) Streamlines, electric potential and velocity contours from HIMAG

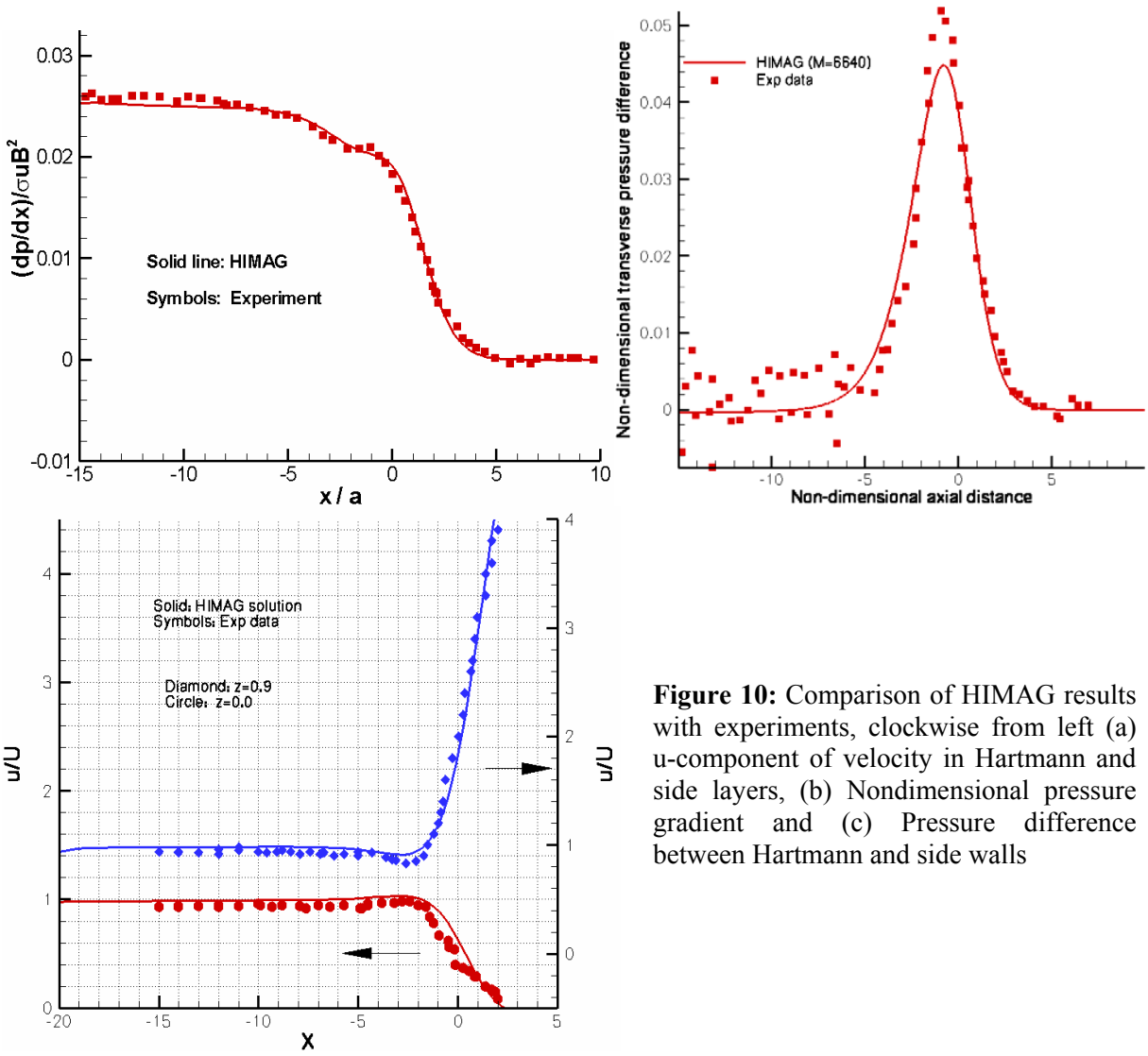


**Figure 10:** Comparison of HIMAG results with experiments, clockwise from left (a) u-component of velocity in Hartmann and side layers, (b) Nondimensional pressure gradient and (c) Pressure difference between Hartmann and side walls

### 4.3 Applications to the Dual Coolant Lead-Lithium (DCLL) blanket concept

We applied HIMAG to study the DCLL concept for a preliminary set of channel dimensions and flow conditions and summarize our results here. Figure [11a] shows a schematic of the detailed flow processes in the DCLL blanket, showing computed velocity profiles in the main flow ducts as well as in the inlet manifold as details. Figure [11b] shows a set of dimensions that were selected for this study.

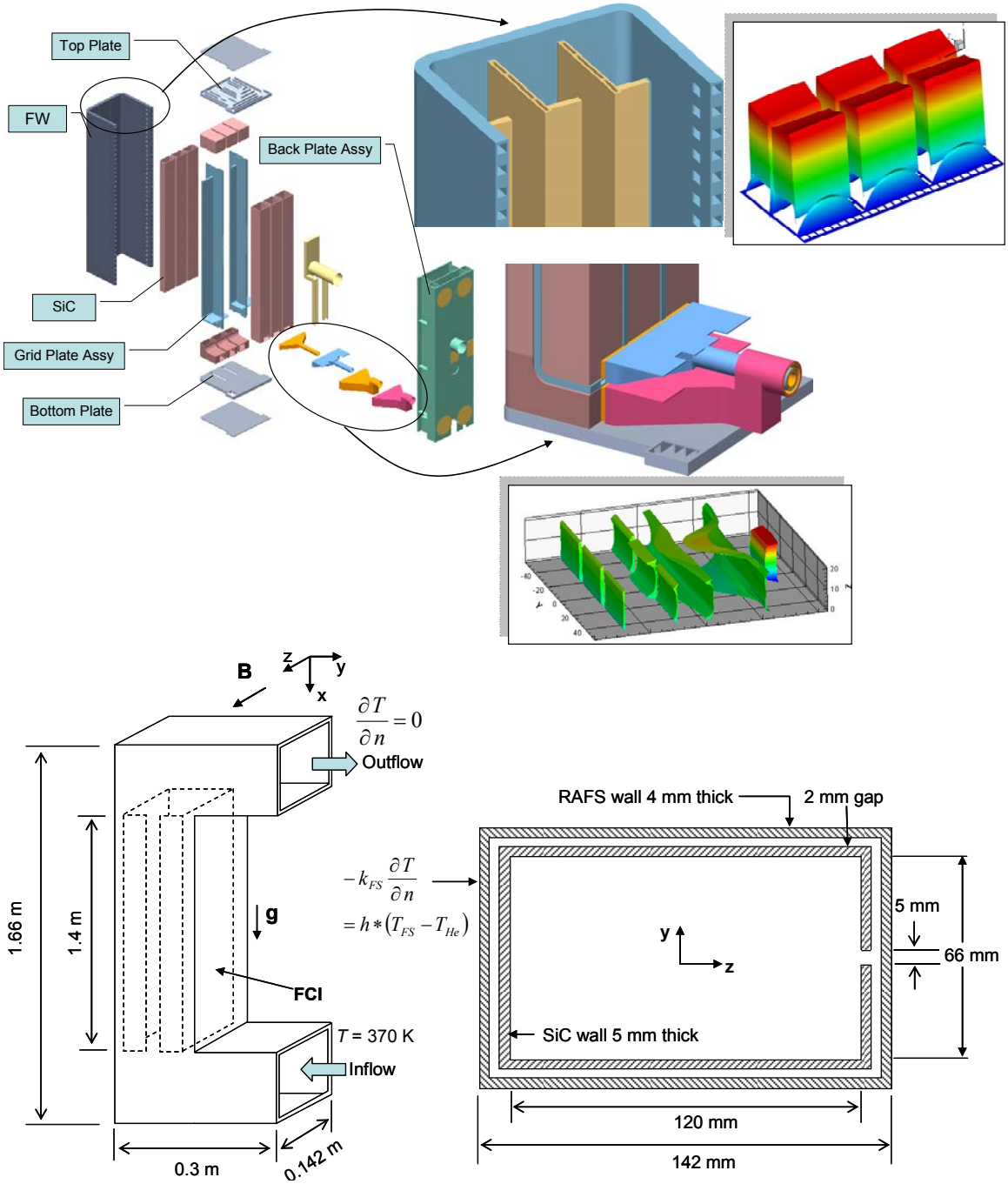


**Figure 11 :** (above) An exploded view of the DCLL parts, (below) Channel dimensions selected here showing the SiC flow channel insert (FCI) cross section

As seen here, a single DCLL-type duct with an enclosed flow channel insert made of low conductivity material is modeled. The case was studied at a Hartmann number of 500 and an interaction parameter of 1000. An interesting result from this study was that the pressure equalization slot in the FCI may not fully maintain a uniform pressure in the cross sectional region. As shown in the detailed views, the pressure is locally balanced near the slot, and there is a certain section of the duct where the net pressure inside and outside the SiC are matched. However, there seems to be a three dimensional variation, which depends strongly on flow conditions. The magnitude of this pressure difference may be acceptable for higher Hartmann number conditions, and this is being presently investigated. We also see the strong recirculation currents caused by natural convection in fig [16], and the nature of flow branching when the flow approaches the FCI from an initial development region where there is no FCI.

In an attempt to understand the physics of flow entering the FCI and three dimensional effects associated therewith, we divided the DCLL flow into three regions as shown in figure [12]. Region-1 has flow entering a steel pipe and approaching a right angled bend, while region-2 contains entry effects where the FCI begins. Region-3 is an almost uniform region of the DCLL where FCI physics will dominate. Figures [13 – 15] present results from this study, showing details of velocity and pressure distributions in each of these regions. It must be noted that these figures show results neglecting heat transfer and natural convection, while figure [16] shows streamlines and temperature contours for a "full" case in which all of these effects are included. Needless to say, such data is extremely invaluable in designing liquid breeder blankets both for domestic programs in fusion as well as international efforts.

RAFS:
Thickness = 4 mm
ρ = 7800 kg/m$^3$
σ = 1.4E6 S/m
$K$ = 33 W/(m k)
$C_p$ = 750 J/(kg K)

FCI (SiC)
Thickness = 5mm
ρ = 2500 kg/m$^3$
σ = 5 S/m
$K$ = 5 W/(m k)
$C_p$ = 800 J/(kg K)

Pb-Li
ρ = 9300 Kg/m$^3$
σ = 7.0e5 S/m
μ = 1.0e-3 kg/(m s)
K = 20.0 W/(m K)
$C_p$ = 190.0 J/(kg K)

Operating conditions:

Inlet Velocity = 0.07 m/s
B = 4T

Re = 9300*0.07*60e-3/1.0e-3
= 39,060

Ha = 4*60e-3*sqrt(7.0e5/1.0e-3)
= 6,349.8

Interaction parameter Ha$^2$/Re = 1032.25

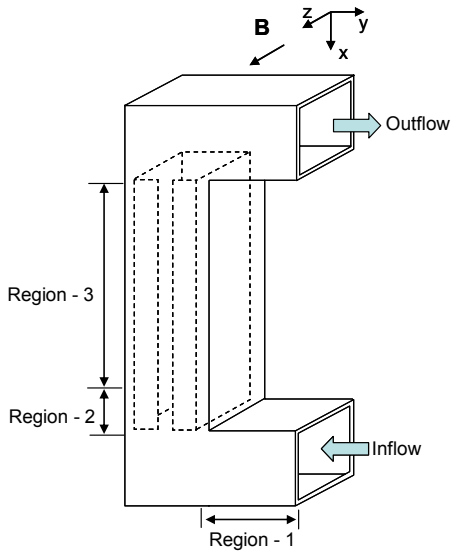


**Figure 12:** Physical properties and flow conditions for the DCLL simulations and region-breakup

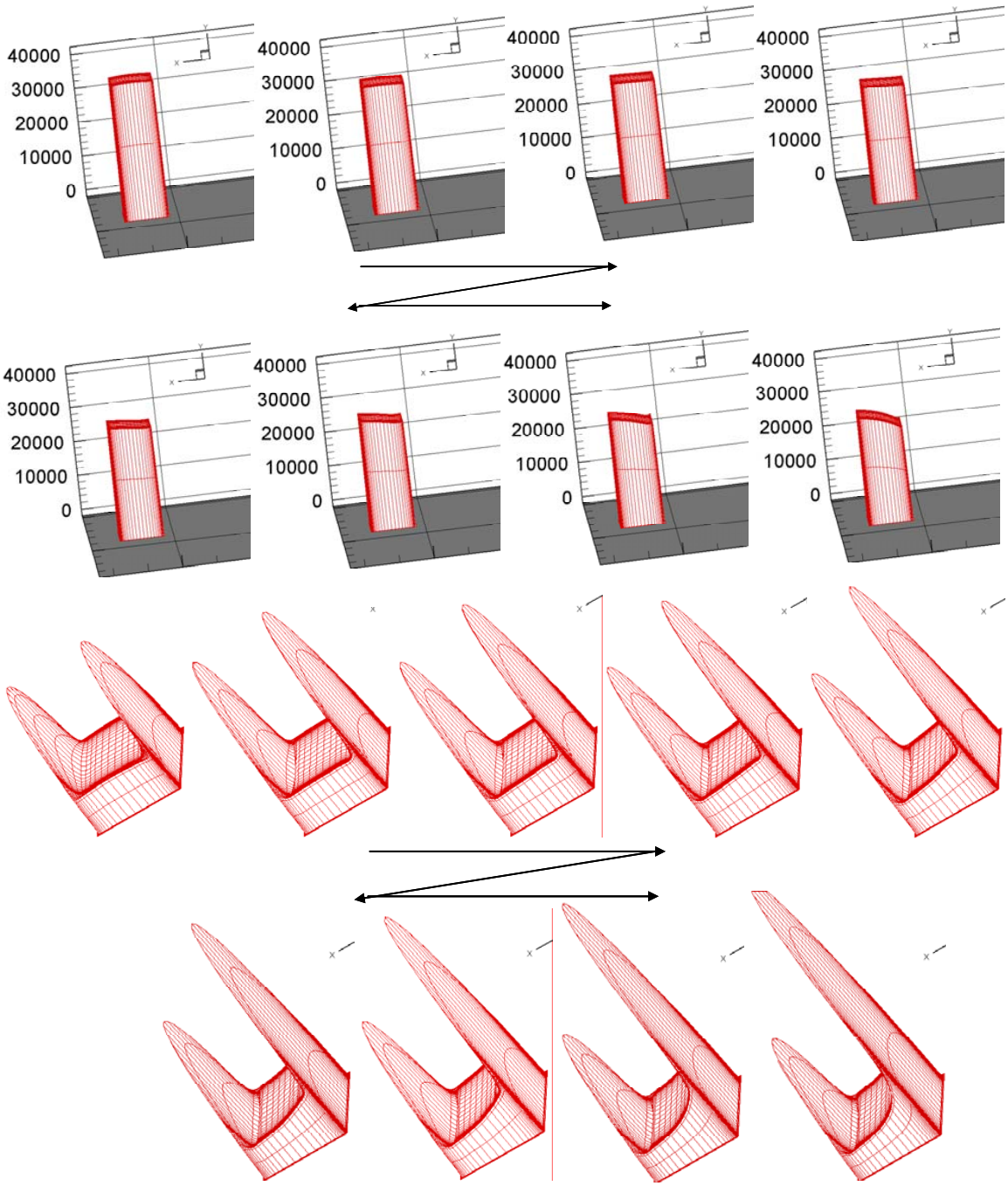


**Figure 13**: Region-1 pressure (above) and velocity (below) distributions

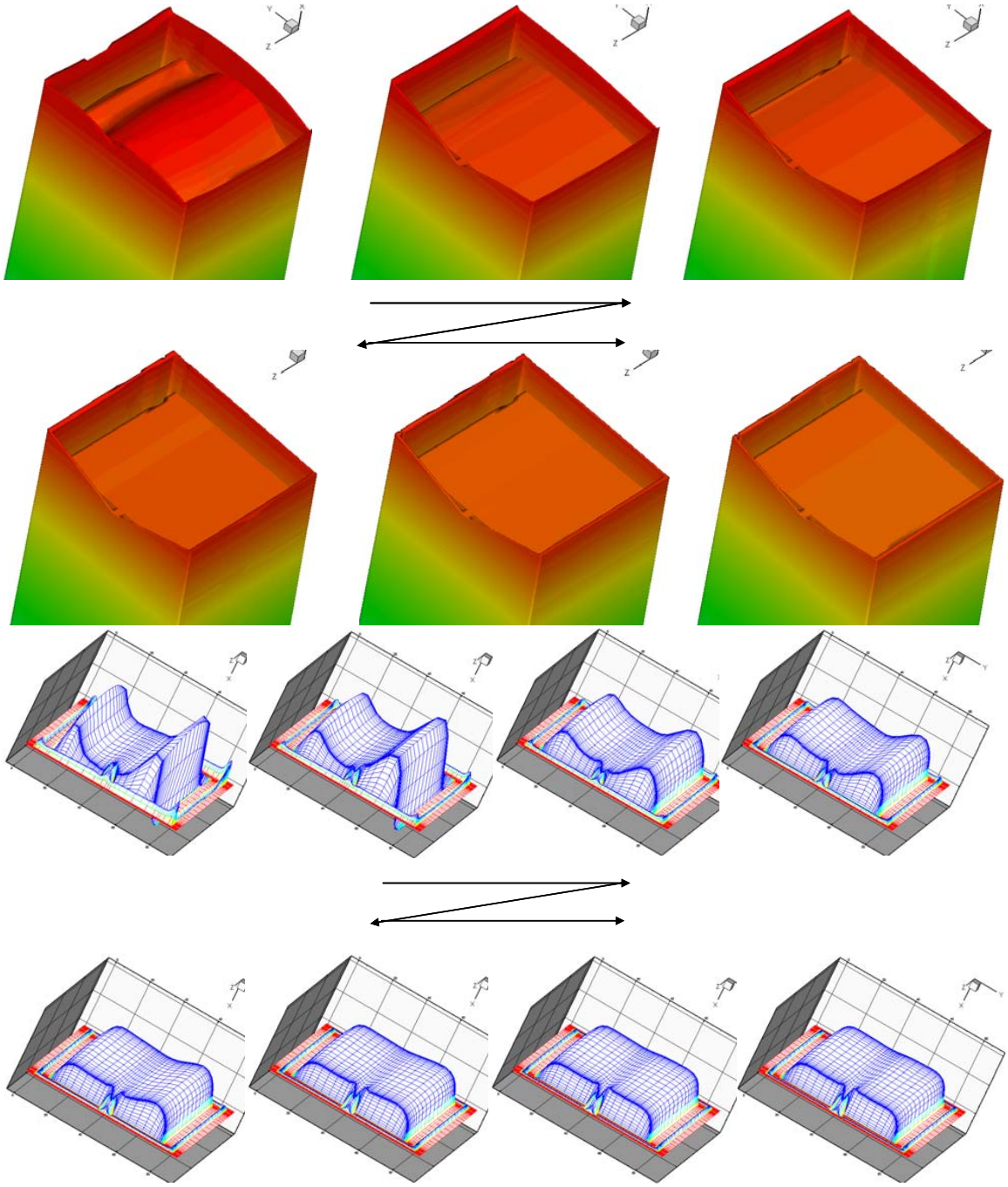

**Figure 14:** Region-2 pressure (above) and velocity (below) distributions

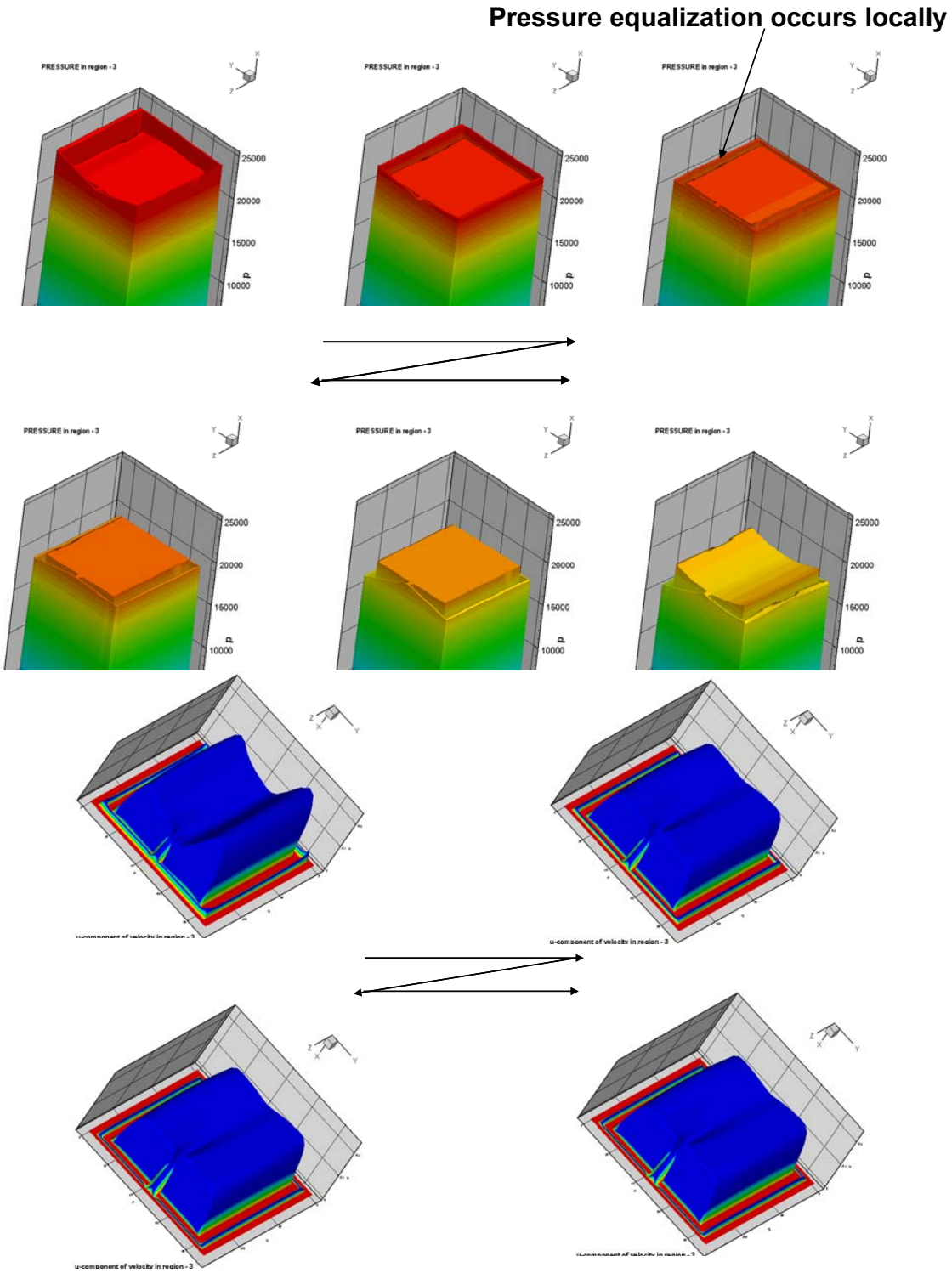


**Figure 15:** Region-3 Pressure (above) and velocity (below) distributions

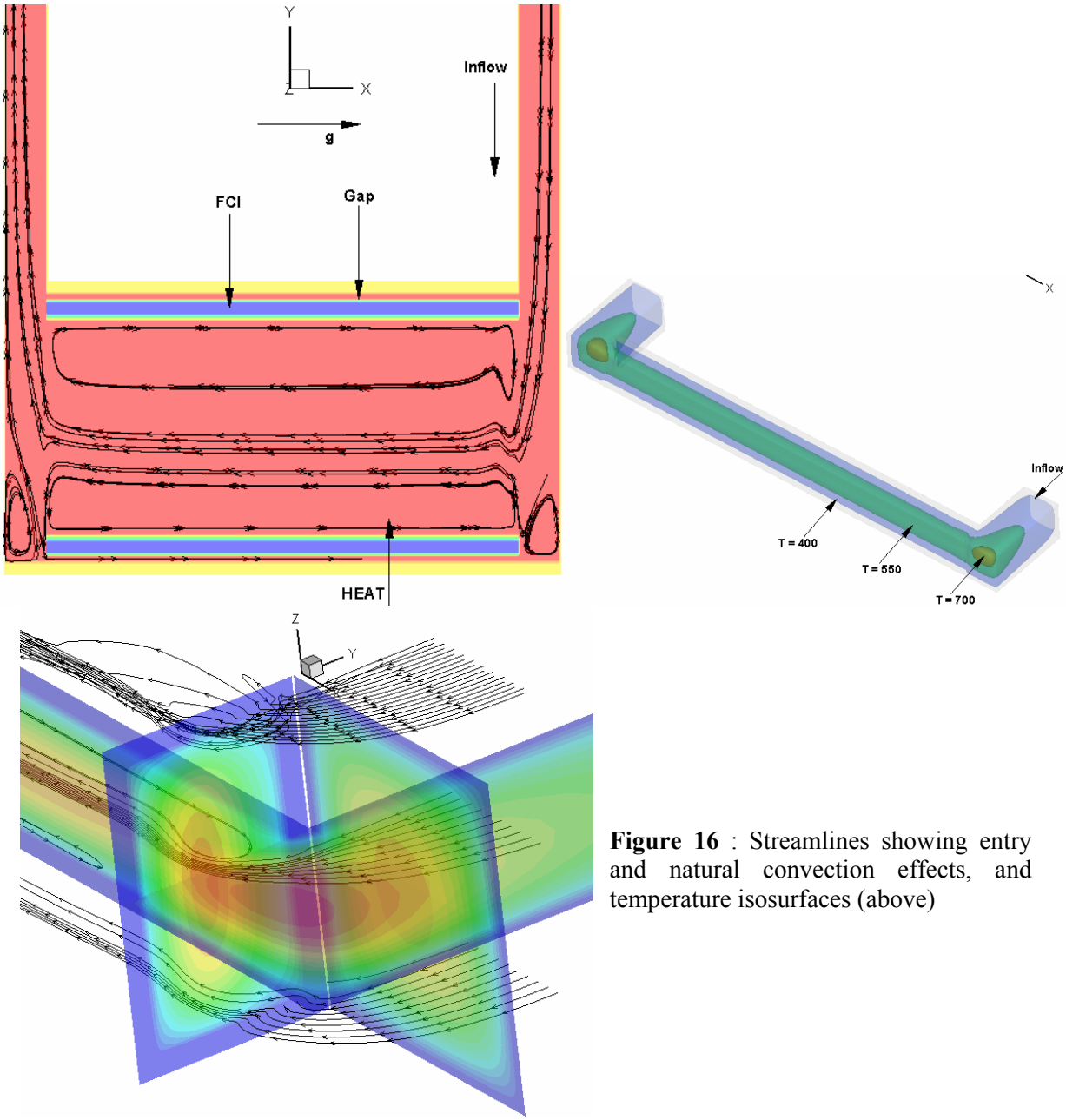


**Figure 16** : Streamlines showing entry and natural convection effects, and temperature isosurfaces (above)

### 4.4 Study of Flow Channel Inserts

In this and the following sections [4.4] to [4.8] we present various aspects of the DCLL flow which are critical to understanding the physics involved. In the course of Phase-II investigations, we enabled HIMAG to be able to model these situations, developed pre- and post-processing capabilities that will enable problem setup as well as data reduction intuitive, easy and accurate. The success of our efforts is seen in the level of detail and intuitive insight provided by these simulations. We begin with emulating the effect of FCI by internal body forces, to understand the tendency of internal body forces to destabilize pressure equalization across the FCI. Figure [17] shows the geometry and problem setup, while figures [18] and [19] show the effect on pressure and velocity fields as the body force is increased. A strongly three-dimensional flow is observed, which deviates from pressure equalization almost monotonically, as the internal body force is increased. The internal body force can be considered to represent inertial effects caused by three-dimensional flow features: entry, fringing fields, natural convection and so forth.

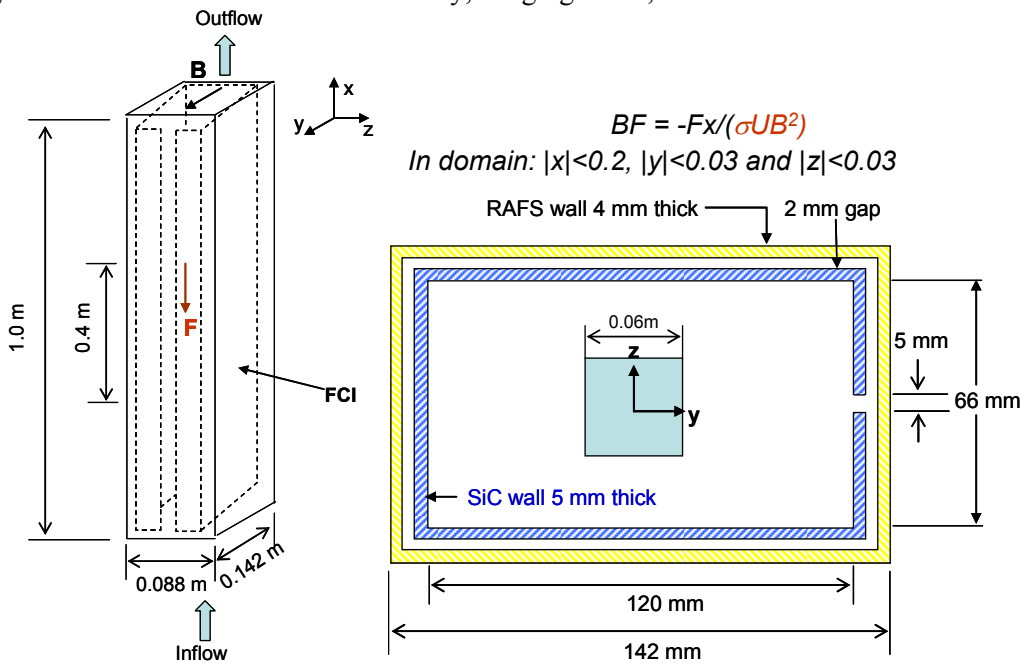


RAFS:
Thickness = 4 mm
ρ = 7,800 kg/m³
σ = 1.4E6 S/m

FCI (SiC)
Thickness = 5mm
ρ = 2,500 kg/m³
σ = 5 S/m

Pb-Li
ρ = 9,300 Kg/m³
σ = 7.0e5 S/m
μ = 1.0e-3 kg/(m s)

Operating conditions:

Inlet Velocity = 0.0017921 m/s
B = 0.62994T

Re = 9300* 0.0017921 *60e-3/1.0e-3
= 1,000

Ha = 0.62994*60e-3*sqrt(7.0e5/1.0e-3)
= 1,000

Interaction parameter $Ha^2/Re$ = 1,000

$c_w$ = 0.133

**Figure 17:** Geometry and flow conditions for the study on flow channel inserts

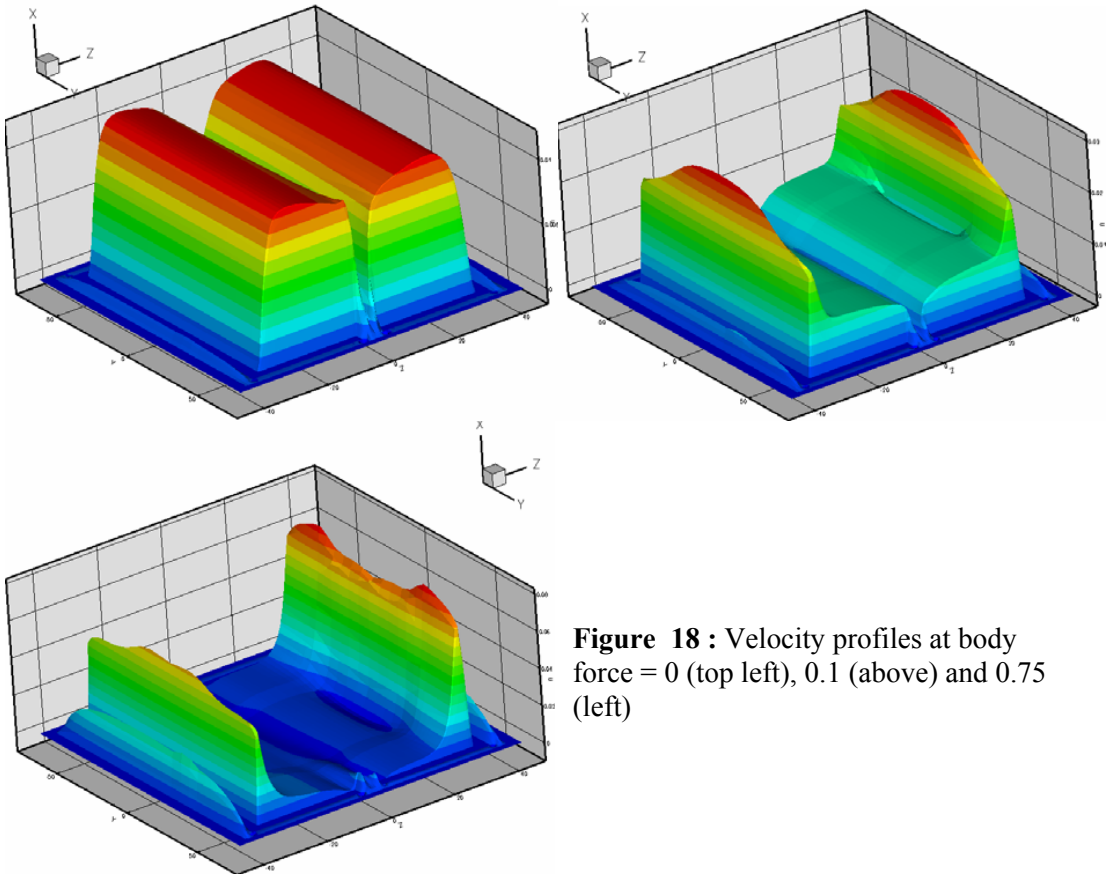

**Figure 18 :** Velocity profiles at body force = 0 (top left), 0.1 (above) and 0.75 (left)

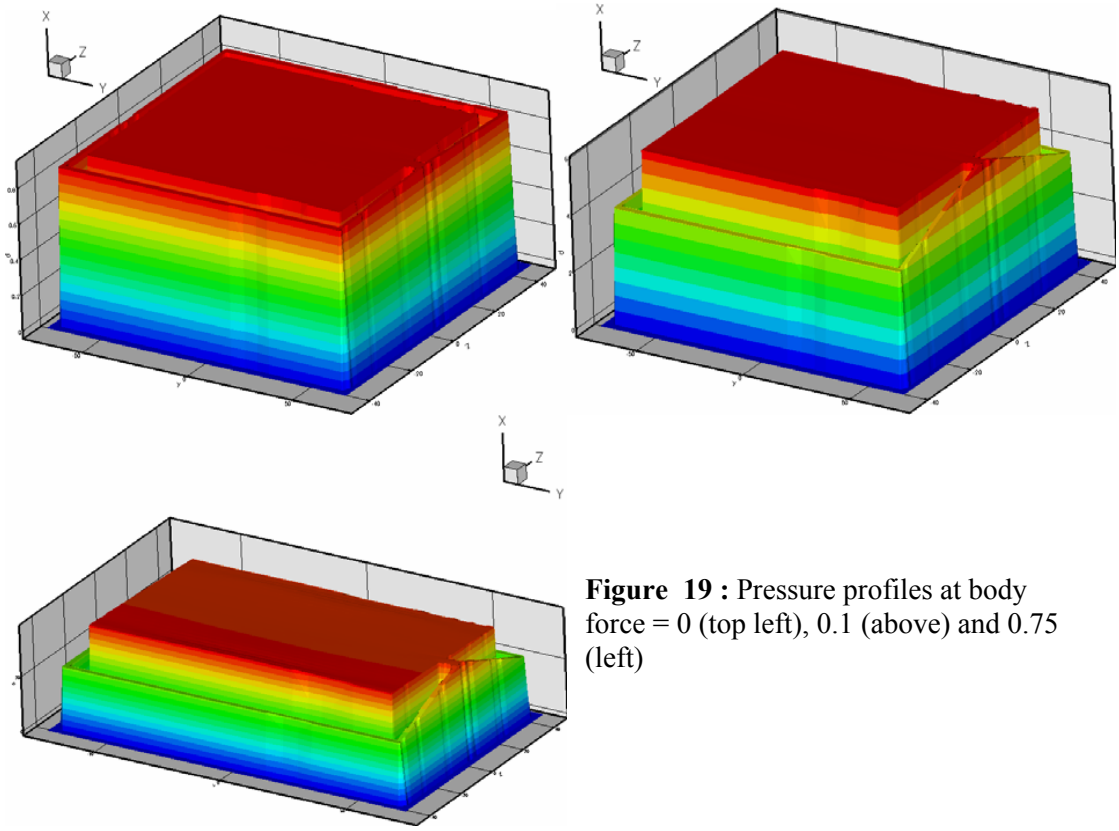

**Figure 19 :** Pressure profiles at body force = 0 (top left), 0.1 (above) and 0.75 (left)

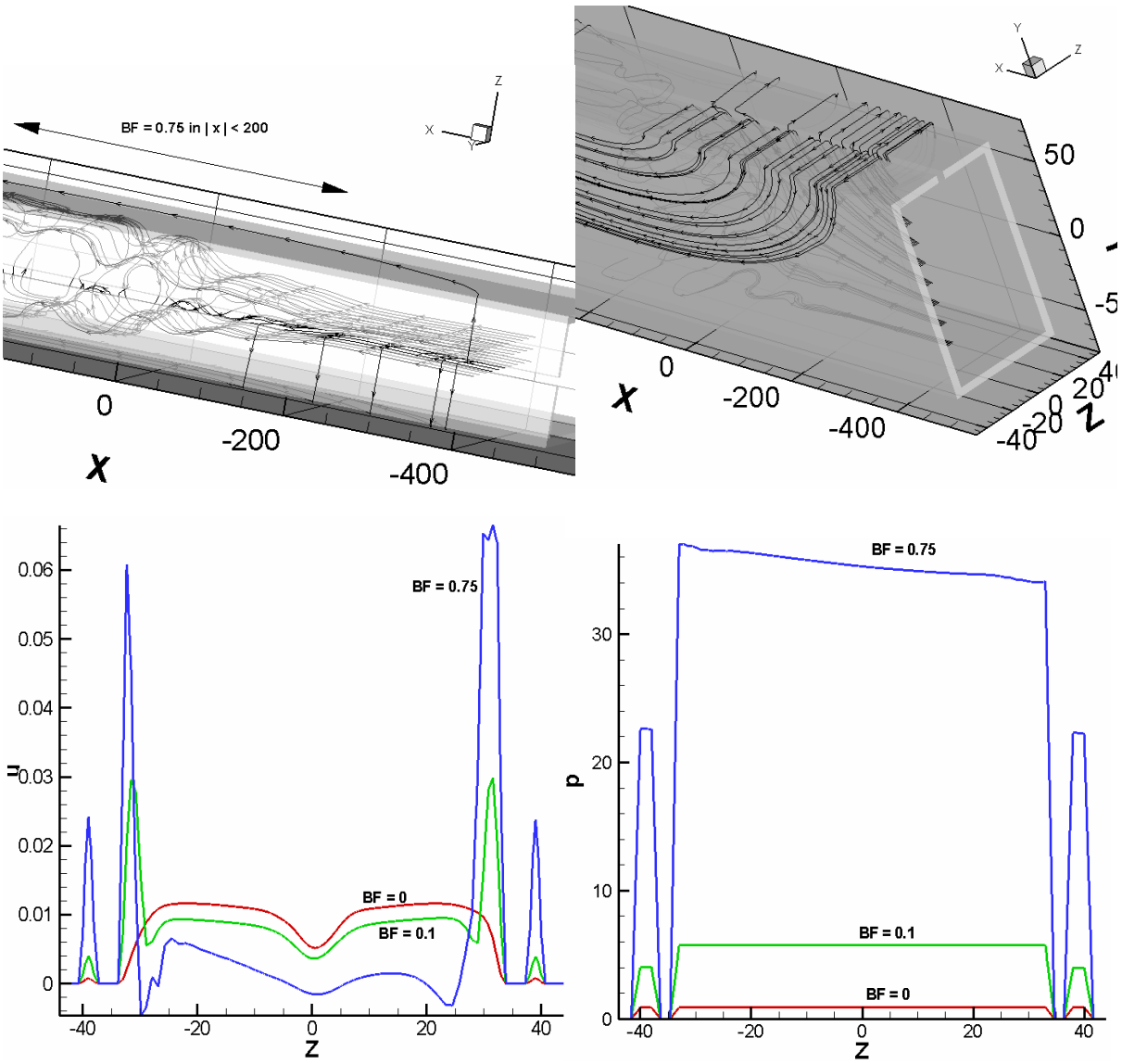


**Figure 20:** Streamlines, velocity and pressure profiles for various values of the flow obstruction parameter

### 4.5 Entry Effects

In this portion of the work we studied the nature of flow development at the entrance to a flow channel insert. The following figures show the problem geometry, pressure contours and streamlines. The Hartmann number was 6350 and Reynolds number was 39,060. We see a significant entry effect and three dimensionality in the flow in the entire channel when the channel length was selected to be equal to the side-dimension of the duct. We see the current lines closing outside of the flow channel insert, and not within the channel itself, thus resulting in greatly reduced pressure gradients within the channel.

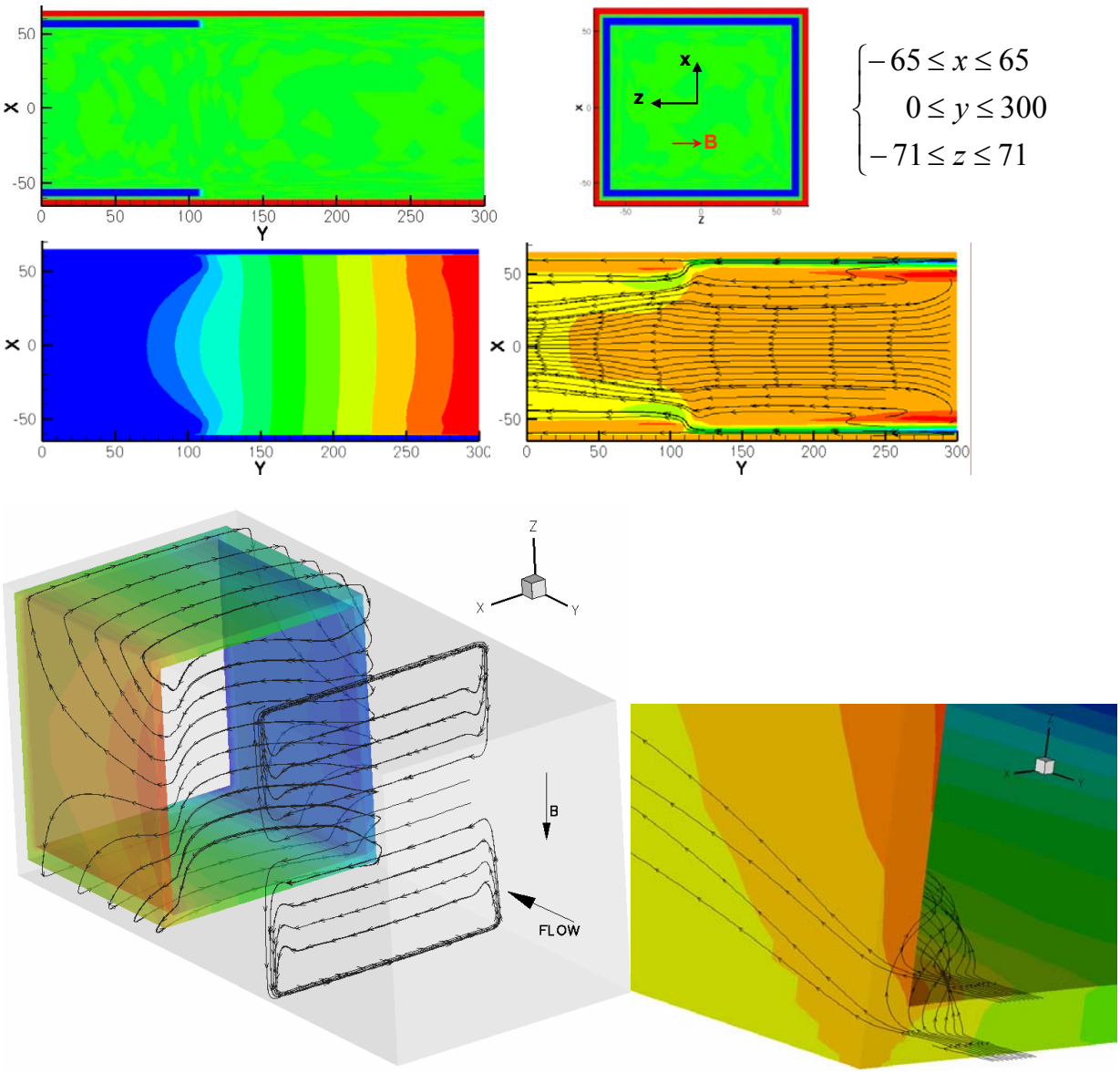


**Figure 21:** Streamlines and current lines at the beginning of a flow channel insert

### 4.6 Increase in flow development length

Here we present the length of channels needed for fully developed flow to occur. The post processing abilities developed here enable the user to visually observe the depth to which electric current lines bend in the flow, causing three-dimensionality, which is felt by the velocity and pressure distributions.

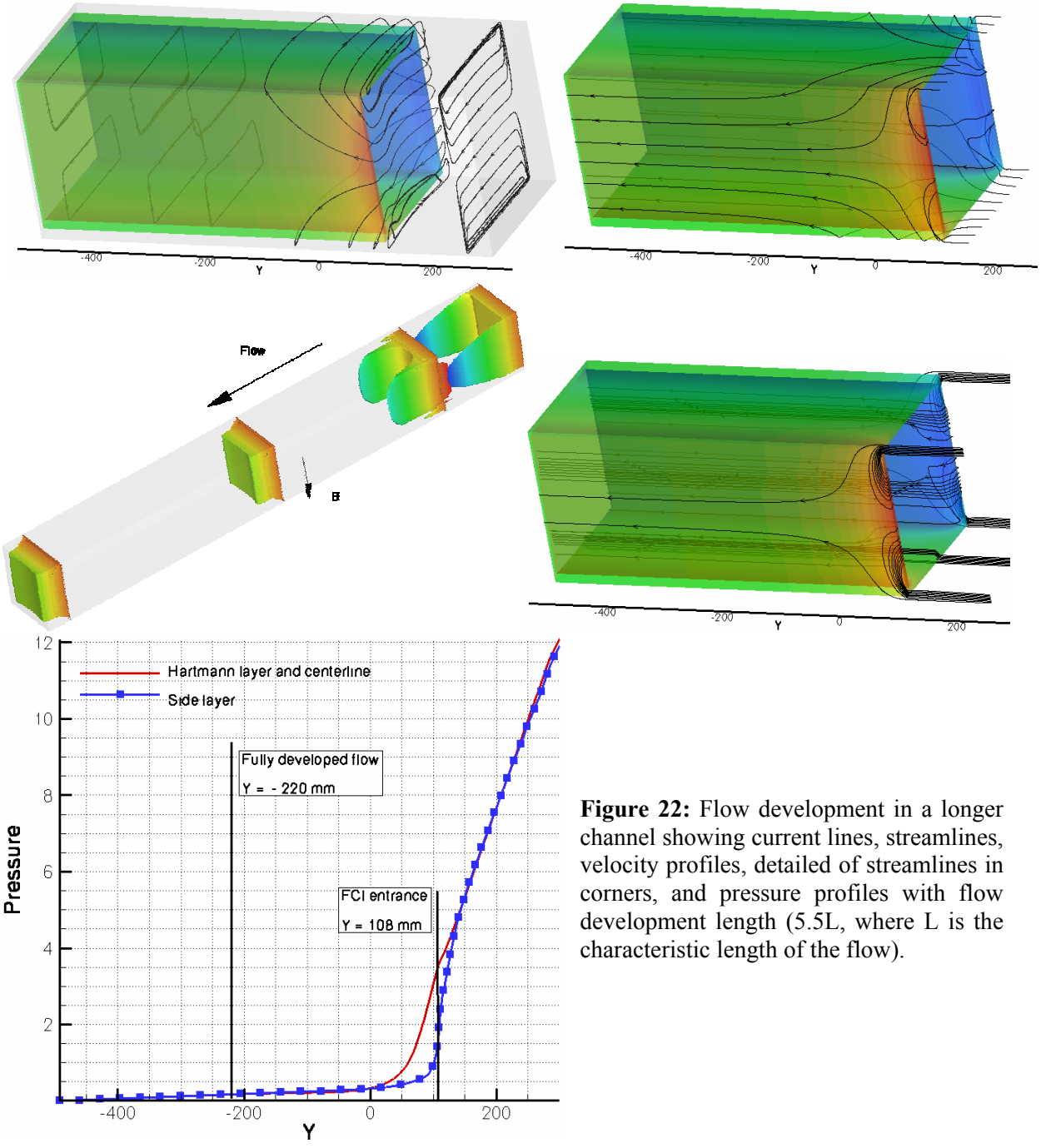


**Figure 22:** Flow development in a longer channel showing current lines, streamlines, velocity profiles, detailed of streamlines in corners, and pressure profiles with flow development length (5.5L, where L is the characteristic length of the flow).

### 4.7 Divided Flow Channel Insert

The results of the above exercise were re-evaluated in a channel with a split flow channel insert with the following results. Three dimensionality and mass flow leakage occurs at the split region.

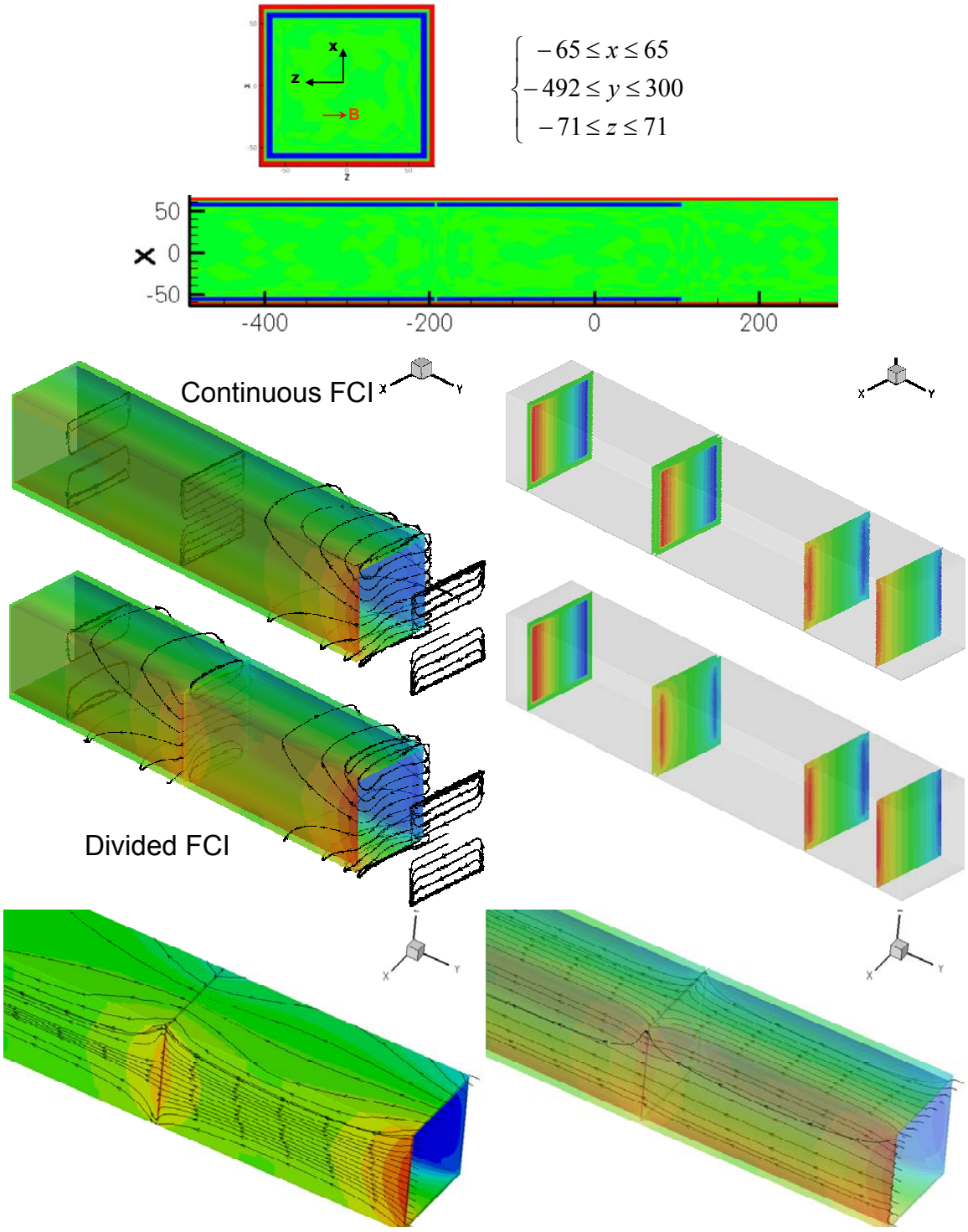


**Figure 23:** Geometry current lines, potential contours and streamlines for flow with a divided FCI

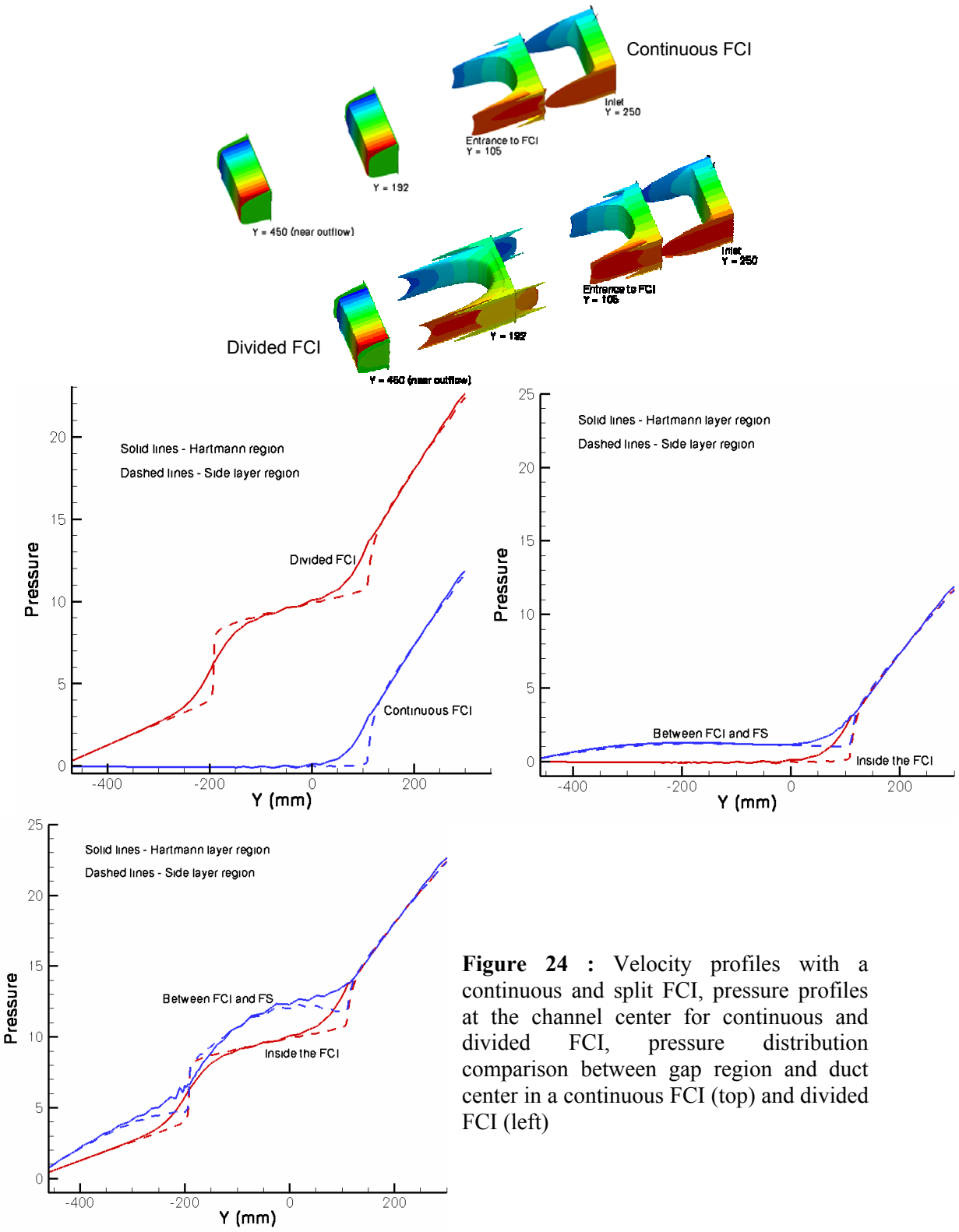


**Figure 24 :** Velocity profiles with a continuous and split FCI, pressure profiles at the channel center for continuous and divided FCI, pressure distribution comparison between gap region and duct center in a continuous FCI (top) and divided FCI (left)

### 4.8 Inlet Manifold

A sample inlet manifold geometry being investigated for ITER-TBM is shown in figure [25]. A single rectangular inlet channel undergoes an abrupt 4x expansion, and then subdivides into 3 parallel channels. The y=0 plane is taken as a symmetry plane, and so only half of the geometry as shown in Fig. 2. is meshed. As a rough approximation of flow with insulating flow channel inserts, the analyses utilize electrically insulated walls. A mass flow rate is prescribed at the inlet, and pressures and normal current density at the outlets of the 3 parallel channels are set to 0. As described in Ref. [30], this outlet condition is considered as imposing a kind of symmetry, where the 3 channels continue and then enter another manifold where they are consolidated into a return channel – with the same pressure drop behavior as the inlet manifold. Such an assumption appears to be justified when considering a simple expansion / contraction pair according to the high Ha and N linear theory as discussed in Ref. [30]. Figure [26] shows problem geometry and figure [27] shows velocity distributions at various cross sectional planes in the inlet manifold. Ref [30] contains a more detailed description of this problem and further simulations made using HIMAG to understand the flows in inlet manifolds with MHD.

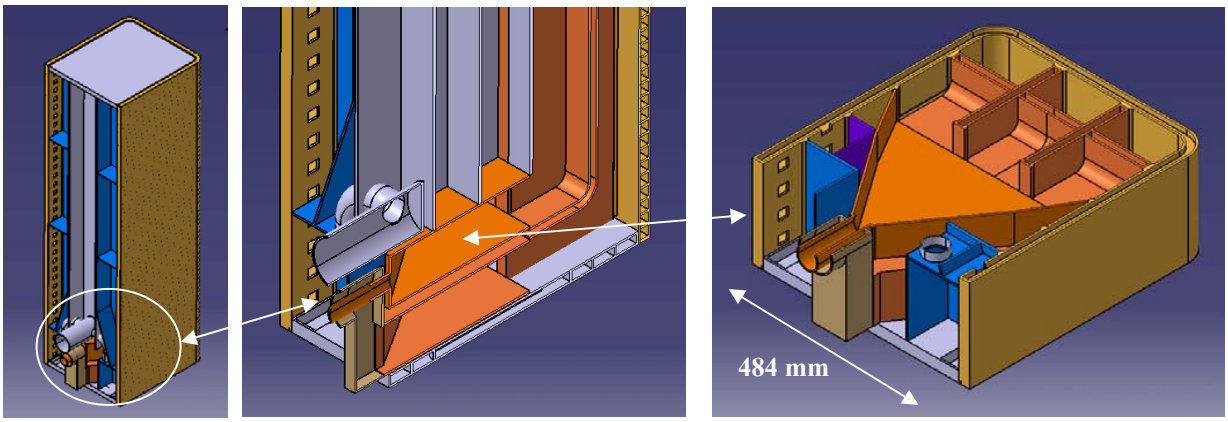


**Figure 25**: Views of US DCLL Test blanket module showing different view of manifold region

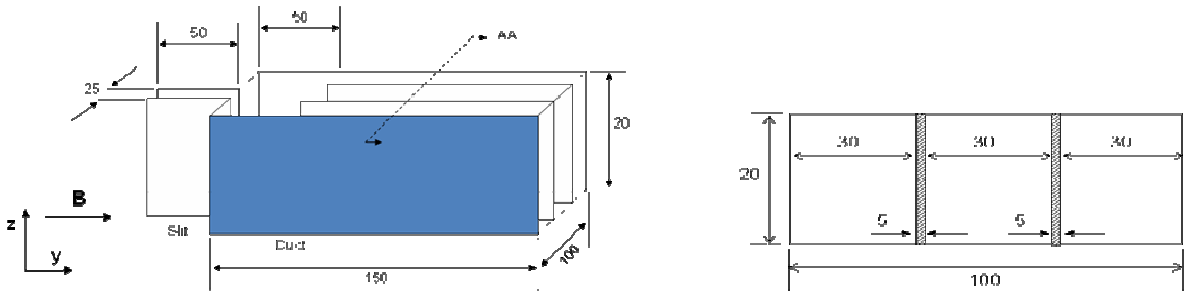


**Figure 26:** Geometric model of idealized DCLL manifold used in 3D simulations (dimensions in mm)

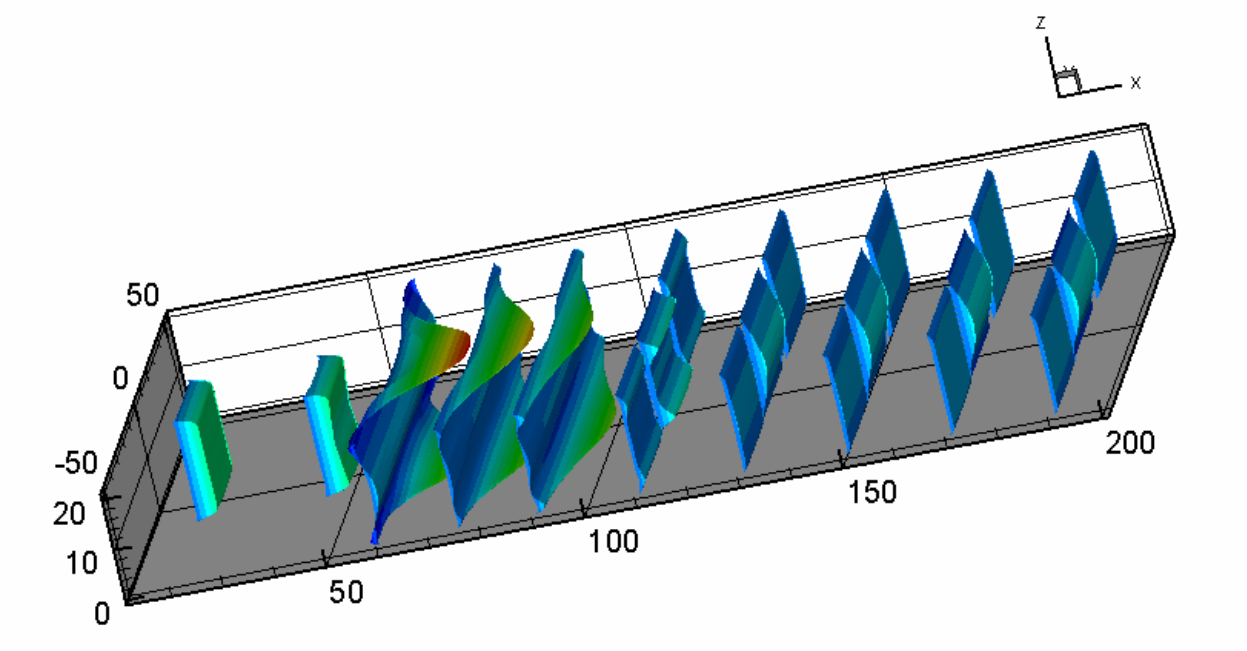


**Figure 27:** Axial velocity profiles at various axial locations for (dimensions in mm, velocity in m/s)

### 4.9 Tritium permeation and transport

During the course of the Phase-II project we added a model within HIMAG for the permeation and transport of Tritium. We present here the summary of the mathematical formulation, numerical technique and a sample result from this study.

**Equations:**

$$\frac{\partial C_s}{\partial t} + \nabla \cdot (C_s \mathbf{u}) = \nabla \cdot \left( D \nabla C_s + C_s \frac{Q}{\kappa T^2} \nabla T \right)$$

$$D_1 \frac{\partial C_s}{\partial n}\Big|_L = D_2 \frac{\partial C_s}{\partial n}\Big|_R$$

$$\frac{k_1}{C_L} = \frac{k_2}{C_R}$$

on material interface

Linearized in time, and used Crank-Nicholson implicit procedure:

$$\frac{\Omega}{\Delta t}\left(C_{ic}^{\,n+1} - C_{ic}^{\,n}\right)\frac{\partial}{\partial t} + \sum_{faces}\left(C_s \mathbf{u}\right)_f^{\,n+1} \cdot \Delta s = \sum_{faces}\left(D \nabla C_s\right)_f^{\,n+1} \cdot \Delta s + \sum_{faces}\left(\frac{Q}{\kappa T^2}\nabla T\right)_f^{\,n+1} \cdot \Delta s$$

Where:

- $$\left(D \nabla C_s\right)_f^{\,n+1} \cdot \Delta s = D_f \frac{\partial C_s^{\,n+1}}{\partial n}\Big|_f \Delta s = D_f \left( \frac{C_{inb}^{\,n+1} - C_{ic}^{\,n+1}}{d} + S_3 \right) \Delta s$$

  Here $S_3$ is an extra term from non-orthogonal correction, and can be omitted.

- $$\left(C_s \mathbf{u}\right)_f^{\,n+1} \cdot \Delta s = \frac{1}{4}\left(C_f^{\,n+1} + C_f^{\,n+1}\right)\left(\mathbf{u}^{n+1} + \mathbf{u}^{n}\right)_f \cdot \Delta s = \frac{1}{2}\left(C_f^{\,n+1} + C_f^{\,n+1}\right)\overline{U} \cdot \Delta s$$

  and $$\overline{U} = \frac{1}{2}\left(U^{n+1} + U^{n+1}\right)$$

- $$\left(\frac{Q}{\kappa T^2}\nabla T\right)_f^{\,n+1} \cdot \Delta s = \left(\frac{Q}{\kappa}\right)_f \left(\frac{1}{T^{n+1}}\right)^2 \left(\frac{\partial T}{\partial n}\right)_f^{\,n+1} C_f^{\,n+1} \Delta s = \beta_0 C_f^{\,n+1} \Delta s$$

The general contribution of all terms will be written as

$$\left(\frac{\Omega}{\Delta t} + \alpha_{ic}\right) C_{ic}^{\,n+1} = \frac{\Omega}{\Delta t} C_{ic}^{\,n} + \alpha_d$$

**For internal faces without material interface:**

There is the same material on both sides. The following conditions applied:

$$\frac{1}{D_f}=\frac{f}{D_l}+\frac{f_1}{D_r} \qquad \text{and} \qquad C_f = fC_{ic}+f_1C_{iinb}$$

$$D_l = D_{ic} \qquad \text{and} \qquad D_r = D_{inb}$$

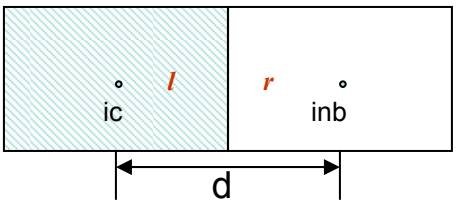


The contribution of all terms for internal faces is

$$\begin{cases} \alpha_{ic} = \sum_{faces}\left[\frac{\overline{U}}{2}\Delta sf+\frac{D_f}{d}\Delta s-\beta_0\Delta sf\right] \\ \alpha_d = \sum_{faces}\left[-\frac{\overline{U}}{2}\Delta s\left(f_1C_{inb}{}^{n+1}+fC_{ic}{}^{n}+f_1C_{inb}{}^{n}\right)+\frac{D_f}{d}\Delta sC_{inb}{}^{n+1}+\beta_0\Delta sf_1C_{inb}{}^{n+1}\right] \end{cases}$$

**For internal faces with fluid on left side and solid on right side:**

The right cell ***inb*** is solid and the following conditions applied:

$$D_f = D_l$$

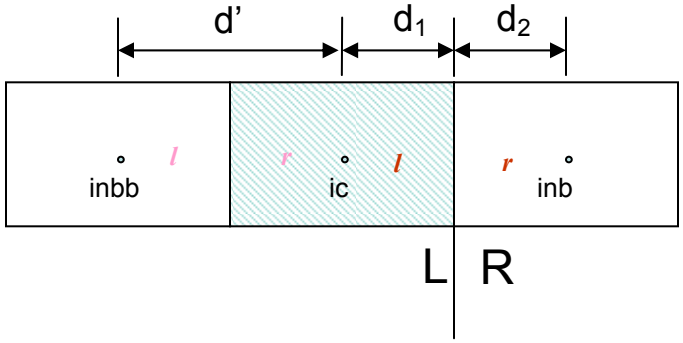


$$\frac{\partial C_s{}^{n+1}}{\partial n}\Big|_l = \frac{C_{ic}{}^{n+1}-C_{inbb}{}^{n+1}}{d'}=\alpha$$

$$\frac{\partial C_s{}^{n+1}}{\partial n}\Big|_L = \frac{C_L{}^{n+1}-C_{ic}{}^{n+1}}{d_1}=\frac{\partial C_s{}^{n+1}}{\partial n}\Big|_l=\alpha$$

$$\frac{\partial C_s{}^{n+1}}{\partial n}\Big|_R = \frac{C_R{}^{n+1}-C_{inb}{}^{n+1}}{d_2}=-\frac{D_1}{D_2}\alpha$$

And the material interface conditions become:

$$\begin{cases} C_R{}^{n+1} = C_{inb}{}^{n+1}-d_2\frac{D_1}{D_2}\alpha \\ C_L{}^{n+1} = \frac{k_1}{k_2}\left(C_{inb}{}^{n+1}-d_2\frac{D_1}{D_2}\alpha\right) \end{cases}$$

The contribution of all terms for internal faces is

$$\begin{cases} \alpha_{ic} = \sum_{faces}\left[-\frac{\overline{U}}{2}\Delta s\frac{k_1}{k_2}\frac{d_2}{d'}\frac{D_1}{D_2}+\frac{D_f}{d_1}\Delta s\left(1+\frac{k_1}{k_2}\frac{d_2}{d'}\frac{D_1}{D_2}\right)+\beta_0\Delta s\frac{k_1}{k_2}\frac{d_2}{d'}\frac{D_1}{D_2}\right] \\ \alpha_d = \sum_{faces}\left\{\begin{array}{l}\frac{\overline{U}}{2}\Delta s\frac{k_1}{k_2}\left[\frac{d_2}{d'}\frac{D_1}{D_2}C_{ic}{}^{n}-\left(C_{inb}{}^{n+1}+C_{inb}{}^{n}\right)-\frac{d_2}{d'}\frac{D_1}{D_2}\left(C_{inbb}{}^{n+1}+C_{inbb}{}^{n}\right)\right]+ \\ \frac{D_f}{d_1}\Delta s\frac{k_1}{k_2}\left[C_{inb}{}^{n+1}+\frac{d_2}{d'}\frac{D_1}{D_2}C_{inbb}{}^{n+1}\right]+\beta_0\Delta s\frac{k_1}{k_2}\left[C_{inb}{}^{n+1}+\frac{d_2}{d'}\frac{D_1}{D_2}C_{inbb}{}^{n+1}\right]\end{array}\right\} \end{cases}$$

**For internal faces with solid on left side and fluid on right side:**

The right cell ***ic*** is solid and the following conditions applied:

$$D_f = D_r$$

$$\frac{\partial C_s^{\,n+1}}{\partial n}\Big|_L = \frac{C_{inb}^{\,n+1} - C_{inbb}^{\,n+1}}{d'} = \alpha$$

$$\frac{\partial C_s^{\,n+1}}{\partial n}\Big|_R = \frac{C_R^{\,n+1} - C_{ic}^{\,n+1}}{d_1} = -\frac{D_1}{D_2}\alpha$$

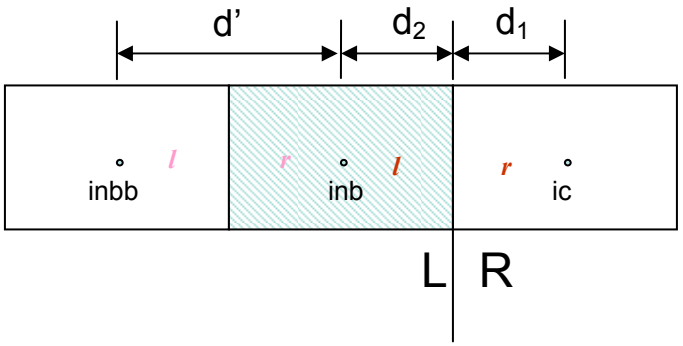


And the material interface conditions become:

$$C_R^{\,n+1} = C_{ic}^{\,n+1} - d_1 \frac{D_1}{D_2}\alpha$$

The contribution of all terms for internal faces is

$$\begin{cases} \alpha_{ic} = \sum_{faces}\left[\dfrac{\overline{U}}{2}\Delta s - \beta_0 \Delta s\right] \\ \alpha_d = \sum_{faces}\left\{\begin{array}{l} \dfrac{\overline{U}}{2}\Delta s\left[\dfrac{d_1}{d'}\dfrac{D_1}{D_2}\left(C_{inb}^{\,n+1} - C_{inbb}^{\,n+1} + C_{inb}^{\,n} - C_{inbb}^{\,n}\right) - C_{ic}^{\,n}\right] - \\ \dfrac{D_f}{d_1}\Delta s \dfrac{d_1}{d'}\dfrac{D_1}{D_2}\left[C_{inb}^{\,n+1} - C_{inbb}^{\,n+1}\right] - \beta_0 \Delta s \dfrac{d_1}{d'}\dfrac{D_1}{D_2}\left[C_{inb}^{\,n+1} - C_{inbb}^{\,n+1}\right] \end{array}\right\} \end{cases}$$

**For Neumann Boundary Condition:**

$$D_f = D_{ic}$$

$$\frac{\partial C_s^{\,n+1}}{\partial n}\Big|_f = 0$$

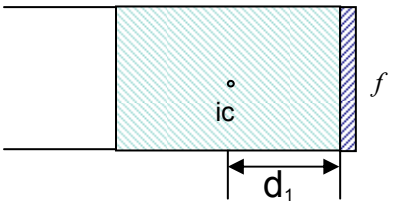


So we have: $C_f^{\,n+1} = C_{ic}^{\,n+1}$

The contribution of all terms for internal faces is

$$\begin{cases} \alpha_{ic} = \sum_{faces}\left[\dfrac{\overline{U}}{2}\Delta s - \beta_0 \Delta s\right] \\ \alpha_d = \sum_{faces}\left\{-\dfrac{\overline{U}}{2}\Delta s C_{ic}^{\,n}\right\} \end{cases}$$

**For Dirichlet Boundary Condition:**

$$D_f = D_{ic}$$

$$C_f^{\,n+1} = C_0$$

And we have: $$\frac{\partial C_s^{\,n+1}}{\partial n}\Big|_f = \frac{C_0 - C_{ic}^{\,n+1}}{d_1}$$

The contribution of all terms for internal faces is

$$\begin{cases} \alpha_{ic} = \sum_{faces}\left[\frac{D_f}{d_1}\Delta s\right] \\ \alpha_d = \sum_{faces}\left\{-\overline{U}\Delta s C_0 + \frac{D_f}{d_1}\Delta s C_0 + \beta_0 \Delta s C_0\right\} \end{cases}$$

**Example:**

A domain with interface at the middle of x-axis. There is a jump of $C_s$ at the interface. The diffusion coefficient ratio $D_1/D_2 = 0.2$, solubility ratio $k_1/k_2 = 2.0$. The solution is shown as follows:

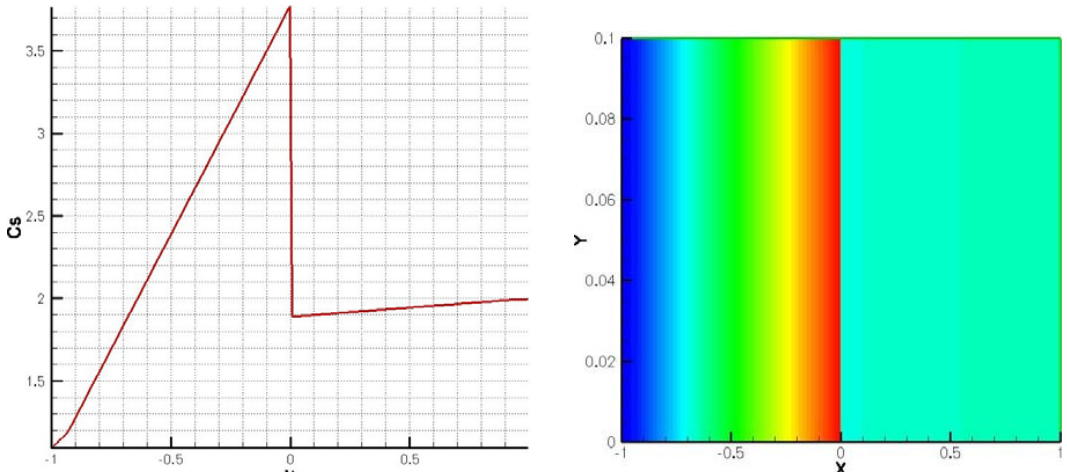


**Figure 28:** Tritium concentration profile and contours across a rectilinear interface

## 5. Phase-I Technical Highlights

In this section we summarize the research performed earlier in Phase-I of this contract.

### 5.1 Formal accuracy and mesh effects: A study of the 2-D driven cavity problem

The 2-D driven cavity problem, investigated by Ghia et al [15] can provide a convenient means to bench mark steady state incompressible flow results. The lid of a unit square filled with incompressible fluid of unit density, is moved in the horizontal direction at unit speed. The coefficient of viscosity of the fluid is selected to match the desired Reynolds number. The case where Re = 1000 has been chosen for the present set of comparisons. Fig. [29] shows the streamline pattern for such a flow. Two low speed circulation regions in the lower corners, a main vortex in the center of the domain, and a developing circulation region in the top left are typical of this flow. Velocity profiles at the center line of this channel are compared with the results of Ghia et al [15].

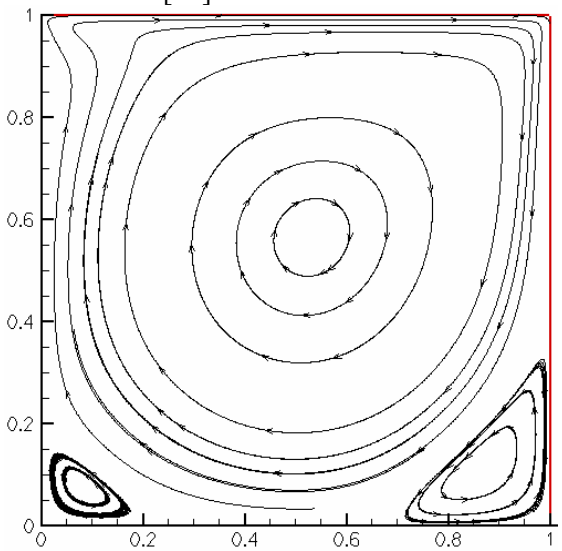


**Figure 29:** Driven cavity at Re = 1000

Structured as well as unstructured meshes were used to study this problem. In the structured mesh case, three different mesh resolutions were used: 31x31, 61x61, 121x121. This provides a spread of mesh resolution that can be used to assess the formal order of accuracy of the solver.

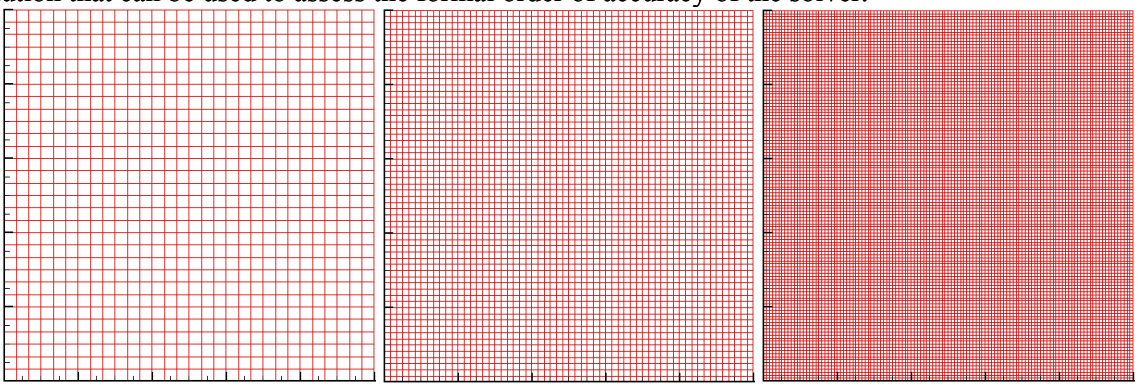

**Figure 30:** Three different structured mesh resolutions used

The x-component of velocity, u, was extracted along the y = 0.5 line in this domain, and the y-component of the velocity, v, was extracted along the x=0.5 line. An error estimate was computed at the extremal locations on these various plots for each mesh resolution. Fig. [31] shows the velocity profiles for the three meshes used, and a grid convergence plot, showing the reduction of error with decreasing mesh size.

A slope of about 2 of this curve indicates the second order accuracy of the basic flow solver. This is shown in Fig [32]. Convergence to all of these solutions has been observed to be uniform and smooth at a time step of 0.01.

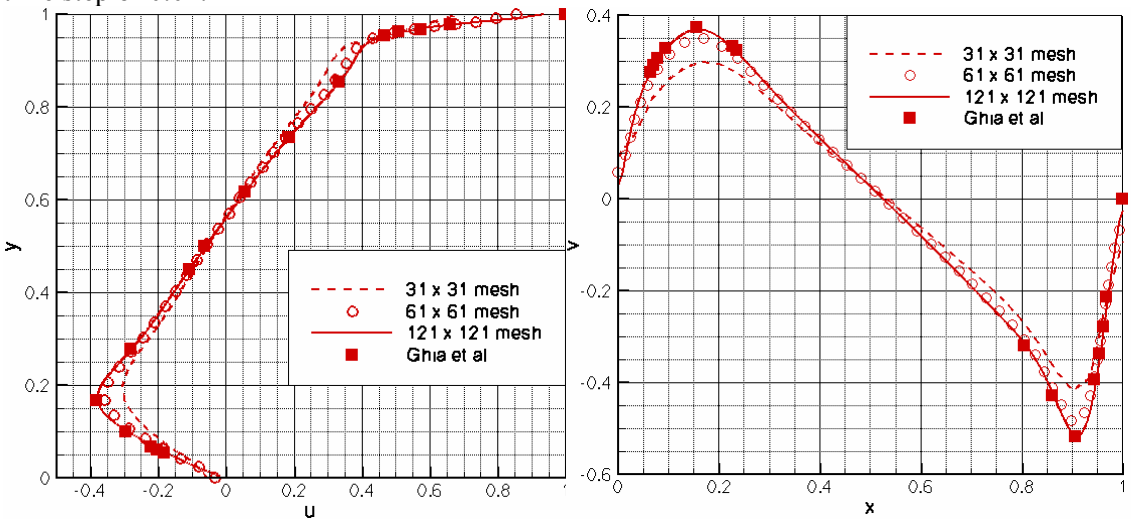


**Figure 31:** Velocity profiles for the three meshes compared with Ghia et al

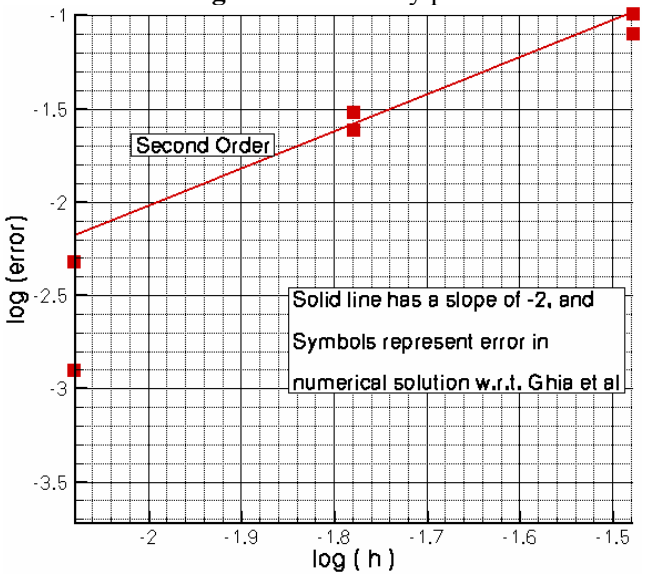


**Figure 32 :** Mesh convergence for the driven cavity problem using uniform structured meshes.

We have attempted to use various types of unstructured triangular meshes, ranging in the degree of smoothness and the minimum cell size. Three different meshes were initially selected, corresponding to a boundary cell face length of 1/20, 1/40 and 1/80, as shown in Fig. [33].

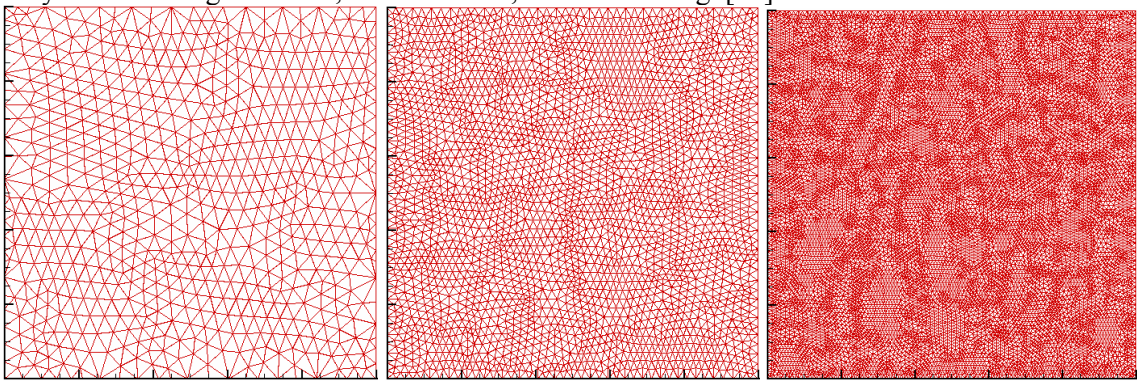

**Figure 33 :** Three unstructured mesh resolutions used

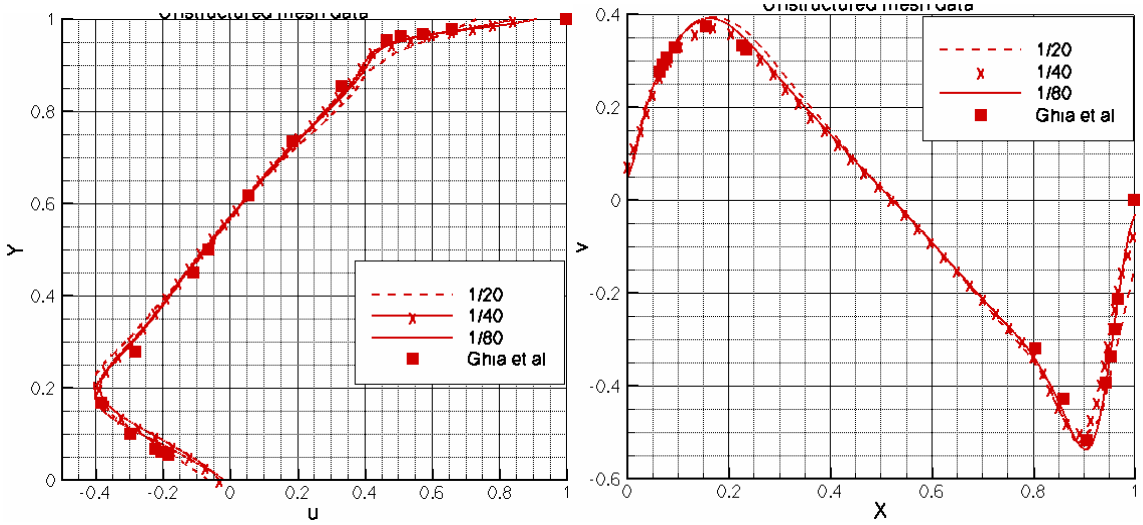


**Figure** 34: Velocity profiles for triangular meshes shown in Fig. [16]

The next series of tests was performed to study the effect of mesh severe mesh stretching on the accuracy of numerical results.

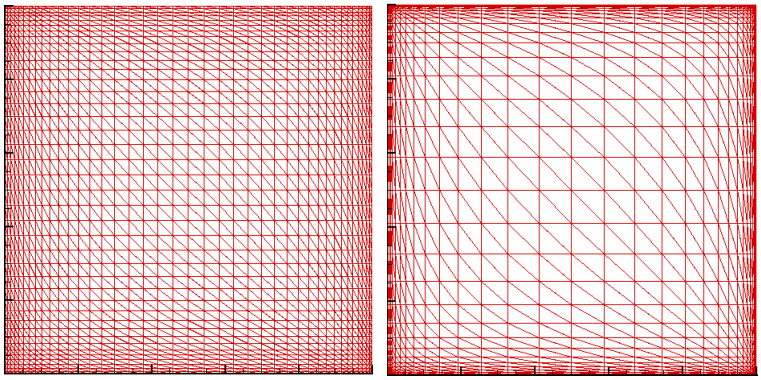

**Figure** 35: (above) Examples of stretched unstructured meshes used and (below) sample results

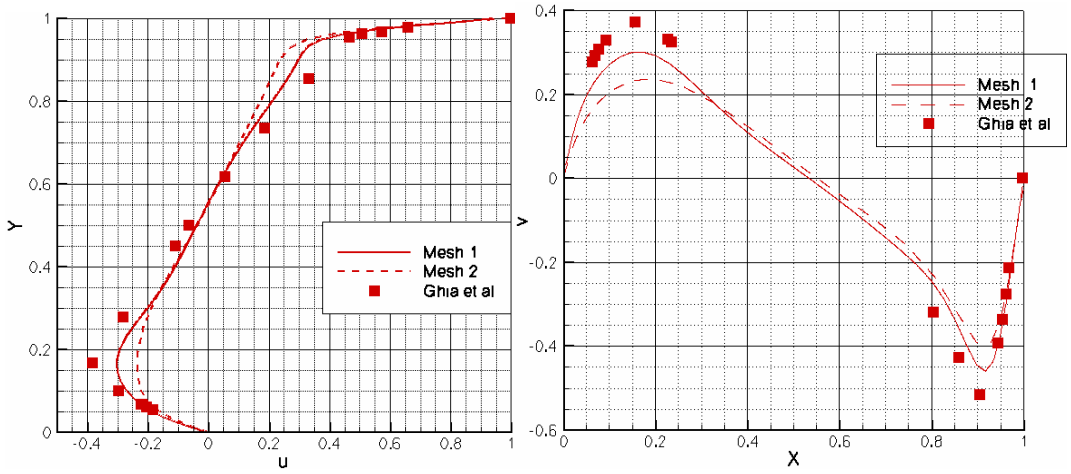

## 5.2 Two-Dimensional Hartmann channel flow

The two-dimensional Hartmann channel flow is a simple extension to the purely hydrodynamic case, and can be used to judge the accuracy of Pressure-Poisson solvers on non-uniform meshes. Hartmann layers (of thickness 1/Ha) form at the side walls of a 2-D channel in the x-y plane where a magnetic field is applied in the y-direction. Within the 2-D framework, current can then only flow in the z-direction, and any electric field present may only exist in the z-direction. Figure [36] shows a schematic of the flow.

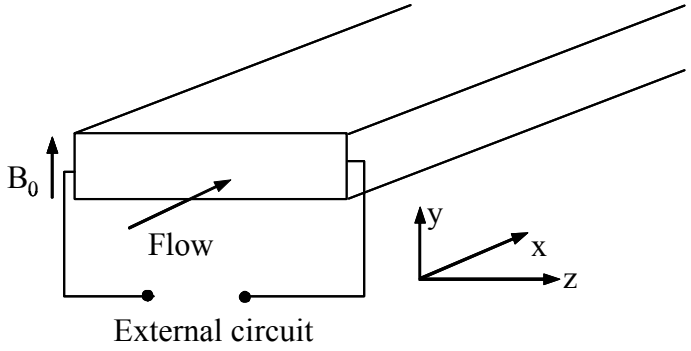


**Figure 36** : Schematic of Hartmann channel flow

Exact solutions can be found to such a flow with insulating walls, assuming a uniform electric field $E_z$ in the z-direction. The expression for the u-component of velocity can be shown to be (Ref. Sutton and Sherman[52]):

$$\boldsymbol{u} = \frac{1}{\boldsymbol{Ha}^2}\left(\frac{1}{\mu}\frac{\partial \boldsymbol{p}}{\partial \boldsymbol{x}} + \boldsymbol{M}^2\boldsymbol{E}_z\right)\left[\frac{\cosh(\boldsymbol{y}*\boldsymbol{Ha})}{\cosh(\boldsymbol{Ha})} - 1\right]$$

If this expression is integrated over the non-dimensional width of the channel in the y-direction, we get the total volumetric flow rate per unit depth in the z-direction:

$$\boldsymbol{q} = \int_{-1}^{1} \boldsymbol{u}\, d\boldsymbol{y} = \frac{2}{\boldsymbol{Ha}^2}\left(\frac{1}{\mu}\frac{\partial \boldsymbol{p}}{\partial \boldsymbol{x}} + \boldsymbol{Ha}^2\boldsymbol{E}_z\right)\left[\frac{1}{\boldsymbol{Ha}}\frac{\sinh \boldsymbol{M}}{\cosh \boldsymbol{M}} - 1\right]$$

The above expressions use an arbitrary value of the pressure gradient in the x-direction. This number may be either specified *a priori*, or adjusted to match a pre-selected mass flow rate. It is often found convenient to set the electric field term to zero in the above expressions. Numerically, these expressions yield a simple exponential behavior at the walls as the Hartmann number increases. Power series expansions are required beyond a Hartmann number of about 500 in lieu of the hyperbolic functions for computer calculation.

HIMAG was used to simulate this flow using a mesh that is stretched to match Ha = 500. (i.e., 7-8 cells within a space of 1/500 from each wall). A channel length of 30 units and a width of 2 units was selected. Magnetic field component By was set to zero near the inflow and increased to 1 linearly between 3<x<4. It is then held constant. Figures [37] show the velocity profiles and comparison with the exact solution of the velocity extracted from near the channel exit. Errors in the computed and exact pressure gradient are shown in Table [2]. In all, a fair comparison has been observed, with a tendency to betterment at higher Hartmann numbers.

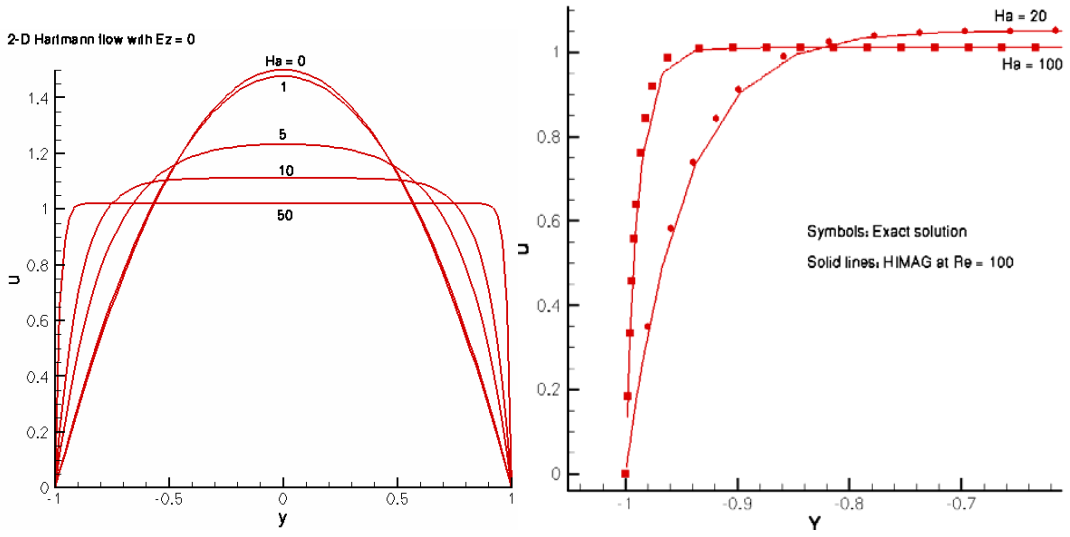


**Figure 37:** Velocity profiles and comparison with the exact solution for 2-D Hartmann flow

| | Re = 200 | | | | Re=10000 | |
|---|---|---|---|---|---|---|
| | Ha = 0 | Ha = 20 | Ha = 50 | Ha = 100 | Ha = 0 | Ha=500 |
| - dp/dx (exact) | 0.03 | 4.21053 | 25.51 | 101.01 | 3e-4 | 25.0501 |
| - dp/dx (HIMAG) | 0.0306 | 4.20616 | 25.4965 | 100.991 | 2.949e-4 | 25.0609 |
| Error (%) | 2 | 0.1038 | 0.0529 | 0.0188 | 1.7 | 0.0431 |

**Table 2 :** Comparison of 2-D Hartmann channel flow with the exact solution

## 5.3 2-D MHD flow past a square cylinder

Viscous flow past a cylinder (circular or rectangular) is a classical problem used to demonstrate temporal and spatial accuracy of flow solvers and the effect of MHD on eddy propagation. Here, we study the flow past a square cylinder, mainly to delegate non-orthogonality errors in the mesh to a different test case. A square of unit side length is placed in a 2-D domain as shown in Fig. [38]. A uniform free stream velocity of 1 was imposed. Flow was studied for a fixed Reynolds number of 200. A unit magnetic field was applied in the y-direction (transverse field). The setup has the advantage that the Poisson equation for electric potential need not be solved, since the potential must be constant in the x-y plane, though it can have a constant z-gradient, which we assume to be zero.

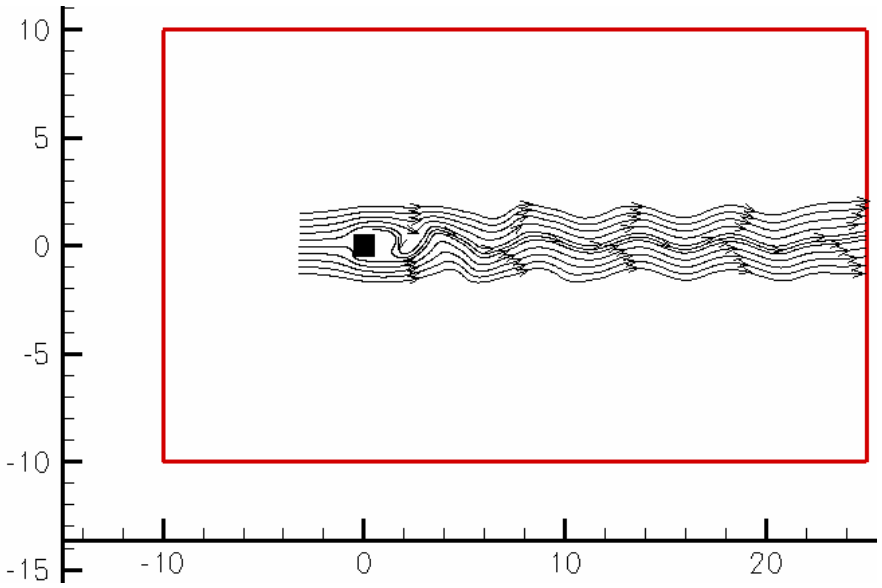


**Figure 38** : Computational domain used for square cylinder study

A magnetic field applied in the y-direction in such a flow has a tendency to first reduce the intensity of the vortex street behind the cylinder, and then subsequently to even shorten the separation bubble in the wake region, leading eventually to a perfectly symmetric (Hele-Shaw type) flow. This is in general agreement with the observations of Frank et al [14].

The effect of an applied magnetic field is fairly strong in this case even at low values of the Hartmann number and interaction parameter. Figure [39] shows the streamline pattern computed for Hartmann numbers 0, 10 and 50, and a Reynolds number of 200 (based on cylinder side length). This corresponds to interaction parameters of 0, 0.5 and 12.5 respectively.

There is a large amount of experimental data pertaining to flows of this nature(e.g., ref [20]). The natural extension to a circular cylinder and the use of non-orthogonal meshes is imminent and will be taken up in due course.

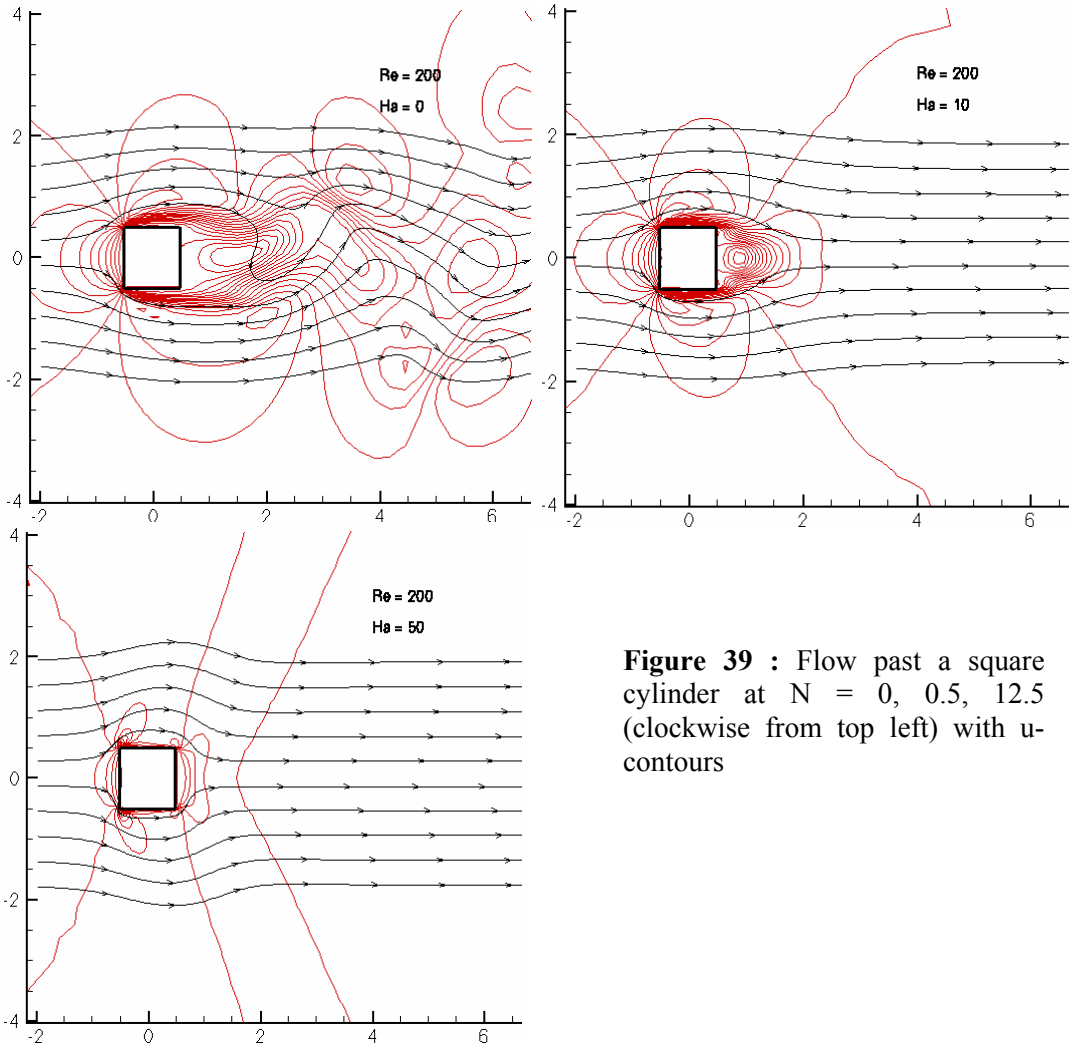


**Figure 39 :** Flow past a square cylinder at N = 0, 0.5, 12.5 (clockwise from top left) with u-contours

## 5.4 The Broken-dam problem with MHD

The "broken dam" problem of Martin and Moyce[26] is a popular benchmark problem used in the study of time accurate free surface flows. A liquid column (2x1) is initially supported by walls on either side. At the onset of the calculation, the wall (dam) on the right side is instantaneously removed, causing the liquid column to collapse. Accurate measurements of the advancing free surface front have been reported in the literature. We investigate here a potential MHD variant of this problem.

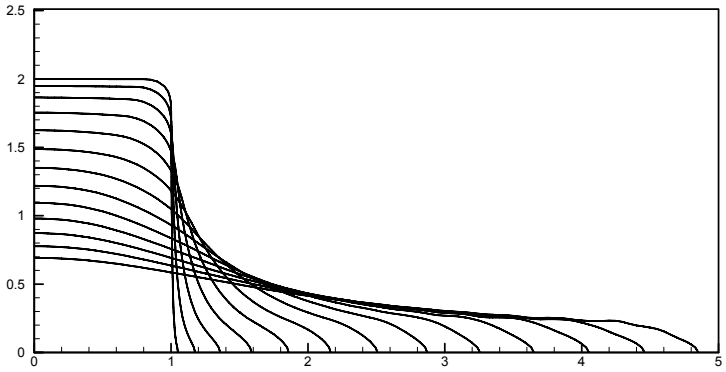


**Figure 40 :** Numerical computation of the broken dam problem – free surface variation in time

As in the square cylinder test case, a magnetic field applied in the x or y-directions seems to provide strong interactions in this situation as well. It is perhaps therefore convenient to design an experiment to study the MHD variant. Here, we study a magnetic field held constant in the region x > 1.5 and y > 0.3 and linearly tapered away from this region. The Hartmann number is 316, based on a characteristic length of 1. Constructing a Reynolds number computed as:

$$\mathrm{Re} = \frac{\rho L\sqrt{2gL}}{\mu}$$

where L = 1, and g is the acceleration due to gravity (also 1). The coefficient of viscosity was selected as 0.001. With this combination, we get a Reynolds number of about 1414. The interaction parameter can be estimated to be about 71. A free surface plot is shown in Fig. [41].

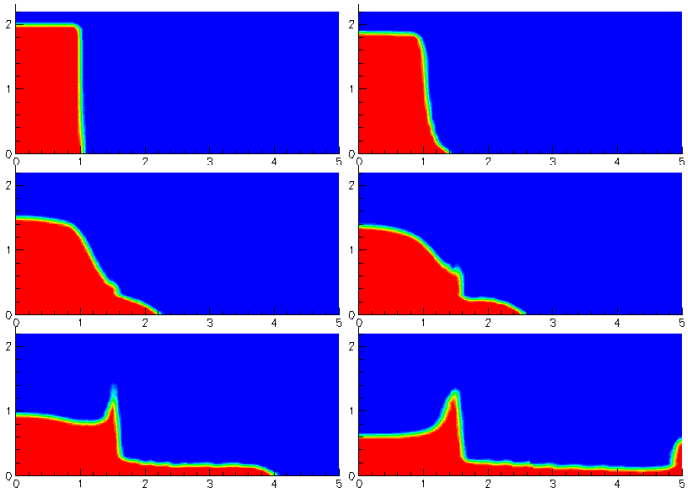

**Figure 41**: Time variation of the free surface for a broken-dam problem with MHD.

## 5.5 Canonical interpretation of complex flow simulations

Among the goals of the benchmarking study described here, we expect to use the "unit" problems to diagnose and understand problems involving more complex physics. An experimental facility at UCLA, named MTOR is being used to perform free surface studies on film flows with conducting walls on all sides but one (the upper). There is a 3-D distribution of magnetic fields, and the Reynolds as well as Hartmann numbers encountered are rather large. The flow Reynolds number is in the vicinity of 10,000, while the Hartmann number is about 1300. There is a significant MHD interaction in the flow, as can be seen in the free surface contours presented in Fig. [43]. Fig. [43c] shows a section of the flow where the flow detaches from one of the walls. This effect and the overall trends seen in the numerical study using HIMAG, have been observed experimentally. Narula et al [35] have presented a study with this data.

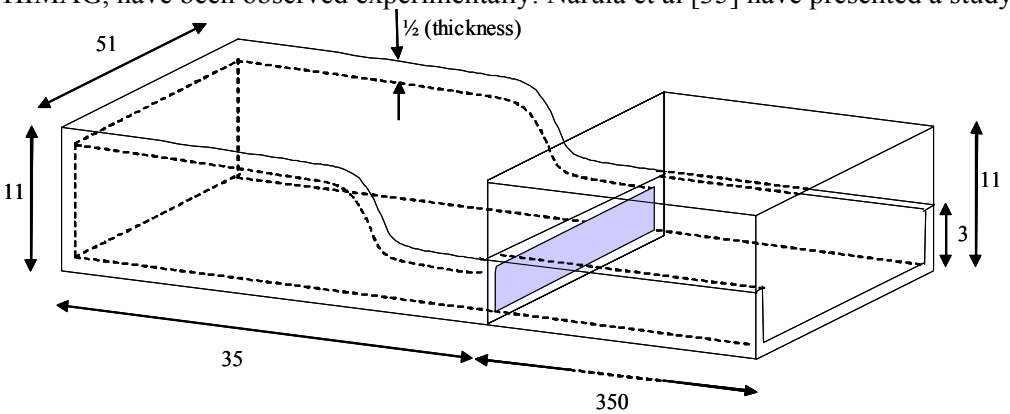


**Figure 42** : NSTX film flow experiment geometry. Dimensions in mm, walls are made of steel.

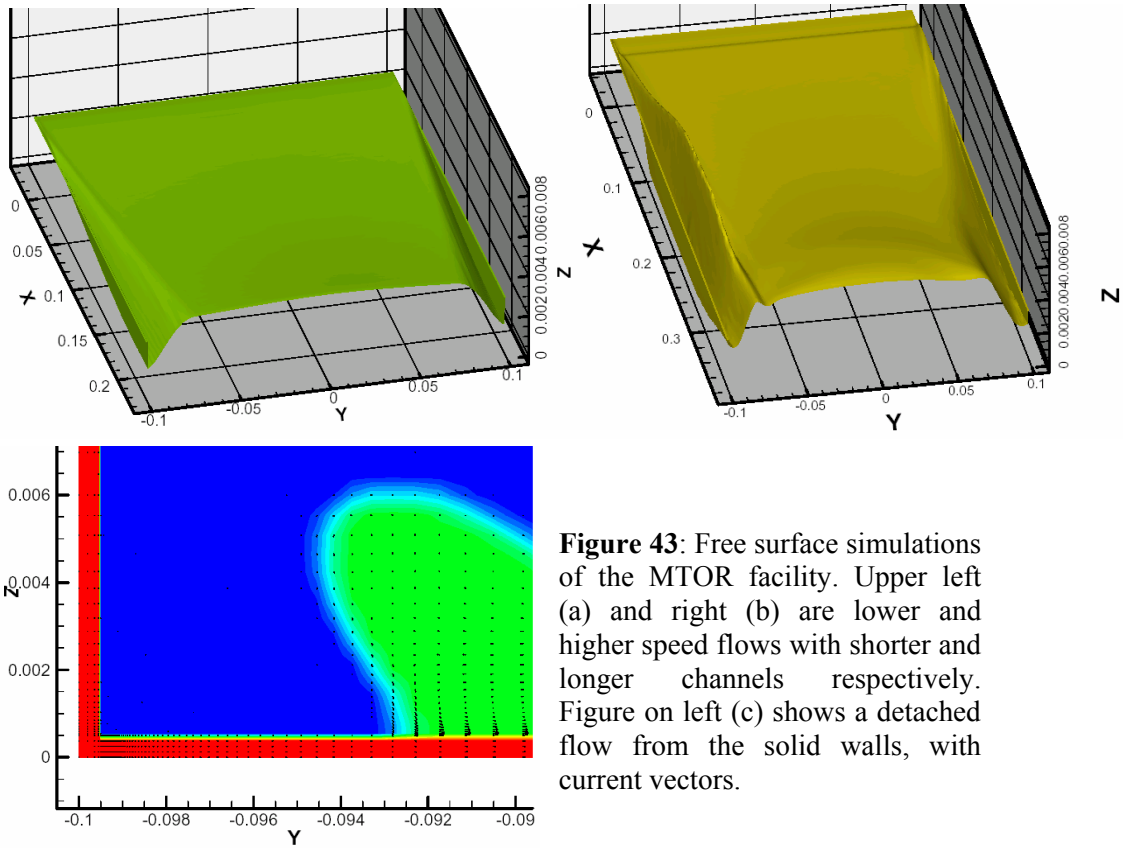


**Figure 43**: Free surface simulations of the MTOR facility. Upper left (a) and right (b) are lower and higher speed flows with shorter and longer channels respectively. Figure on left (c) shows a detached flow from the solid walls, with current vectors.

Qualitatively, the following describes the process used in achieving these simulations and deriving a physical interpretation from them. High density ratio, surface tension, wall conduction, high surface deformation in a region of non-uniform grid spacing caused by the need to resolve high Hartmann numbers, and 3-D variation of applied magnetic field are the important physical issues encountered in this simulation. Wall conduction, high Hartmann number issues have been addressed earlier, and the effect of non-uniform mesh spacing has been dealt with earlier in this report as well as in prior reports related to HIMAG. The accuracy of free surface capture and the stability of the level set procedure were established in an earlier work based on the analysis of simpler problems, such as the broken-dam, oscillating droplet and rising bubble. Ni et al [37] have presented a methodical validation procedure for this purpose. The experience gained in the development of canonical problems has proved to be invaluable in the study of the MTOR experiment.

Sample diagnostic tests on jet flow in the LIMITS experiment (Brooks et al [8]) have been shown in Fig. [44]. The surface of the jet as it enters a magnetic field gradient is shown, and inflow and outflow cross sections, to demonstrate mass conservation by the level set procedure are shown alongside. Pressure and density contours at a jet cross section are shown in Fig. [44 c,d]. These are used to correlate with the expected value of pressure rise across a circular jet, obtained from surface tension considerations, presented by Ni et al [37].

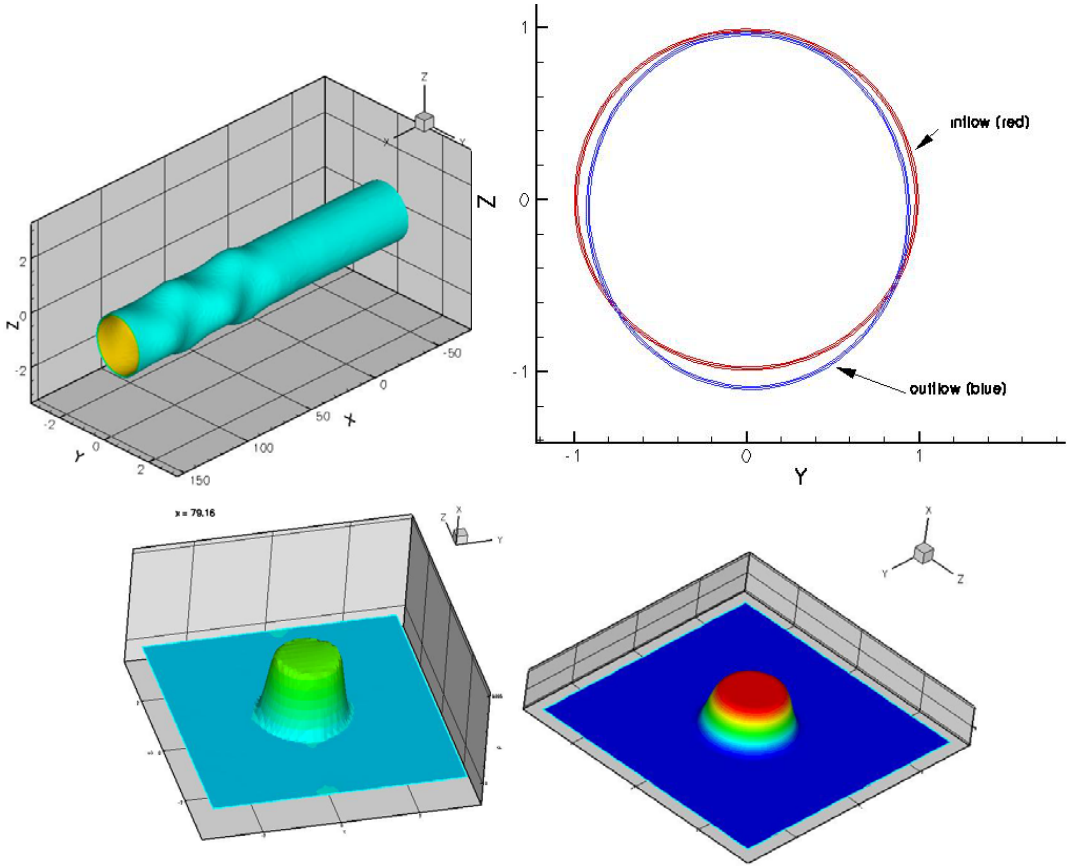


**Figure** 44: (a) Top-left, free surface of the jet in the LIMITS simulation, (b) Cross sections of the jet at inflow and outflow, (c) Pressure profile at a cross section, (d) density profile at a cross section of the jet. $\Delta p = 1/(R * We)$ is the analytical result, where R is the radius of the cross section and We is the Weber number

## 5.6 Setting up HIMAG for fully developed flow

HIMAG has been recently modified to run in a "fully developed" mode. Here, the user has an option to prescribe a pressure gradient in, say, the x-direction and use a single cell in that direction while generating the mesh. The grid in the y-z plane can be arbitrary, and include conducting walls, multiple materials and can even be partitioned to run across parallel processors. The domain boundaries in the x-direction are set as Neumann-type, and all variables are simply copied from the cell center, thus representing the fact that there are not gradients of flow quantities in the x-direction, except for the gradient of pressure, which actually drives the flow. Initial velocity can be set to zero. There is no need for the pressure Poisson solver, while a Poisson solver for the electric potential is yet required. Fig. [45] shows a typical sketch for a square duct with conducting walls for which a mesh is generated for a Hartmann number of 500, and has been partitioned into 8 processors.

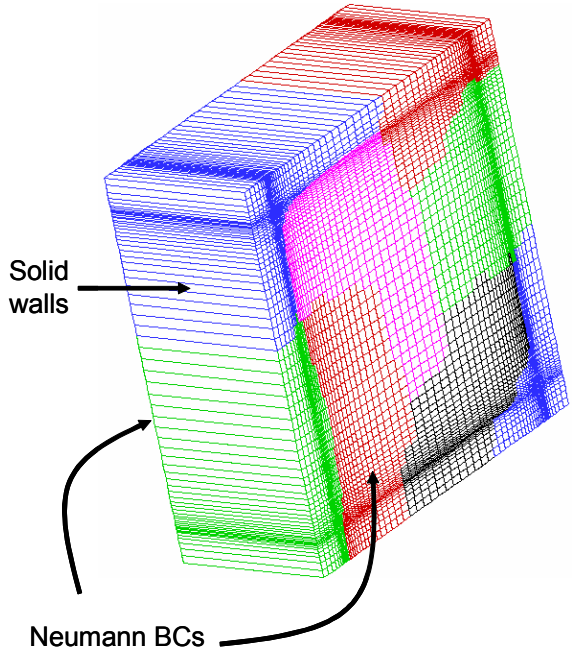


**Figure 45 :** Setting up the fully developed flow problem with HIMAG

Detailed validations of HIMAG with the analytical solutions of Shercliff [47] and Hunt [16] have been reported to some extent in earlier reports, and to some extent are ongoing, particularly for high Hartmann numbers, where some effort is being made in increasing the speed of convergence. We present here a preliminary result to demonstrate the ability of the code to model walls of multiple conductivities. Fig. [46] shows a square duct in which magnetic field is applied in the y-direction. A conducting wall of thickness 0.1 units is present on all sides, and is conducting in the Hartmann region and insulating in the side-wall region. Current lines are shown, superposed over velocity contours. A comparison with the analytical solution of Hunt is shown in Fig. [46].

In order to assist newer users to learn HIMAG, a user interface has been prepared which can be used to set up simple rectilinear geometries and import structured-type meshes into HIMAG's .ux format. A provision has been made for high Hartmann number flows whereby the user may specify the Hartmann number and a suitable grid quality will be pre-selected by the program, providing a smooth transition into a wall region if present. This work will be reported elsewhere.

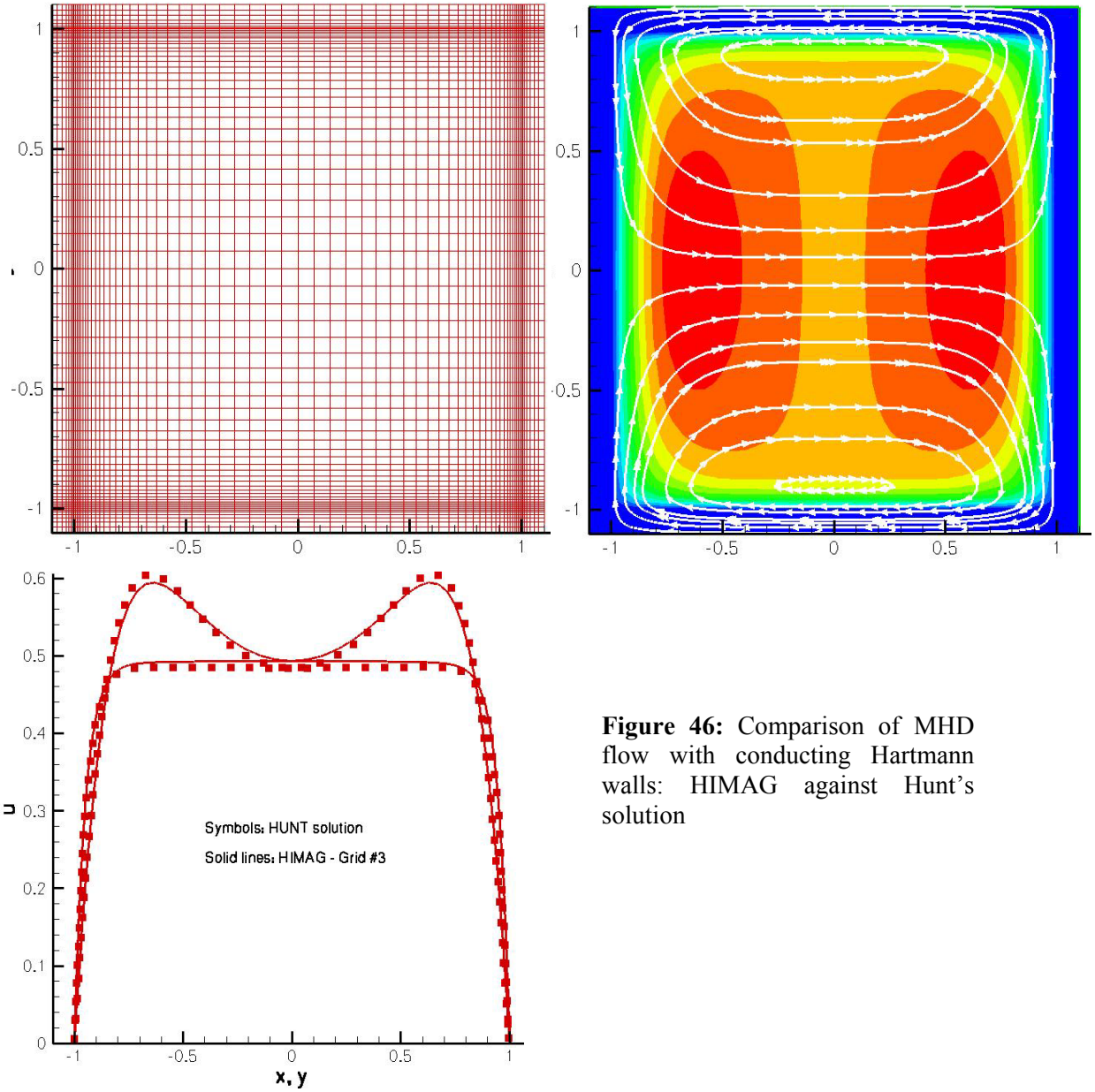


**Figure 46:** Comparison of MHD flow with conducting Hartmann walls: HIMAG against Hunt's solution

## 5.7 Flow development and uniqueness

J.C.R. Hunt[17] formally proved in 1969 (following an initial result from H.K.Moffat,) that MHD flow in a constant (arbitrary) cross section duct under the action of a transverse magnetic field is uniquely specified by certain parameters: *either* the pressure gradient in the axial direction, *or* the volume flow rate, *and* either the electric current leaving the walls of the duct at each point on its exterior, *or* the electric potential at these points. He further deduced that no secondary flow can exist under these conditions in a fully developed duct flow.

This result is very interesting, and invaluable in developing canonical problems for MHD codes. In comparing solutions obtained from codes using the inductionless approach (the phi-formulation) with codes using the induced field (B-formulation) approach, we are some times faces with the fact that boundary conditions may not always be identically imposed. This can lead to a mismatch in solution, which nevertheless, does not violate the uniqueness theorem. Another source of discrepancy is the non-convergence of Poisson solvers when using the inductionless formulation. While the convergence of these solvers at each time step is not essential for a steady flow solution, we have observed that slow convergence (particularly at high Hartmann numbers) can lead to solutions that are asymptotically close to the correct one, but never quite exactly the same. Fig [47] shows the benefits of using a conjugate gradient solver that is now available in HIMAG to achieve faster convergence very efficiently.

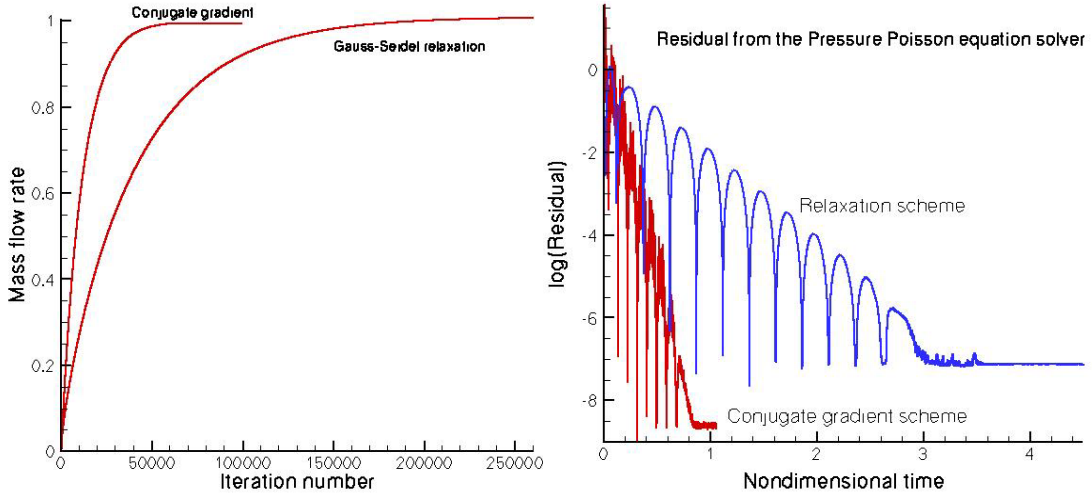


**Figure** 47 : Time history of mass flow rate and pressure Poisson residual for two solvers

We are able to recover the 2-D fully developed solution from adequate solution convergence (fig. [48]) , and errors may be attributed to the non-convergence, as can be seen by the matching solution obtained using the conjugate gradient solver shown in Fig. [49]. The marching of the 3-D solver can go through a series of pressure profiles as seen in Fig. [50], giving a huge spread in the possible error in predicting pressure gradient until convergence.

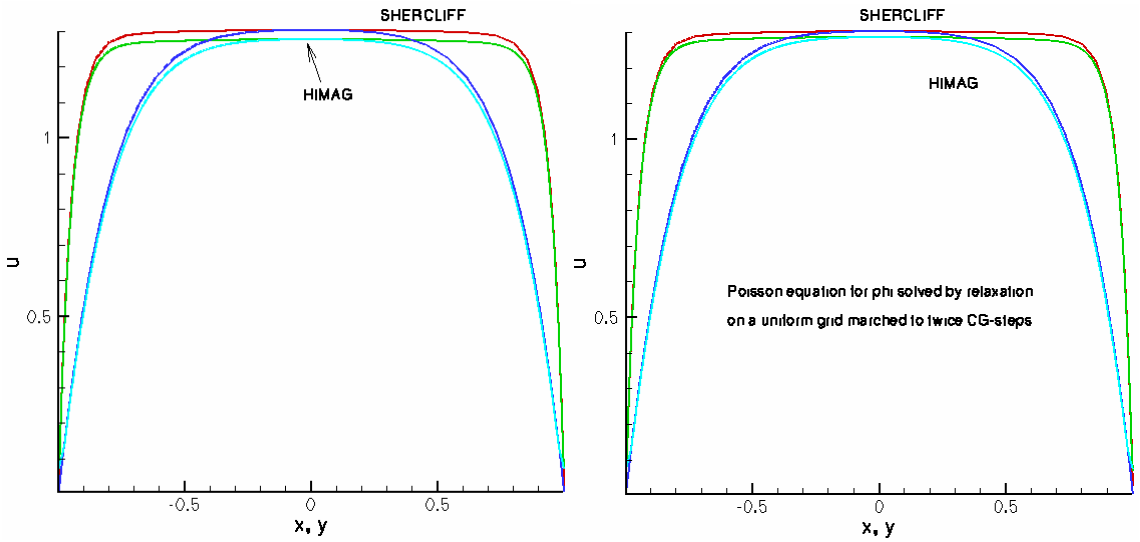


Figure 48: Solution from HIMAG run in a 3-D mode with Shercliff's solution (left), and 2-D-fully developed mode with insufficient convergence (right)

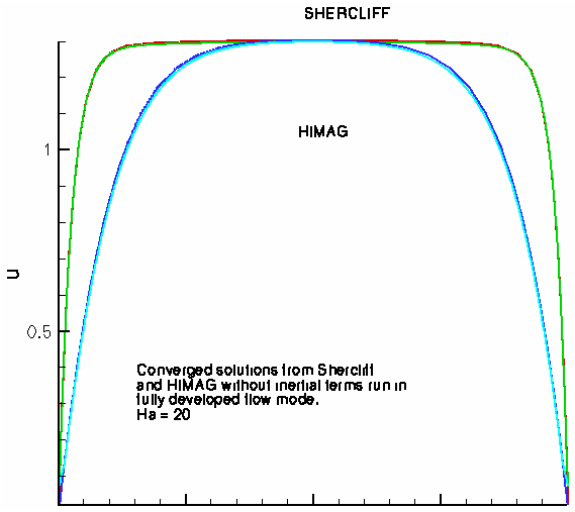


**Figure 49 :** Fully converged solution from HIMAG compared with Shercliff

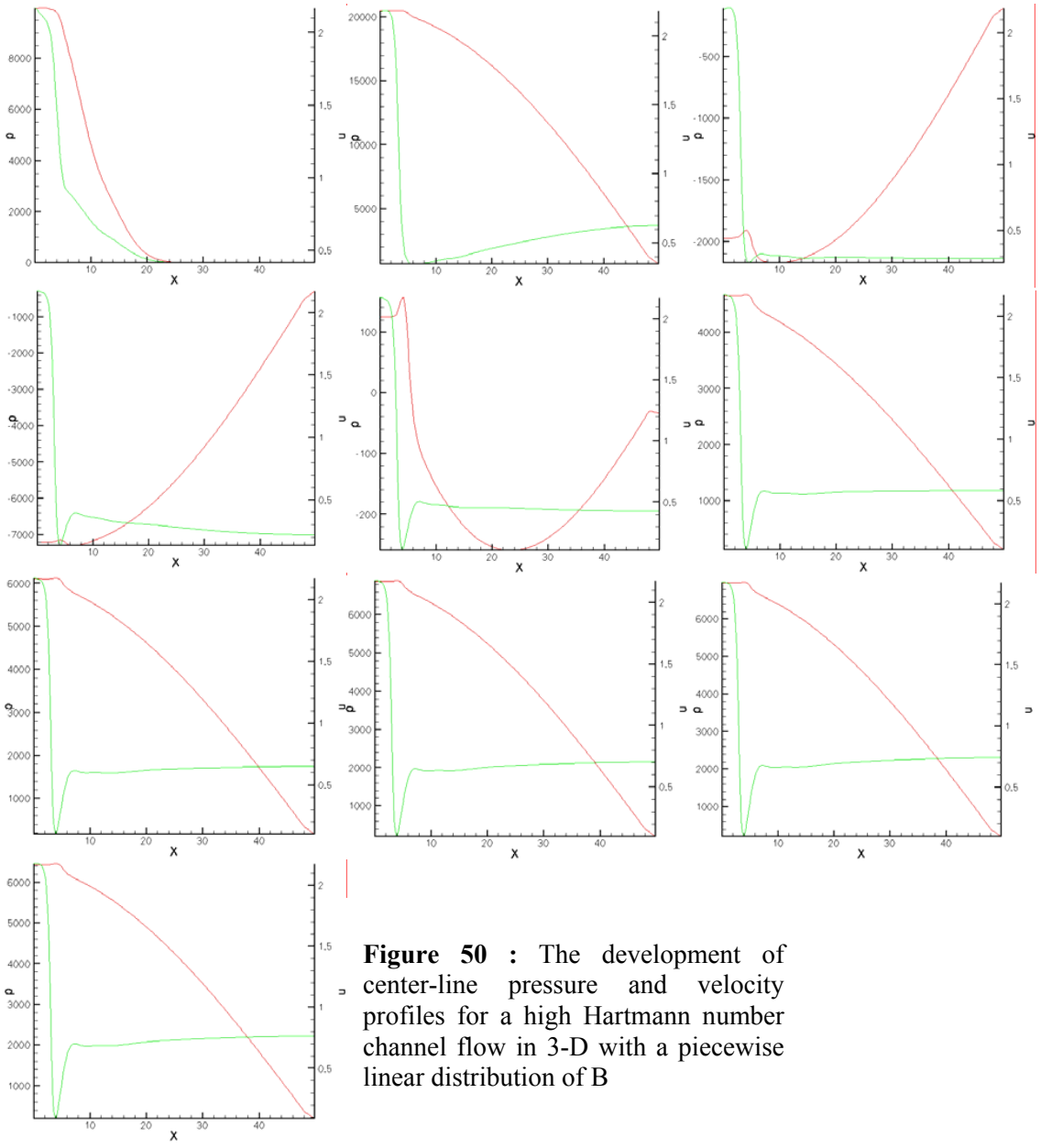

**Figure 50 :** The development of center-line pressure and velocity profiles for a high Hartmann number channel flow in 3-D with a piecewise linear distribution of B

We have observed certain situations which may potentially circumvent the criteria of Hunt's theorem. These include, primarily, the provision for alternate current paths. Fig. [51] shows a study where a channel with conducting walls has a slotted tubing insert intended for pressure equalization. In a 3-D solver, the applied magnetic field is ramped up sufficiently upstream, and the ramping causes local pressure gradients and a pumping force which drives fluid into corner regions of the slotted area (Fig. [51a]). This is a non-unique process, and can potentially affect the flow conditions downstream. Velocity contours across a cross section in the downstream region (where the magnetic field is constant) are shown in Fig. [51b].

We are presently investigating if this represents a violation of some of the assumptions of the uniqueness theorem. Yet another case has arisen in the course of our investigations, pertaining to the manner in which electrical conductivity is interpolated at a computational cell located at a material interface. We have been able to obtain solutions involving strong negative velocities in the slot region by using a conservative

interpolation, as well as a smooth positive velocity with an upwinded interpolation, as seen in Fig. [52]. In Phase-II we have substantially addressed the diversity of phenomena that can arise in FCI-related flows, and their enormous sensitivity to boundaries and flow development.

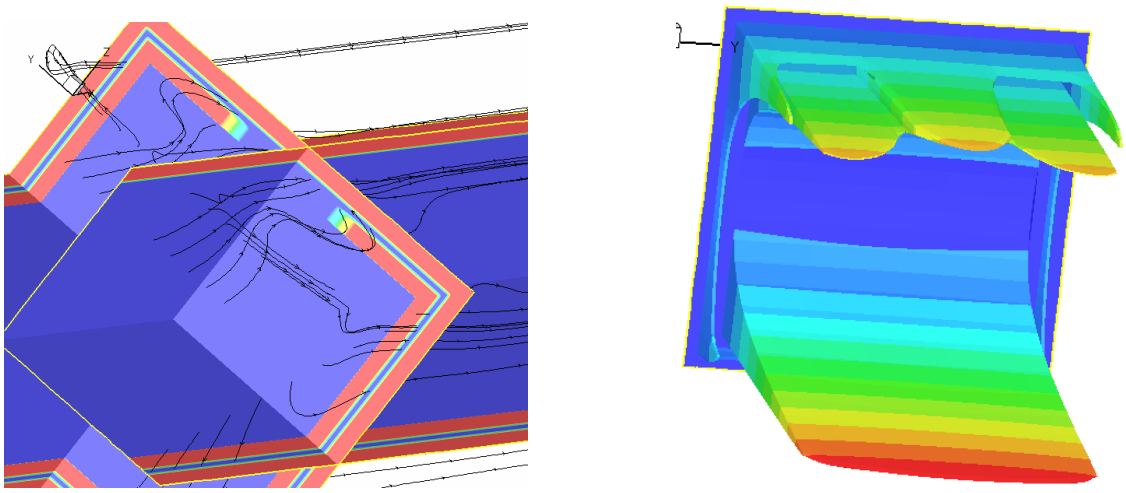

(a) (b)

Figure 51 : Flow entrapment in corner regions of a slotted wall MHD channel. Streamlines migrate from the core of the flow via the slot, propelled by local gradients of magnetic field.

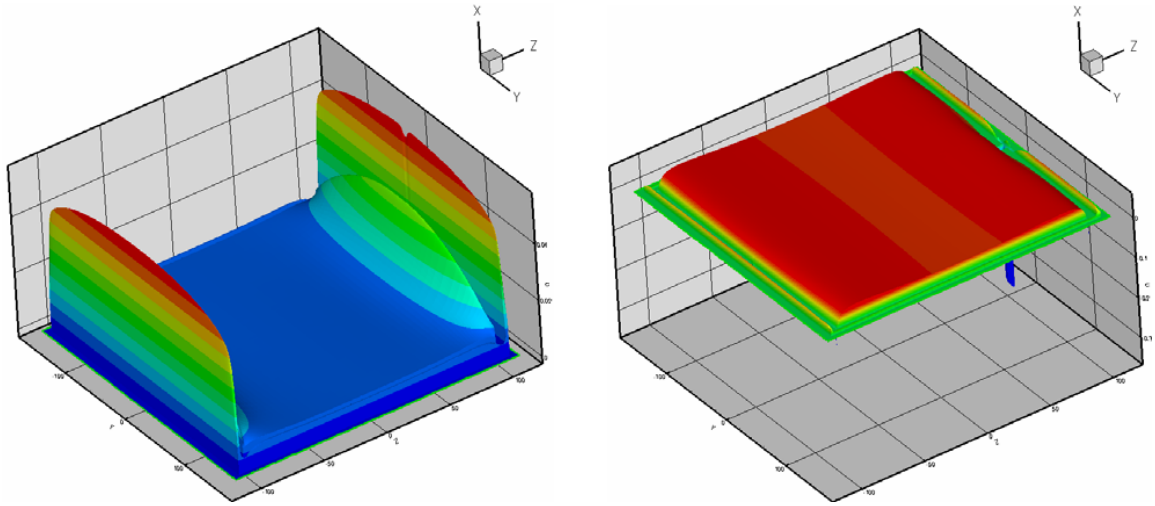

Figure 52 : Different velocity fields obtained by different interpolation techniques at walls.

## 5.8 The 3-D "development" of an applied magnetic field

One of the concerns in the development of a 3-D MHD solver for engineering applications is that the external magnetic field and relevant boundary conditions are some times rather hard to deduce. This is important in the design of benchmark problems, since different solvers can advance magnetic fields in different ways, and an initially non-physical distribution of magnetic field can present non-unique numerical evolution of the flow. For instance, consider the experimentally determined magnetic field variation in the MTOR facility at UCLA shown graphically in Fig. [53].

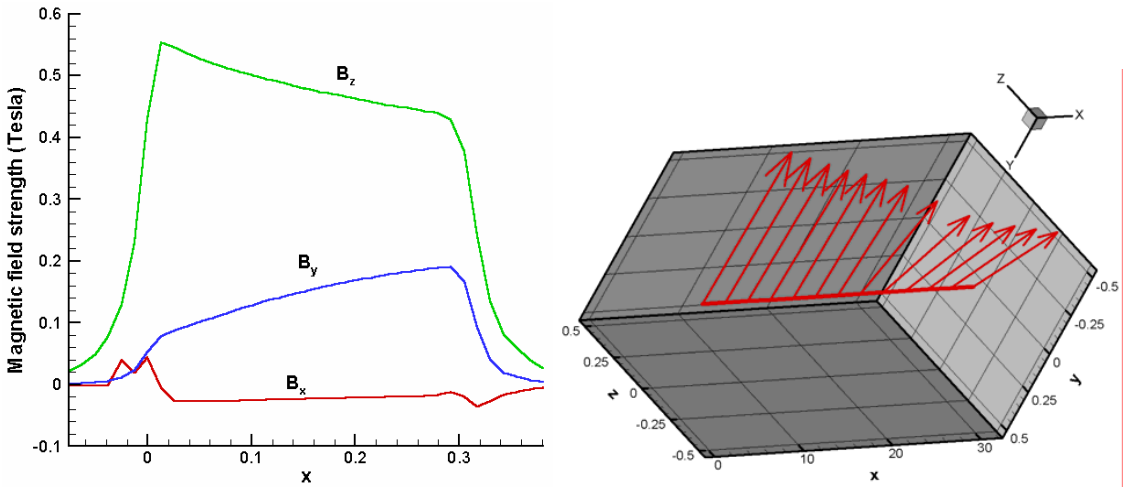


**Figure 53**: Sample magnetic field distributions measured along test section centerline of LIMITS (Ref. Brooks[8]) (left) and MTOR (Ref. Narula[35]) (right) experiments

The main concern in transferring this data to 3-D solvers is that these field distributions are not divergence and curl free. If they were reconstructed from a precise knowledge of their sources (coil windings, permanent magnets, etc.) a self-consistent field could have been determined. We present a technique which takes resort to the Biot-Savart law of electromagnetics to reconstruct a 3-D field given a 1-D distribution of field components, thus enforcing divergence and curl-free fields in the computational domain.

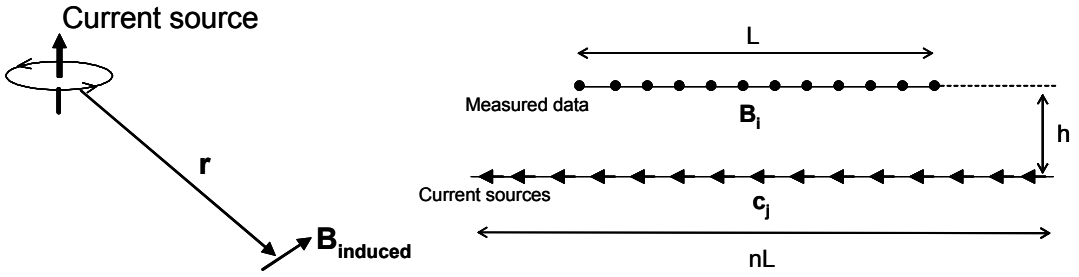


Figure 54 : Notation for Biot-Savart law (left), Placement of sources in the present model (right)

Figure [54] shows the notation we use in this computation. A small current element $\delta \boldsymbol{I}$ induces a magnetic field $\delta \boldsymbol{B}$ at a position vector **r** given by the Bio-Savart law:

$$\delta\vec{B} = \alpha \frac{\vec{r} \times \delta\vec{I}}{r^3}$$

where $\alpha$ represents the strength of the source. A given distribution of magnetic field can be reconstructed from a sequence of current sources as shown in Fig. [54] using this law. If there N sources selected to model M measurements, we may form a linear set of N simultaneous equations in terms of the unknown source strengths, as follows:

$$\sum_{j=1}^{N} c_j \delta \vec{B}_{ij} = B_i \quad i = 1...M \quad \rightarrow \quad [A]\{c_j\} = \{B_i\}$$

In general, N may not be equal to M and a least squares approach may be used to obtain a smooth field solution to the above matrix equation, using the following strategy:

$$\underbrace{[A]^T [A]}_{M} \{c_j\} = [A]^T \{B_i\} \quad \rightarrow \quad \{c_j\} = M^{-1} [A]^T \{B_i\}$$

These expressions have been used to reconstruct an exponential distribution of magnetic field with varying gradient in Fig. [55]. We see here the sensitivity of the reconstruction technique to sharp gradients in the field. The number of sources and their placement needs to be optimized to obtain smoothness in the reconstructed field when there are sharp gradients, in order to prevent oscillations.

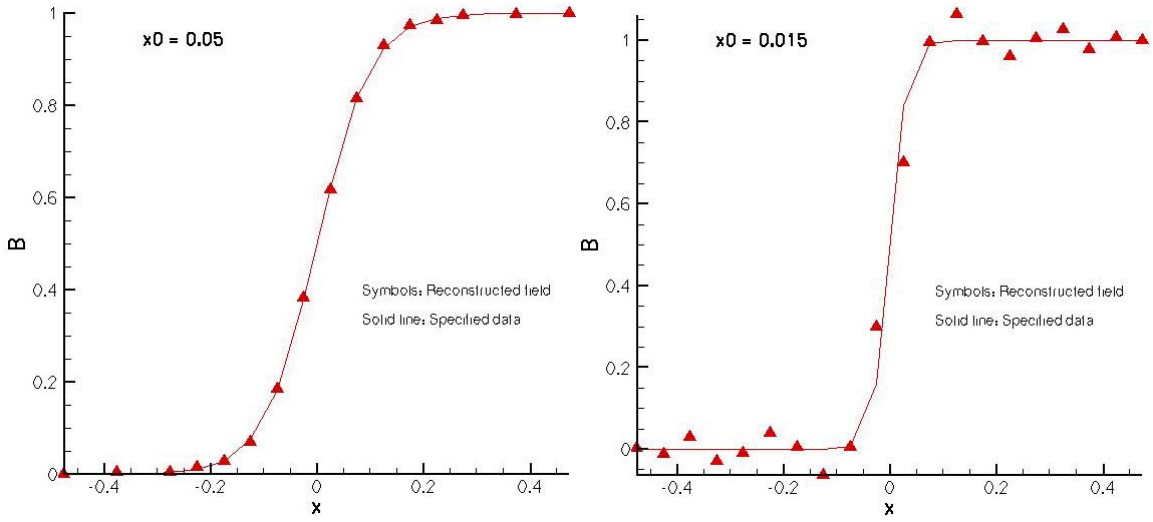


Figure 55: Applied field and reconstructed fields computed by the Biot-Savart technique.

A different approach to this problem, based on deriving the applied field from the gradient of a scalar potential is being investigated in a separate research activity at HyPerComp. It is believed that both these options are useful and will be offered to the users of the code. Simulations using a divergence and curl free magnetic field are more likely to agree with experiments and with codes based on the B-field formulation.

## 5.9 Turbulence modeling

In our phase-I work, we have initiated a RANS type k-e model for turbulence. A setup for an arbitrary set of advection diffusion equations has been provided in HIMAG as a precursor to developing turbulence and transport modeling. This routine may be called with any conserved quantity and it will be advected with local flow velocity using a Crank-Nicholson implicit scheme. This scheme loosely couples with the momentum solver, and sub-iterations or global-iterations are needed for a fully self-consistent solver.

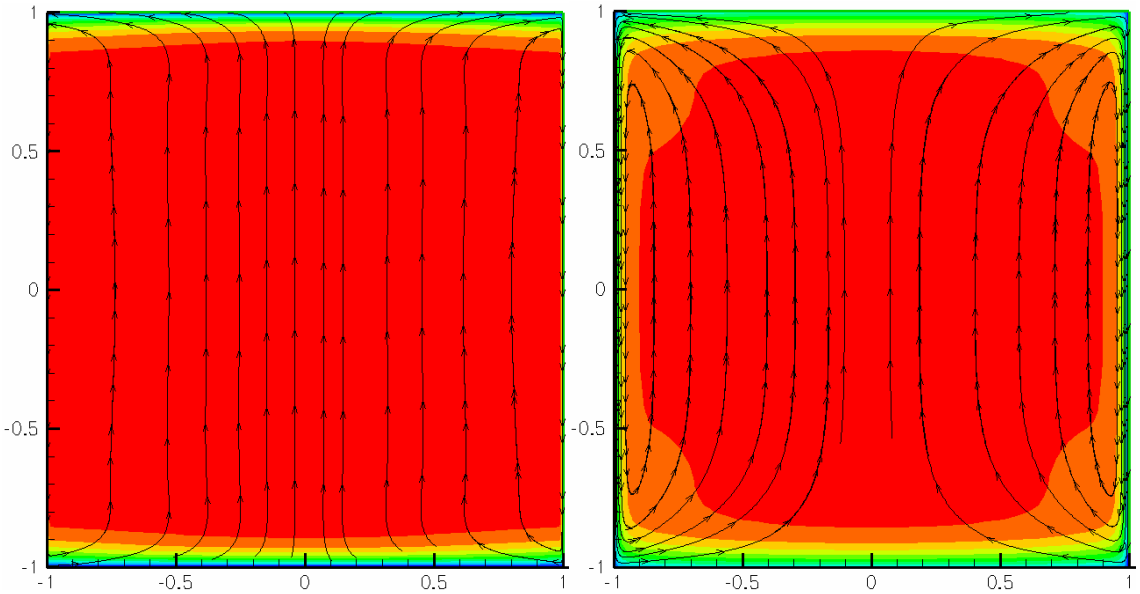

Figure 56 : Current lines and velocity contours in a channel flow at Ha=500, Re = 10,000.

The result in Figure [56] shows a simple zero-equation turbulence model used to simulate high Hartmann number flow. The fundamental assumption in this model is that the Hartmann number is high enough that turbulence is two-dimensional in nature, and eddy viscosity is a constant every where except in the region near the side-wall, where the flow becomes laminar. The development of the k-e model is ongoing at the present time.

## 6.0 Conclusion and future work

The over-arching goal of this development is to create the capability for carrying out virtual experiments in blanket modules, implying predictive capability spanning multiple modes of operation, faithful representation of salient physics processes in the plasma-material interface, liquid and solid media and the relevant interactions among these and external loads. The use of a completely integrated virtual testing of blanket module concepts in the manner envisioned would truly realize the promise of the computer revolution in engineering design, and apply it to the important task of fusion power generation. To this end, we intend to equip HIMAG with the ability to carry out convective and turbulent flow computations, and to perform Tritium transport calculations.

In addition, we sought to develop a database of problems which may be used to experimentally and computationally demonstrate flow features in such a way as to render them useful for code validation and test calibration. We realize that such problems are available in some limited form, for fully developed flows and some external flows, such as flow past a cylinder with insulating walls. We wish to extend the breadth of this problem space, to include new physical features that are of prime relevance to *practical* devices. Work is currently ongoing to make these calculations faster – by an order of magnitude or more. This will change the face of MHD-based design in fusion devices, and HIMAG is ideally poised to take the next leap into this essentially uncharted territory.

## 7.0 References


[1] Abdou, M.A. et al, "US plans and strategy for ITER blanket testing," *Fusion Sc. and Tech.*, 47:3, 475-487, 2005

[2] Abdou, M.A., and the APEX team, "Exploring novel high power density concepts for attractive fusion systems," *Fus. Eng. Des*., **45**, pg. 145, 1999

[3] R.E. Alcouffe *et al*. "DANTSYS 3.0, a diffusion accelerated neutral particle transport code system." LA-12969-M, Los Alamos National Laboratory, June 1995

[4] Barth, T.J., "Aspects of unstructured grids and finite-volume solvers for the Euler and Navier-Stokes equations," von Karman institute lecture series, 1994-05, 1994

[5] Boissonneau, P., "Magnetohydrodynamics propulsion: A global approach of an inner DC thruster," *Energy conversion and management*, **40**, pg. 1783, 1999

[6] Borowski, S.K., "Comparison of fusion/antiproton propulsion systems for interplanetary travel," NASA Lewis (Glen) Research Center TM 107030, 1987

[7] Breuer, K.S., Park, J., Henoch, C., "Actuation and control of a turbulent channel flow using Lorentz forces," *Phys. Fluids*, **16**, No. 4, pg. 897-907, 2004

[8] Brooks, J.N., et al, "Overview of the ALPS program," *Fusion Sc., Tech*., **47**, No. 3, pg. 669-677, 2005

[9] Bühler, L., "Magnetohydrodynamic flows in arbitrary geometries in strong, nonuniform magnetic fields – A numerical code for the design of fusion reactor blankets," *Fus. Tech*., **27**, pg. 3-24, 1995

[10] Bühler, L., "Magnetohydrodynamic flow in ferromagnetic pipes," *Forschungszentrum Karlsruhe Report*, FZKA 6702, 2002

[11] Davidson, P.A., "Magnetohydrodynamics in materials processing," *Ann. Rev. Fluid Mech*., Vol. 31, pg. 273, 1999

[12] Farhat, C., Lesoinne, M., LeTallec, P., "Load and motion transfer algorithms for fluid/structure interaction problems with non-matching discrete interfaces: Momentum and energy conservation, optimal discretization and application to aeroelasticity," *Comput. Methods Appl. Mech. Engrg.*, **157**, pp. 95-114 (1998)

[13] Fautrelle, Y., "Metallurgical applications of MHD," pg. 3, AIAA, 1991

[14] Frank, M., Barleon, L., Müller, U., "Visual analysis of two-dimensional magnetohydrodynamics," *Phys. Fluids*, **13**, pg. 2287-2295, 2001

[15] Ghia, U., K.N. Ghia and C.T. Shin, "High-Re Solutions for Incompressible Flow Using the Navier-Stokes Equations and a Multigrid Method," *J. Comp. Physics* **48** (1982) 387-411

[16] Hunt, J.C.R., "Magnetohydrodynamic flow in rectangular ducts," *J. Fluid Mech*., **21**, part 4, pp. 577-590, 1965

[17] Hunt, J.C.R., "A uniqueness theorem for magnetohydrodynamic duct flows," *Proc. Camb. Phil. Soc.* **65**, pg. 319-327, 1969

[18] Hunt, J.C.R., Holroyd, R.J., "Applications of Laboratory and Theoretical MHD duct flow studies in fusion reactor technology," Culham Laboratory, CLM-R169, May 1977

[19] Jasak, H., "Error analysis and estimation for the finite volume method with applications to fluid flows," Ph.D. Thesis, Imperial College of Science, Technology & Medicine, 1996

[20] Kalis, Kh.E., Tsinober, A.B., Shtern, A.G., Shcherbinin, E.V., "Flow of a conducting fluid past a circular cylinder in a transverse magnetic field," *Magnitnaya Gidrodinamika*, **1**, No. 1, pg. 18-28, 1965

[21] Kenjeres, S., Hanjalic, K., "On the implementation of Lorentz force in turbulence closure models," *Int. J. Heat Fluid Flow*, **21**, pg. 329-337, 2000

[22] Kharicha, A., Molokov, S., Aleksandrova, S., Bühler, L., "Buoyant convection in the HCLL blanket in a strong, uniform magnetic field," *Forschungszentrum Karlsruhe Report*, FZKA 6959, 2004

[23] Kim D., Choi, H., "A second order time-accurate finite volume method for unsteady incompressible flow on hybrid unstructured grids," *J. Comp. Phys.,* **162**, 2000

[24] Kingsley, G., Siegel, J.M., Harrand, V.J., Lawrence, C., Luker, J.L., "Development of a multi-disciplinary computing environment (MDICE)," AIAA Paper 98-4738 (1998)

[25] Kirillov, I.R., Reed, C.B., Barleon, L., Miyazaki, K., "Present understanding of MHD and heat transfer phenomena for liquid metal blankets," *Fus. Eng. Des*., **27,** pg. 553, 1995

[26] Martin, J.C., Moyce, W.J., "An experimental study of the collapse of liquid columns on a rigid horizontal plane," *Phil. Trans. A*., **244**, pg. 312-324, 1952

[27] Messadek, K., Moreau, R., "An experimental investigation of MHD quasi-two-dimensional turbulent shear flows," *J. Fluid Mech*., 456, pg. 137-159, 2002

[28] Molokov, S., Reed, C.B., "Review of free-surface MHD experiments and modeling," ANL report, ANL-TD/TM99-08, April 2000

[29] Moreau, R., "MHD turbulence at the laboratory scale: established ideas and new challenges," *App. Sc. Res.,* **58**, pg. 131-147, 1998

[30] Morley, N.B., Ni, M.-J., Munipalli, R., Huang, P., Abdou, M.A., "MHD simulations of liquid metal flow through a toroidally oriented manifold," to appear in Fusion Eng. Des., 2008

[31] Morley, N.B., Smolentsev, S., Barleon, L., Kirillov, I.R., Takahashi, M., "Liquid Magnetohydrodynamics – recent progress and future directions for fusion," Fus. Eng. Des., Vol. 51, pg. 701, 2000

[32] Morley, N.B., Smolentsev, S., Munipalli, R., Ni, M., Gao, D., Abdou, M.A., "Modeling for liquid metal free surface MHD flow for fusion liquid walls," *Fus. Eng. Des.*, **72**, pp. 3-34, 2004

[33] Morley, N.B., Malang, S., Kirillov, I., "Thermofluid magnetohydrodynamic issues for liquid breeders," *Fusion Sc., Tech*., **47**, No. 3, pg. 488-501, 2005

[34] Murgatroyd, W., "Experiments on MHD channel flows," *Phil. Mag.*, **44**, pg. 1348-1354, 1953

[35] Narula, M., Abdou, M.A., Ying, A., Morley, N.B., Ni, M.-J., Miraghaie, R., Burris, J., "Exploring liquid metal PFC concepts – Liquid metal film flow behavior under fusion relevant magnetic fields," *Fusion Engineering & Design*, 81:(8–14), 1543–1548, 2006

[36] M.-J. Ni, S. Komori, N. Morley, "Projection methods for the calculations of incompressible unsteady flows"*, Numerical Heat Transfer B,* **44**, pp. 533-551, 2003

[37] Ni, M.-J., Munipalli R., Morley N.B., Abdou, M.A., "Validation strategies in interfacial flow computation for fusion applications," *Fusion Engineering & Design*, 81:(8–14), 1535–1541, 2006

[38] Ni, M.-J., Munipalli R., Huang, P.-Y., Morley, N.B., Abdou, M.A., "A current density conservative scheme for incompressible MD flows at a low magnetic Reynolds number (in two parts,)" *J. Comp. Phys.*, Vol. 227, pp. 174-228, 2007

[39] Ni, M.-J., R. Munipalli, N. B. Morley, P.-Y. Huang, M. A. Abdou, "Validation Case Results for 2D and 3D MHD Simulations," *Fusion Sc. and Tech.*, Vol. 52, pp. 587-594, Oct. 2007

[40] Oberkampf, W.L., Trucano, T.G., "Verification and validation in computational fluid dynamics," *Prog. Aero. Sc.*, **38**, pg. 209-272, 2002

[41] Osher, S., Fedkiw, R., "Level set methods and dynamic implicit surfaces," Springer-Verlag, New York, 2003

[42] Potherat, A., Sommeria, J., Moreau, R., "An effective two-dimensional model for MHD flows with transverse magnetic field," *J. Fluid Mech*., **424**, pg. 75-100, 2000

[43] Reed, C.B., Picologlou, B.F., Hua, T.Q., Walker, J.S., "ALEX Results – A comparison of measurements from a round and a rectangular duct with 3-D code predictions," 12th IEEE symposium on Fusion Engineering, Monterey, CA, Oct. 1987

[44] Reiter, F., Tominetti, S., Perujo, A., "Tritium transport in the water cooled Pb-17Li blanket concept of DEMO," *Fus. Eng. Des*., **15**, pg. 223-234, 1992

[45] Roy, C.J., "Review of code and solution verification procedures for computational simulation," *J. Comp. Phys.*, **205**, pg. 131-156, 2005

[46] Samareh, J.A., Bhatia, K.G., "A unified approach to modeling multidisciplinary interactions," AIAA paper 2000-4704 (2000)

[47] Shercliff, J.A., "Steady motion of conducting fluids in pipes under transverse magnetic fields," *Proc. Cambridge Phil. Soc*., **49**, pg. 136, 1953

[48] Smolentsev, S., Abdou M.A., Morley, N., Ying, A., Kunugi, T., "Application of the k-e model to open channel flows," *Int. J. Eng. Sc.*, **40**, pg. 693-711, 2002

[49] Smolentsev, S., Abdou, M.A., Morley, N.B., Sawan, M., Malang, S., Wong, C., "Numerical analysis of MHD flow, heat transfer and tritium transport in a poloidal channel of the DCLL blanket with a SiCf/SiC flow channel insert," to be presented at ISFNT-7, Tokyo, May 22-27, 2005

[50] Smolentsev, S., N. B. Morley, M. Abdou, R. Munipalli and R. Moreau, Current approaches to modeling MHD flows in the dual coolant lead lithium blanket, *Magnetohydrodynamics*, Vol. 42, No. 2/3, 225-236, 2006

[51] Sommeria, J., Moreau, R., "Why, how, and when MHD turbulence becomes two-dimensional," *J. Fluid Mech*., **118**, pg. 507-518, 1982

[52] Sutton, G. W., and A. Sherman, "*Engineering Magnetohydrodynamics*", McGraw-Hill Book Company, New York, 1965

[53] Sze, D.-K., Wang X., "MHD Coating Requirements," presentation made at the JUPITER-II workshop on Modeling and design of materials systems for fusion blankets, Washington, DC., November 2002

[54] Tagawa, T., Authie, G., Moreau, R., "Buoyant flow in long vertical enclosures in the presence of a strong horizontal magnetic field. Part-I: Fully established flow," *European J. Mechanics – B*, **21**, pg. 383-398, 2002 and "Part-II: Finite enclosures," by Authie, G., Tagawa, T., Moreau, R., *ibid* **22**, pg. 203-220, 2003

[55] Tillack, M.S., Wang, X.R., Pulsifer, J., Malang, S., Sze, D.K., Billone, M., Sviatoslavsky, I., "Fusion power core engineering for the ARIES-ST power plant," Fus. Eng. Des., Vol. 65, pg. 215, 2003

[56] Townsend, J.C., Salas, A.O., "Managing MDO software development projects," AIAA paper 2002-5442 (2002)

[57] Thess, A., Zikanov, O., "Why, how, and when two-dimensional MHD turbulence becomes three-dimensional," article in review, 2005

[58] Tsinober, A., "MHD flow drag reduction," in Viscous Drag Reduction in Boundary layers, *AIAA Progress in Aero. and Astro.,* Vol. 123, ed. Bushnell D.M., Hefner, J.N., 1990

[59] J. Van Kan, "A second order accurate pressure-correction scheme for viscous incompressible flow," *SIAM Journal of Scientific Computing*, **7**, pp. 870-891, 1986

[60] Walker, J.S., Ludford, G.S.S., "Entry lengths for circular and rectangular ducts in strong magnetic fields," *Magnitnaya Gidrodinamika*, **11**, No. 1, pp. 75-78, 1975

[61] D. G. Whyte, T. E. Evans, C. P.C. Wong, W. P. West, R. Bastasz, J. P. Allain, J. Brooks, "Experimental observations of lithium as a plasma-facing surface in the DIII-D tokamak divertor," *Fusion Engineering and Design*, 2003

[62] Widlund, O., "Wall functions for numerical modeling of laminar MHD flows," *European J. Mechanics – B*, **22**, pg. 221-237, 2003

[63] Ying, A.Y., et al, "Exploratory Studies of Flowing Liquid Metal Divertor Options for Fusion Relevant Magnetic Fields in the MTOR Facility," To appear in Fusion Engineering and Design, 2004

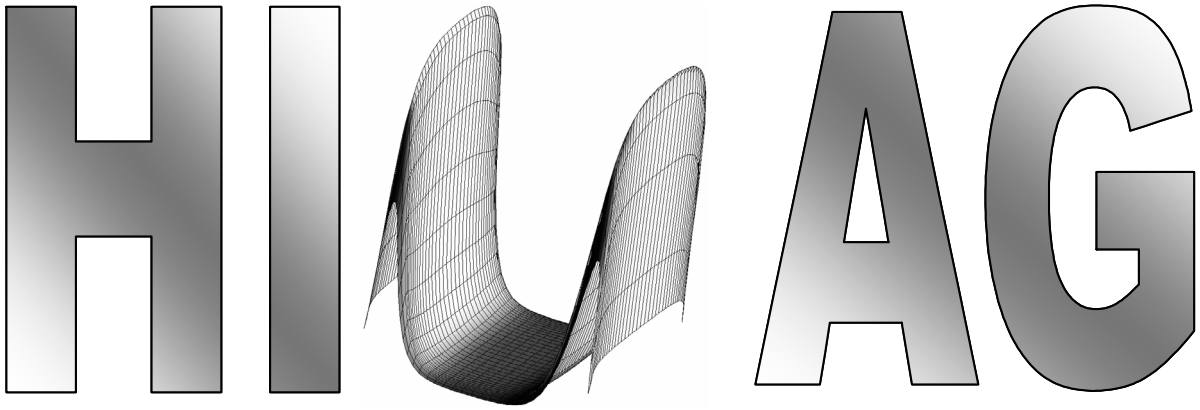

**H**yPerComp **I**ncompressible **M**HD solver for **A**rbitrary **G**eometry



# A Guide to the Graphical User Interfaces

**Table of Contents**

## 1. A Guide to the Graphical User Interfaces

This document is an introduction to the graphical utilities interfacing with HIMAG. In summary, the sequence of steps in executing HIMAG in its present form are:

1. Create a grid using HIMAG-GRID. This involves the following steps:
   Run HIMAG-GRID and obtain a univ.cemgrd file
   Run UNIVBK and obtain a fort.21 file
   Move fort.21 to ***<casename>.ux*** file
   The .ux file is the grid that HIMAG uses. It can also be generated via commercial mesh generation software such as ICEM-CFD. Should material regions be involved, a mat.bin file is additionally created. mat.bin can be created within HIMAG as well, if the uses wishes to specify material regions within HIMAG.
2. Create a BC patch file using HIMAG-PREP. This involves the following steps:
   Run HIMAG-PREP, create individual patches from geometrical or other techniques
   Read in material regions from mat.bin
   Create material interface patch regions for post-processing if needed
   Save the BC file as ***<casename>.ugm***
3. Partition the ux and ugm files if parallel execution is desired. This will result in a series of files named partition.?.patch partition.?.ux partition.?.ugm. The utilities ux2part and colormhd are used to partition the grid and BC file.
4. Create or modify the HIMAG input file
5. Execute HIMAG. Typically the run command is:
   Single CPU: ./himag –i mhd –g duct
   16 CPUs: mpirun –np 16 ./himag –i mhd
   CPU list from file: mpirun –p4pg pgfile ./himag –i mhd
   where mhd.input is the input file, duct.ux and duct.ugm are the grid and BC files, and pgfile is a CPU list on which the code can be run when run in parallel.
6. The code writes diagnostic information to screen which can be redirected to an output file.
7. MHD2TEC can be then used to postprocess results for visualization in TECPLOT.

# HIMAG-GRID

A simple mesh generation program for HIMAG for routine geometries

## HIMAG-GRID

With the intent of making HIMAG a user-friendly tool for researchers in the liquid-metal MHD community, HyPerComp Inc. has developed a grid generation capability with many useful features. Grid generation can be accomplished by a text-based input file or by the use of a GUI. In this section we will describe the salient features of the grid generation tool and also the GUI developed for problem set-up.

Grid generation for liquid-metal MHD: Square and circular ducts are among the most common configurations of interest to the fusion community. While the ultimate goal of HIMAG is to provide a detailed solution of liquid metal flows in complex manifolds, fully developed and/or developing flows in simple ducts can provide useful insight into the physics of such flows. Grid generation for flows in simple geometries is greatly simplified by the use of a tool developed by HyPerComp. This utility reads in a text input file prepared by the user (or generated by a GUI) and generates a single block to which the user can assign boundary conditions.

For problems involving the flow of liquid metals in a magnetic field, the cross-sectional area of a duct (with infinitesimally thin walls) can be divided into 3 main regions. These regions are, the Hartmann layer (near walls perpendicular to the direction of the B-field), the side layer (parallel to the direction of the field) and the core. The thickness of the Hartmann layers are proportional to the reciprocal of the Hartmann number, whereas the thickness of the side layers are proportional to the reciprocal of the square root of the Hartmann number. For high Hartmann number cases of interest to the fusion community, resolving the Hartmann layer can lead to a great disparity in the grid spacing in the core region, Hartmann layers, and the side layers. Keeping this constraint in mind, good quality grids need to be generated by ensuring a smooth transition of grid spacing from one region to another. To facilitate the generation of good quality grids for use with our solver, we have developed an in-house grid generation utility.

The main features of this tool are as follows:

Importing existing grid files: This option facilitates the use of existing 1-D and 2-D grid spacing information. For instance, if one were to be given the distribution of grid points along the Y and Z axes, it is possible to generate the grid connectivity information. This feature is useful for code validation purposes. Using this feature, it is possible to regenerate the exact grid used by any other solver/group and verify the validity of the results using HIMAG.

Grid type: The user can generate a grid with the following cell types. The value to be assigned to the option variable (nopt) is shown alongside the grid type.

(a) Hexahedral (nopt = 1)
(b) Prism (nopt = 2)
(c) Tetrahedral (nopt = 3)
(d) Hexahedral grid for a circular geometry (nopt = 40)
(e) Hexahedral grid for a half circular geometry (nopt = 41)
(f) Polar grid for a circular geometry (nopt = 50)

Some sample grids generated using some of the above-mentioned options are show below. Fig 104 (a) shows a prism grid (nopt = 2), whereas Fig 104 (b) and (c) show a hexahedral grid for a half circular geometry (nopt = 41) and a polar grid (nopt = 50), respectively.

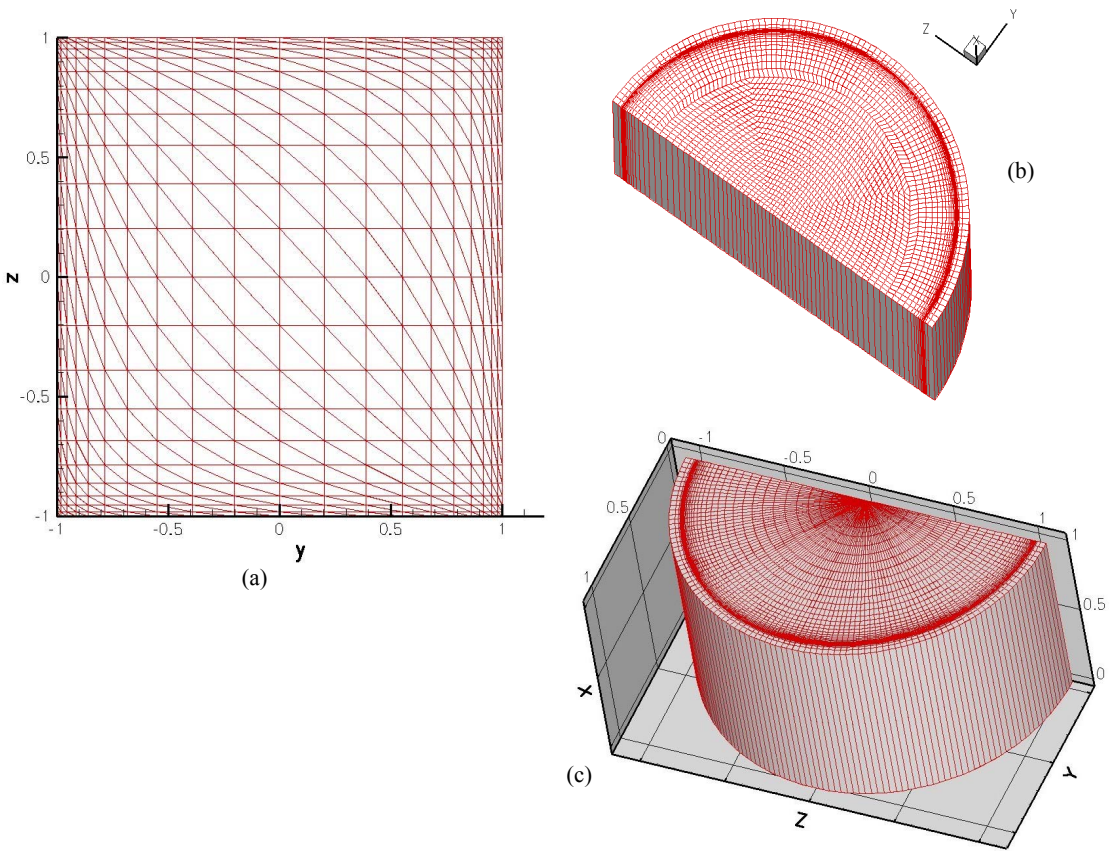


Figure 104: Sample meshes generated by HIMAG-GRID

Grid stretching: Five options are available for generating uniform and non-uniform stretching. These options are as follows. The value to be assigned to the variable (iopt) is shown along side.

(a) Uniform mesh (iopt = 0)
(b) Roberts' stretching (Left and Right) (iopt = 1 & 2, respectively)
(c) Roberts' double sided stretching (iopt = 3)
(d) Polynomial stretch (prescribed grid spacing at either end). (iopt = 4)
(e) Interior stretch at a prescribe location (iopt = 5)

When a non-uniform stretching option is chosen (iopt > 0) the user has to provide the stretching parameter. Using these stretching options the user has the ability to divide the computational domain into several segments and use the appropriate stretching option to generate good quality grids.

Symmetries: If the grid is symmetric in a particular co-ordinate direction, this feature can be used to mirror the grid spacing about the axis of symmetry. '0' implies no symmetry, whereas 1 implies symmetry. With this notation, an input such as 011 implies that there is no symmetry in the X-direction whereas there is symmetry in the Y and Z directions. This feature is useful in situations where the domain comprises of many materials and regions such as the DCLL unit-cell problem.

Figure 105 shows the cross-section of the DCLL unit-cell. The DCLL comprises of an outer stainless-steel wall, and a Silicon Carbide (SiC) flow-channel insert surrounding the flow of Lithium-Lead (fluid).

A slot in the FCI in the direction of the magnetic field allows the Lithium-Lead core to communicate with a thin region of Lithium-Lead flowing in the region between the outer stainless steel sleeve and the FCI (this slot is called the Pressure Equalizing Slot (PEH)). The DCLL geometry presents a challenging configuration in terms of generating a good quality grid. The PEH and the Hartmann layers have to be resolved along with the FCI, the stainless steel outer wall, and the core flow. By exploiting the symmetry feature along the Y and Z direction, and the use of appropriate stretching parameters, one can generate a grid to study a fully-developed flow in this cell. The input file for this geometry is also shown in the Appendix. Since the grid is symmetric in the Y and Z axes, only 6 segments are specified in the input file. Using the symmetry option (011) the remaining segments are generated automatically. Figure 106 shows the grid layout of the DCLL generated using the grid generation tool developed at HyPerComp Inc.

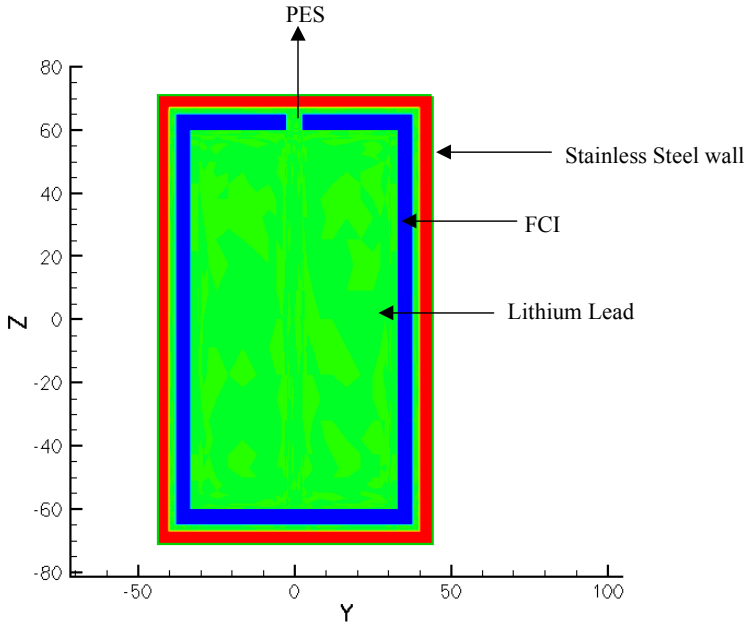


Figure 105: Geometrical configuration of the DCLL unit cell

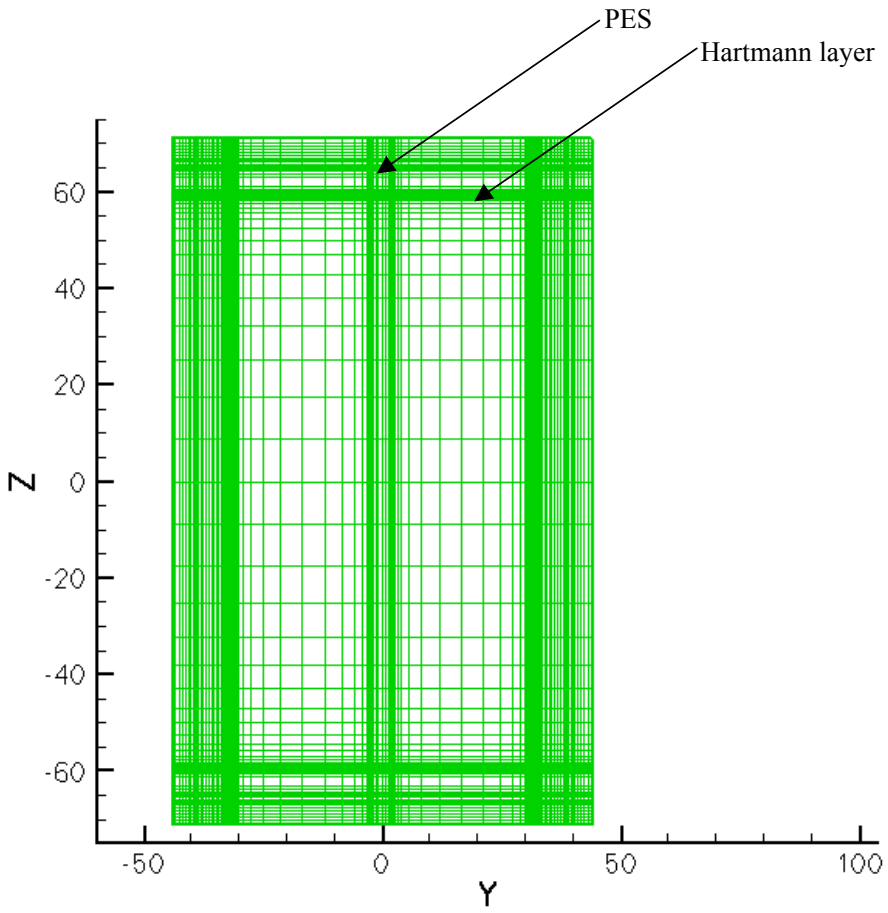


Figure 106: Grid layout of the DCLL unit cell

Non-orthogonal meshes in Square/Rectangular geometries: This feature is very useful in testing and benchmarking non-orthogonal corrections in the solver. For instance, one could generate a orthogonal, hexahedral mesh in a square duct and compute the flow field, electric potential and current under the fully developed flow assumptions (Shercliff solution or Hunt solution). The user could then generate a non-orthogonal mesh and recompute the solution with the non-orthogonal corrections. Fig 107 shows some non-orthogonal meshes generated by this feature. The user can define the degree of non-orthogonality by prescribing the two parameters (mgrd1 and mgrd2) which fixes the number of grid points orthogonal grid points in the each coordinate direction.

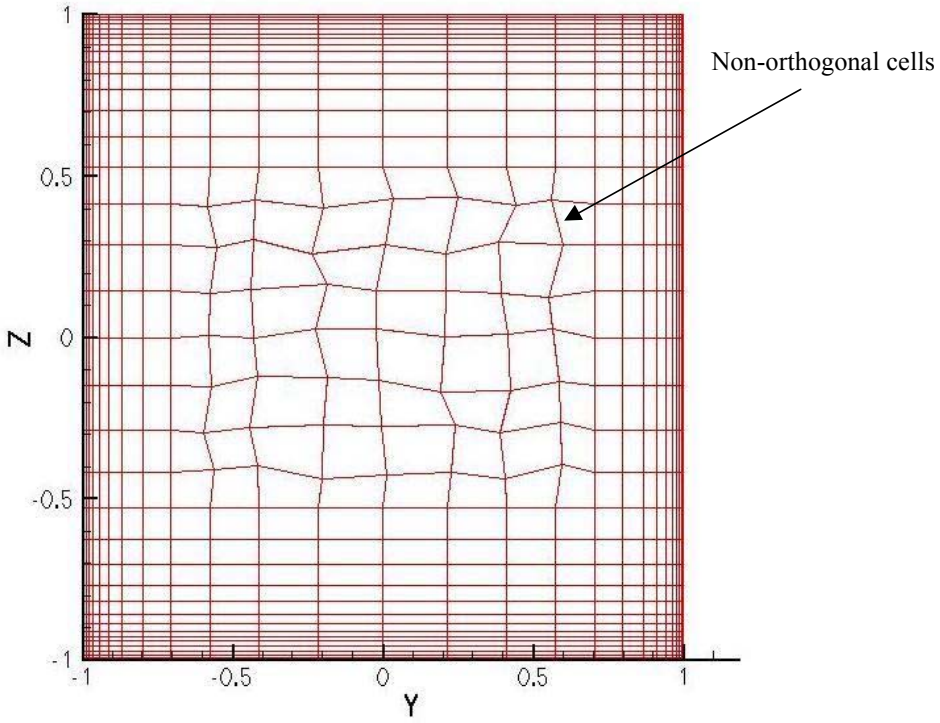

Figure 107: Non-orthogonal cells in a square domain.

Diagnostics: The grid generation tool also writes out a log file (grid.log) that identifies the grid type used by the user, the extent of the computational domain in the 3 coordinate axes and the minimum cell size in each of the coordinate axes. Additionally, it also provides information about the number of cells and nodes.

In order to generate a good quality grid it is necessary to ensure a smooth transition in the grid spacing between adjacent segments along any coordinate direction. A trial and error method is necessary to select the stretching parameters in various segments to accomplish this goal. In order to simplify this process, the grid generation tool writes out a file called checkXYZ.dat. This file has the location and grid-spacing for each grid point along each coordinate axis. The user can look at the grid spacing between various segments and make an intelligent guess as to the value of the stretching parameter to be used. This greatly facilitating the process of generating grids for geometrical configurations, requiring multiple segments (such as the DCLL unit cell geometry).

An example of the use of this grid generation utility is for the study of a fully developed flow in a square duct is demonstrated. A sample input grid file for the case is shown on pages 107-108. For this particular case, it is assumed that the magnetic field is applied along the Y-axis and the fully developed flow is in the X-axis The half width for this duct is 1 m and the center of the duct is at the origin. The user specifies the extent of the domain and the number of regions (nxsgm, nysgm, nzsgm) for each of the coordinate directions (X, Y & Z). For each region, the user further specifies the number of grid points and the extent of the region. In the sample input file, the Y and Z coordinate axis have 3 regions (two for the near wall Hartmann/sidewalls and one for the core). The appropriate stretching function with the stretching factor is used to ensure a smooth transition from the highly refined Hartmann/sidewall region to the core of the flow. In the core of the flow, gradients of velocity, electric potential and other variables are small, hence a coarse mesh is sufficient. Fig 108 shows the entire grid and an enlarged view of the grid spacing near the Hartmann and side walls.

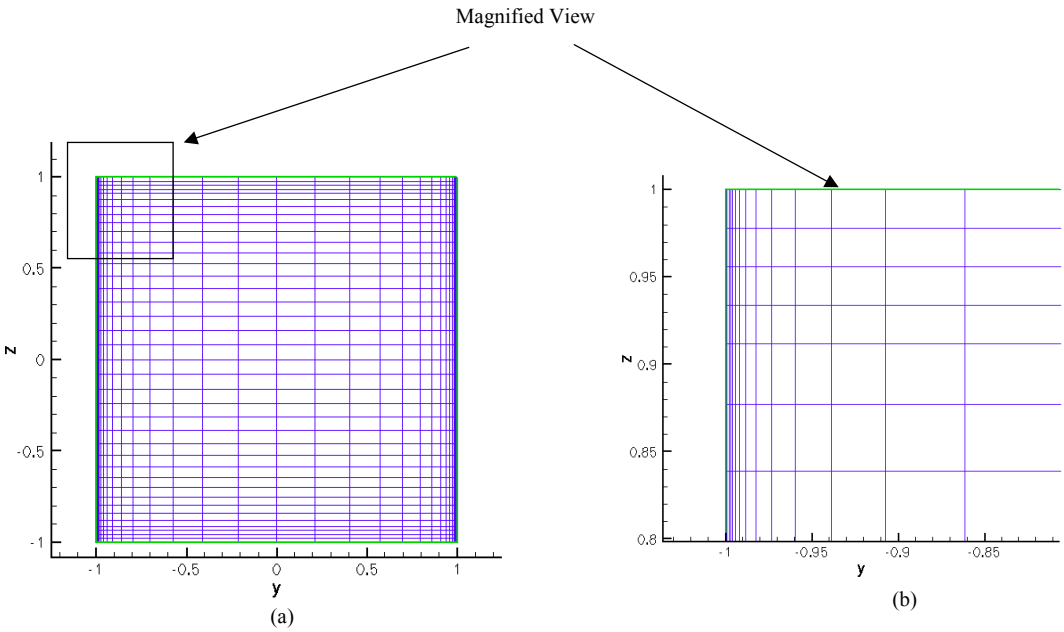


Figure 108: Grid layout (a) and magnified view of the Hartmann layer (b) for a square duct using the input file shown in Appendix 1

Grid generation for Circular ducts: Thus far we have discussed the utility of the grid generation tool for generating hexahedral, orthogonal meshes for rectangular geometrical configurations. As mentioned earlier, our grid generation utility also has the ability to generate grids for circular pipes. Several types of grids with varying degrees of non-orthogonality can be generated. Figure 109 shows different kinds of grids that can be generated for circular pipes. Figure 109 (a) shows a grid with an orthogonal core whereas regions near the outer periphery have highly non-orthogonal cells. Figure 109 (b) shows another grid generated with cells which are not as non-orthogonal using our grid generation tool.

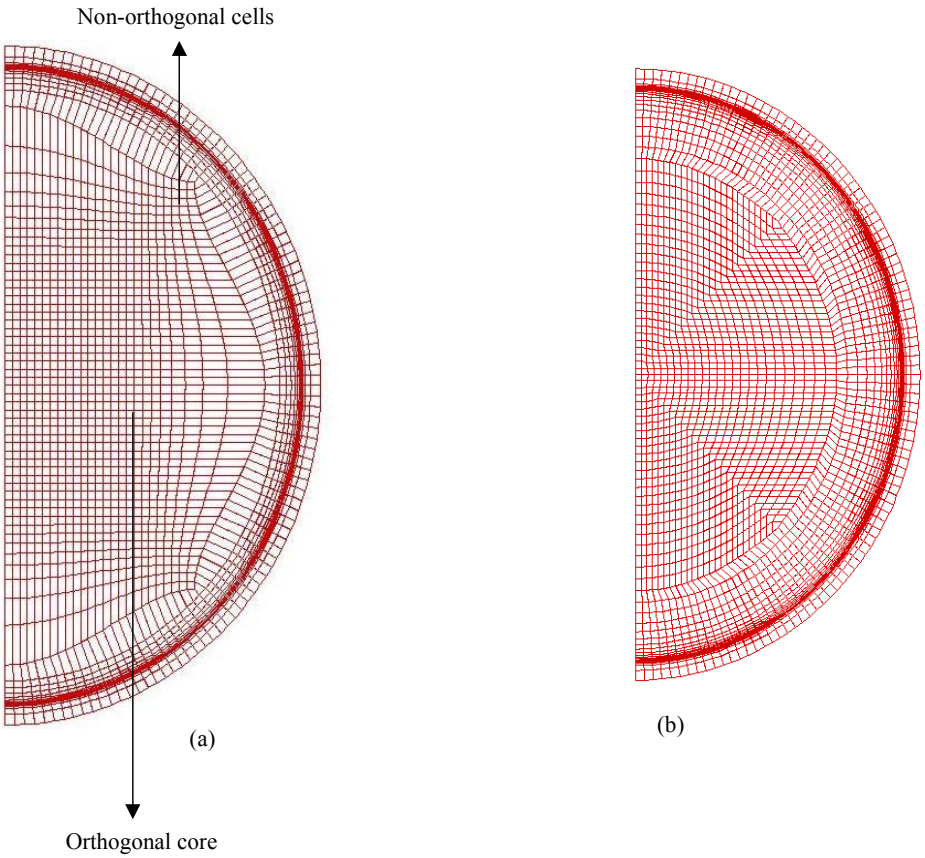

Figure 109: Grids generated for a circular duct with conducting walls with HIMAG-GRID

## GUI-Based Grid generation:

To enhance the utility of our grid generation tool, we have also developed a GUI to facilitate the generation of the input file. The sample input files shown in (pg. 107-108) can be generated using this GUI. The GUI enables the user to define the number of segments, the number of grid points per segment and the stretching parameter. The GUI interface also writes out a text input file to enable future verification.

### Chose Geometry Type:

Grid Creation Main Window. Creating a 3D rectangle.

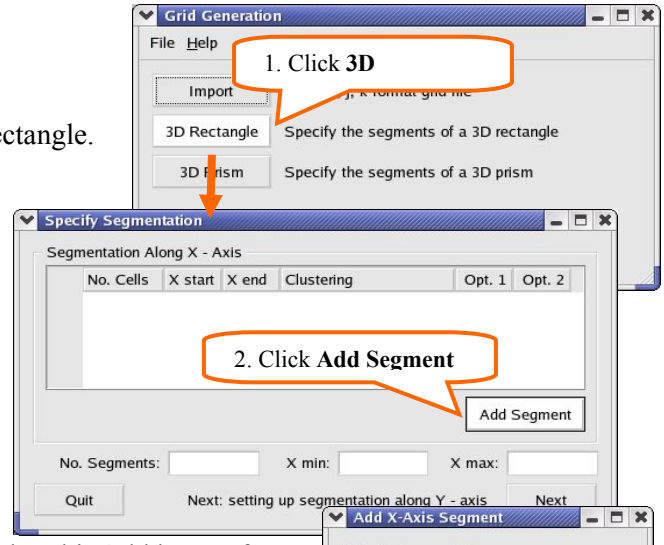


### Add Segments:

Adding Segments. Using the Add Segment Dialog, hit Add button for each segment.
Entries are added to the table.

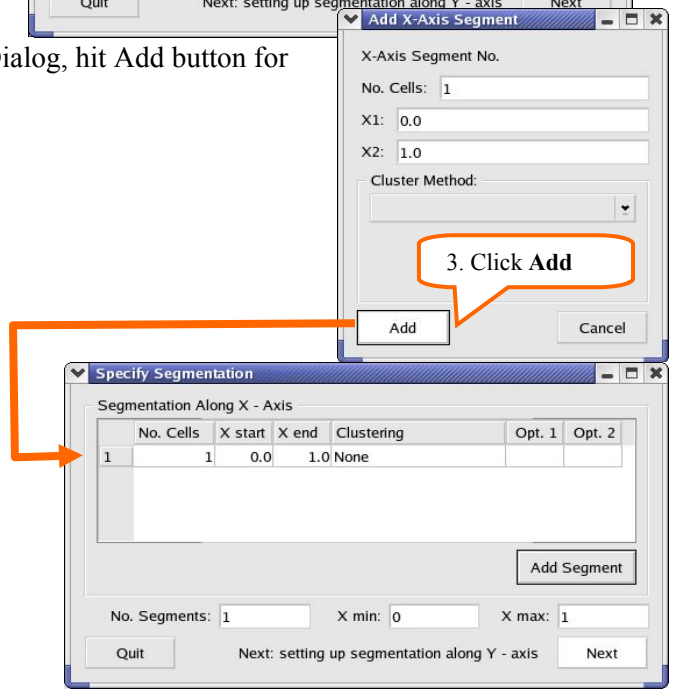


### Repeat for Y and Z Axes:

Hit the Next button to progress to the proceed to next axis

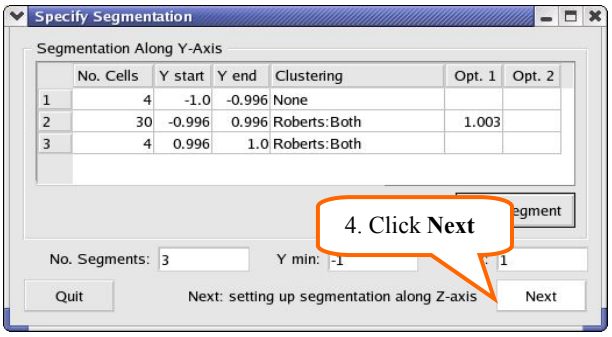

**Save Input File:**

Save the input (.input) file for future geometry modifications.

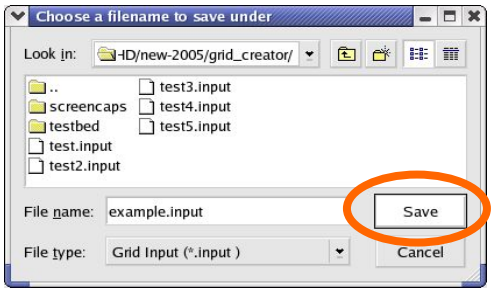


**Save Geometry File:**

Save the geometry (.ux) file.

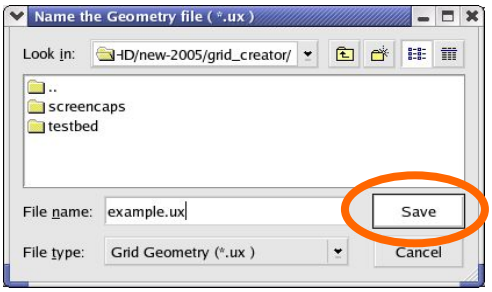

## INPUT FILE FOR THE SQUARE DUCT

```
* x-axis: Number of segments (nxsgm),  xmin,   xmax
                            1     0.0      1.0
* #1: nxcel,  xmax1
      1     1.0
      Stretch_option, stretching_factor
      0
* y-axis: Number of segments (nysgm),  ymin,   ymax
                           3   -1.0      1.0
* #1: nycel, ymax1
      4     -0.996
*     Stretch_option, stretching_factors
      0
* #2: nycel, ymax2
      30    0.996
*     Stretch_option, stretching_factor
      3
      1.003
* #3: nycel, ymax3
      4     1.0
*     Stretch_option, stretching_factor
      0
* z-axis: Number of segments (nzsgm),  zmin,   zmax
                         3       -1.0      1.0
* #1: nzcel, zmax1
      4     -0.912
*     Stretch_option, stretching_factor
      0
* #2: nzcel, zmax2
      30    0.912
*     Stretch_option, stretching_factor
      3
      1.3
* #3: nzcel, zmax3
      4     1.0
*     Stretch_option, stretching_factor
      0
```

## INPUT FILE FOR THE DCLL UNIT CELL

```
* x-axis: Number of segments (nxsgm),  xmin,   xmax
                                    1     0.0   1.0
* #1: nxcel, segment-xmax
      1     1.0
*     Stretch_option, stretching_factor
      0
* y-axis: Number of segments (nysgm),  ymin,   ymax
                                  11    -44.0 44.0
* #1: nycel, segment-ymax
      6     -40.0
*     Stretch_option, stretching_factor
      2
      1.5
* #2: nycel, segment-ymax
        5       -38.0
```

```
*     Stretch_option, stretching_factor
        1
      2.9
* #3: nycel, segment-ymax
        10      -33.0
*     Stretch_option, stretching_factor
        0
* #4: nycel, segment-ymax
        14      -24.78
*     Stretch_option, stretching_factor
        0
* #5: nycel, segment-ymax
        14      -2.5
*     Stretch_option, stretching_factor
        3
        1.09
* #6: nycel, segment-ymax
        10      2.5
*     Stretch_option, stretching_factor
        3
      2.85
* z-axis: Number of segments (nzsgm),  zmin,   zmax
                              11          -71   71
* #1: nzcel, segment-zmax
        6       -67.0
*     Stretch_option, stretching_factor
        2
      2.0
* #2: nzcel, segment-zmax
        5      -65.0
*     Stretch_option, stretching_factor
        0
* #3: nzcel, segment-zmax
        4       -63.0
*     Stretch_option, stretching_factor
        1
      1.3
* #4: nzcel, segment-zmax
        6       -60.0
*     Stretch_option, stretching_factor
        2
      1.009
* #5: nzcel, segment-zmax
        5      -59.875
*     Stretch_option, stretching_factor
        0
* #6: nzcel, segment-zmax
        60      59.875
*     Stretch_option, stretching_factor
        3
      1.0025
```

# HIMAG-PREP

# A Graphical pre-processor for HIMAG

## HIMAG-prep Tutorial-One: cube.ux

This tutorial is intended to guide a novice HIMAG-prep user through a typical session. During the tutorial, the user will open a .ux (geometry) file, create a patch on the geometry from a cutting plan, create a patch from free faces, assign boundary conditions to both patches, and save the project by writing a .ugm (unstructured grid MHD) file.

USER TIP: The name of the .ugm file will usually, but not always be the same as that of it's corresponding geometry, or .ux, file. Normally, when a geometry file is loaded, HIMAG-prep will automatically look for a .ugm file with same name so that the properties of the geometry load at the same time. However, because the boundary conditions and materials properties of a particular geometry can be swapped out for other boundary conditions and material properties (created for that same geometry), multiple, uniquely named .ugm files may exist. This topic will be addressed again later in the tutorial.

NOTE: The HIMAG-prep dialogs and windows in this tutorial have had their borders removed; the appearance of your dialogs and windows will of course depend on the version and operation system you are using.

1. After successfully compiling and installing HIMAG-prep, and after setting the PATH variable to allow for calls to the program, go to the tutorial directory.
2. From the command line run the program by typing "prep":
    a. Host:> prep
3. A dialog will appear asking for a geometry file to load.
4. Select "cube.ux" and hit "open."

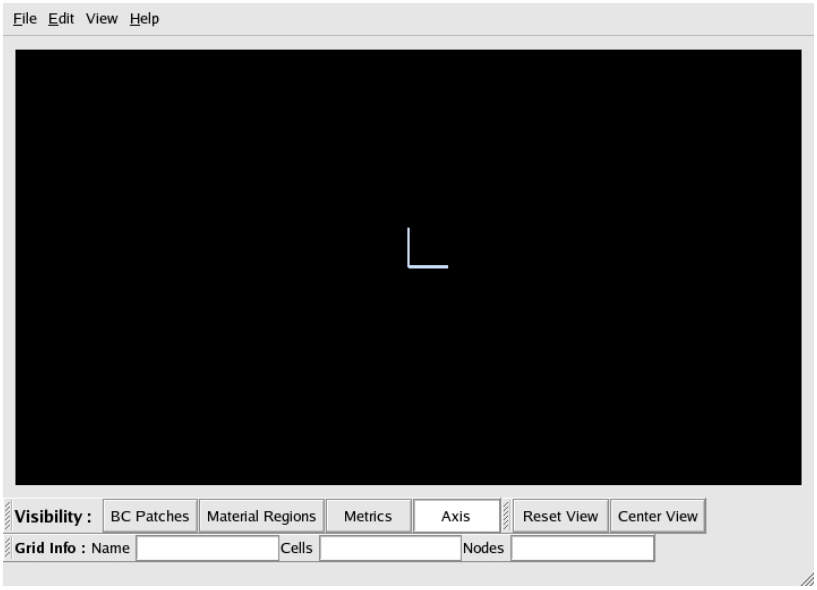


5. The Prep main window looks empty at first: The geometry is actually a cube shape, but only the white markers for the x,y,and z axis can be seen. While the geometry has loaded, no patches have been defined, so nothing is visible yet. In the tutorial directory, you'll notice no "cube.ugm" exists yet. No patch related information exists for this geometry yet. That will change as the tutorial is completed.

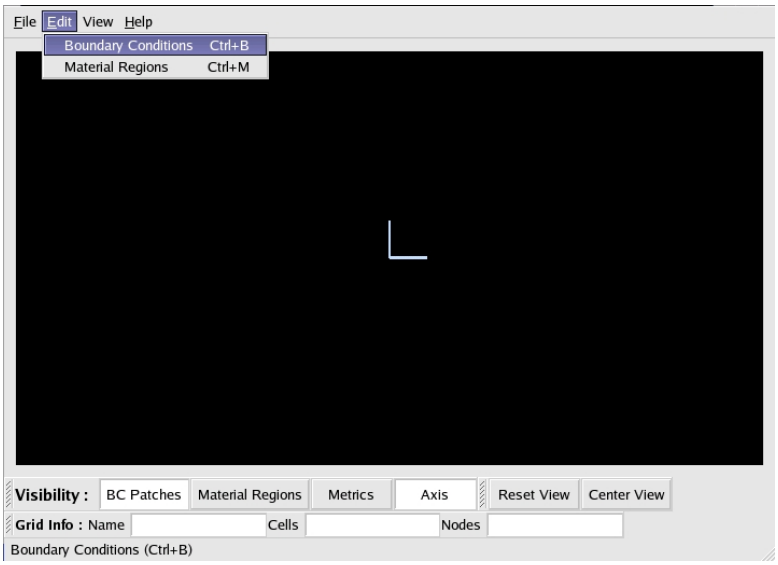


6. From the top menu bar, select "Edit." A popup menu will appear. Select "Boundary Conditions."
7. The Boundary Conditions Panel will appear:
8. This Panel has many functions. It allows the user to create and edit patches derived from the current geometry. Once patches are created, the panel describes the boundary conditions of all the patches in the geometry. Notice at the top of the panel a menu bar with "Create" and "Edit" as its options. The "Create" menu is where patches can be derived from the geometry either by a node range, a cutting plan, a min/max box, or from the remaining faces not

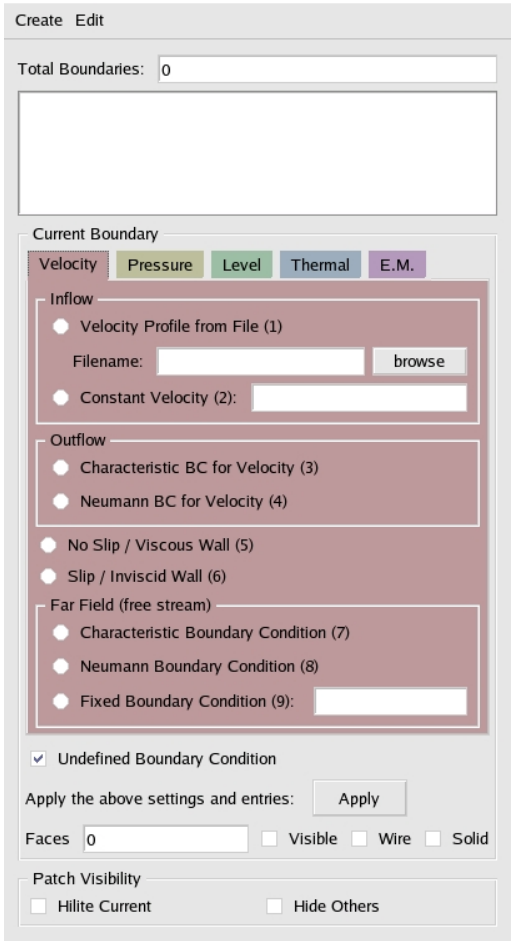

included in any patch ("free faces"). The "Edit" menu is where patches can be duplicated and deleted.

9. In this example a patch will be created from a cutting plane. The z=1 plane of the cube shape.
10. Select "Create" from the top menu bar.
11. Select "From Cutting Plane" from the popup menu.

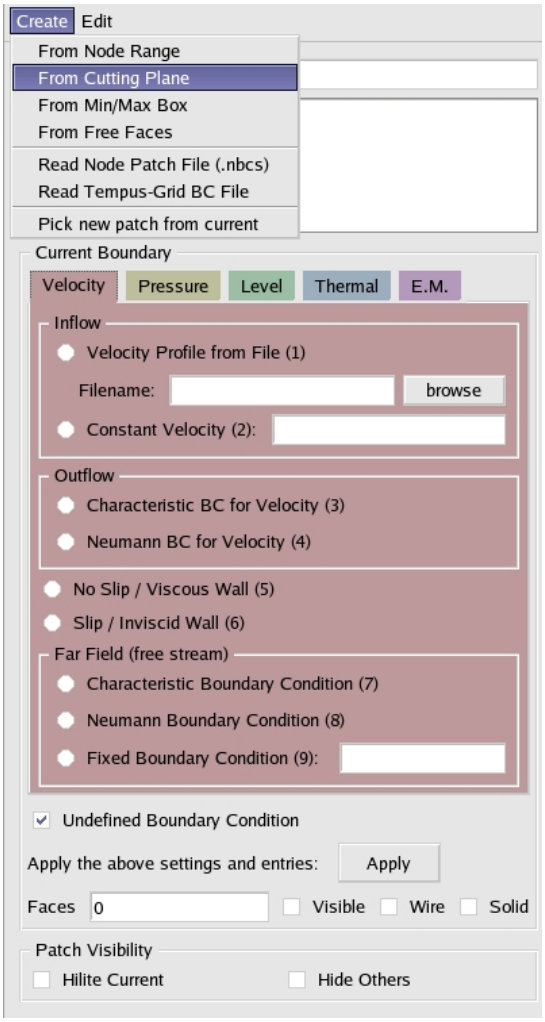


12. A popup window will appear asking you along which plane you would like to create the patch. Select "Z."

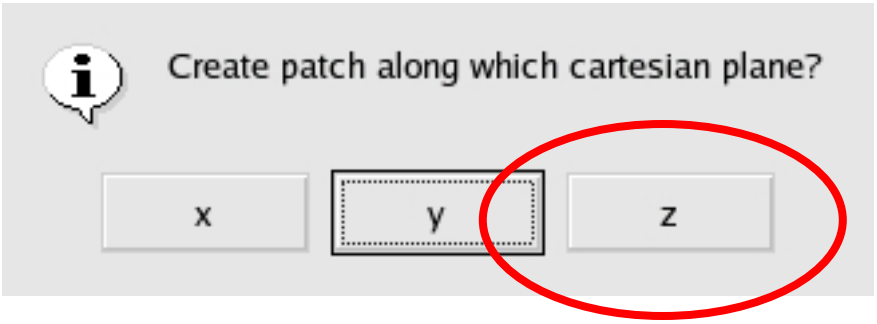

13. Another popup window will appear asking you for the plane value. Eneter 1.0 and click "OK."

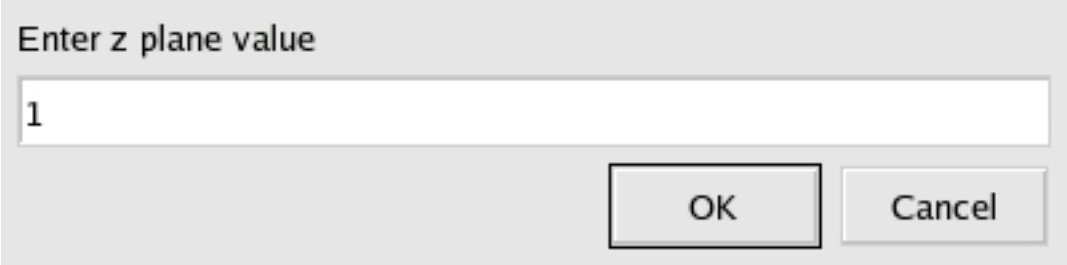


14. Another popup window will appear asking you for the tolerance. Enter 0.001 and click "OK."

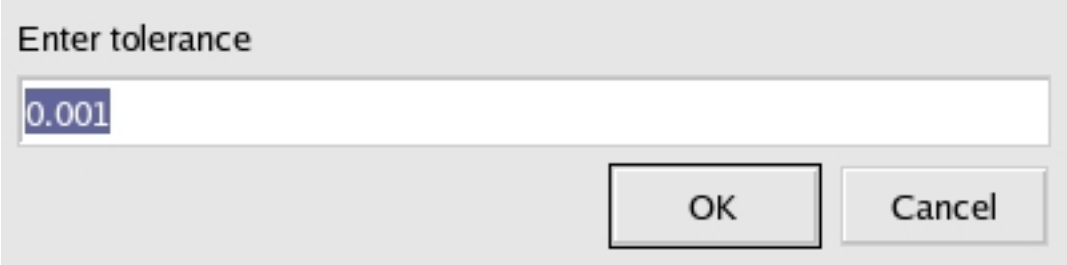


15. A patch made up of the faces of the cube geometry existing on the z=1 plane will appear in the main window:

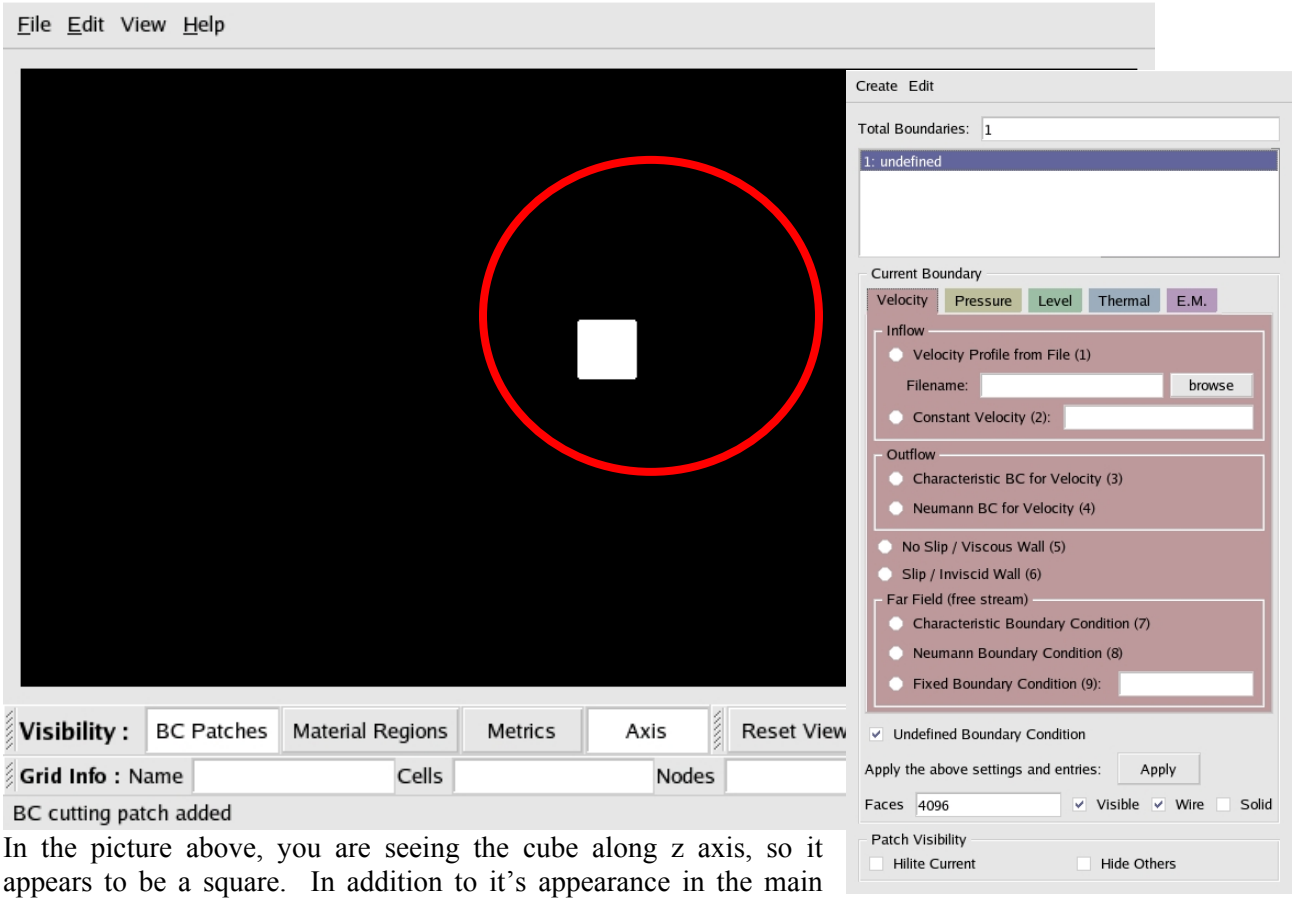


In the picture above, you are seeing the cube along z axis, so it appears to be a square. In addition to it's appearance in the main window, the new patch will appear as "undefined" in the list box at the top of the Boundary Condition panel.

16. The Boundary Condition panel has been shown above, adjacent to the viewer window.

17. DEFINING BOUNDARY CONDITIONS / ASSIGNING BC's TO PATCHES: Next the user will want to define a boundary for that patch. Notice the "Current Boundary" titled group of five colored tabs in the center of the panel. The five aspects of a boundary condition in HIMAG-prep are: Velocity, Pressure, Level Set, Thermal, and Electro Magnetics. Selecting a type from each of the five aspect tabs defines the boundary condition. The types are radio buttons; only one type per Tab can be chosen at a time.

**USER TIP:** You must make a selection from each of the five aspect tabs and then click the "Apply" button underneath the tabs to define a boundary condition. Leaving any one of the tabs unselected means the definition of the patch's boundary condition is incomplete and will result in the "Apply" command being ignored. In the case of an incomplete assignment the "Apply" button leaves the patch unchanged.

18. Select the "Velocity" tab; and then select the "Constant Velocity" button within it. In the constant velocity editable field, enter a value of 1.0.
19. The panel should look like this:
20. Select the "Pressure" tab; and then select the "Neumann" button within it.

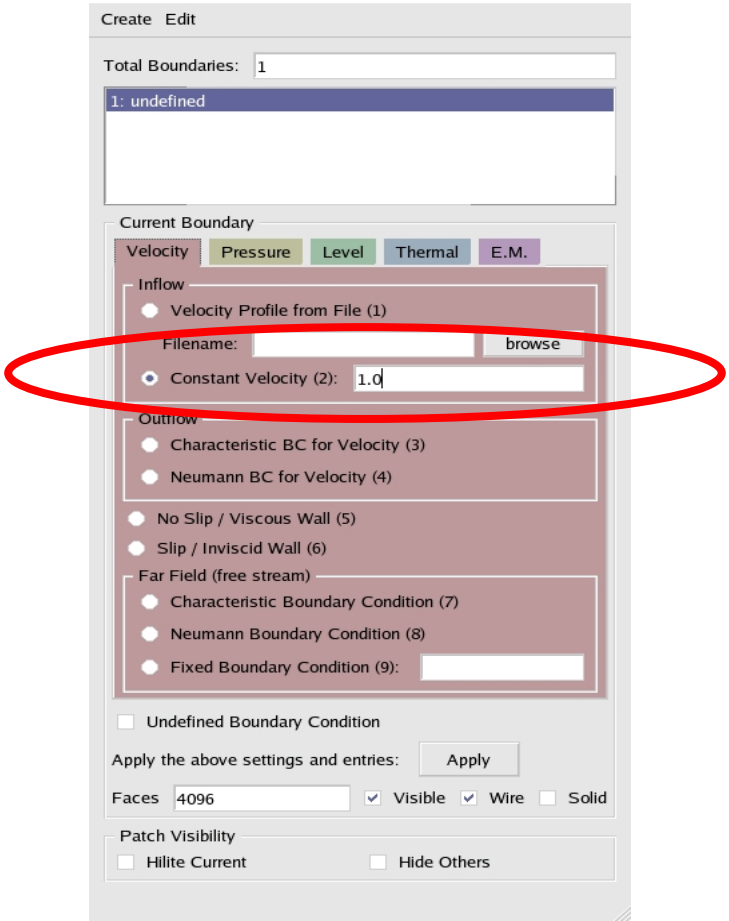


21. Select the "Level" tab; and then select the "Neumann" button within it.
22. Select the "Thermal" tab; and then select the "Neumann" button within it.
23. Select the "E.M." tab; and then select the "Neumann Phi" button within it.
24. The panel should now look like this:

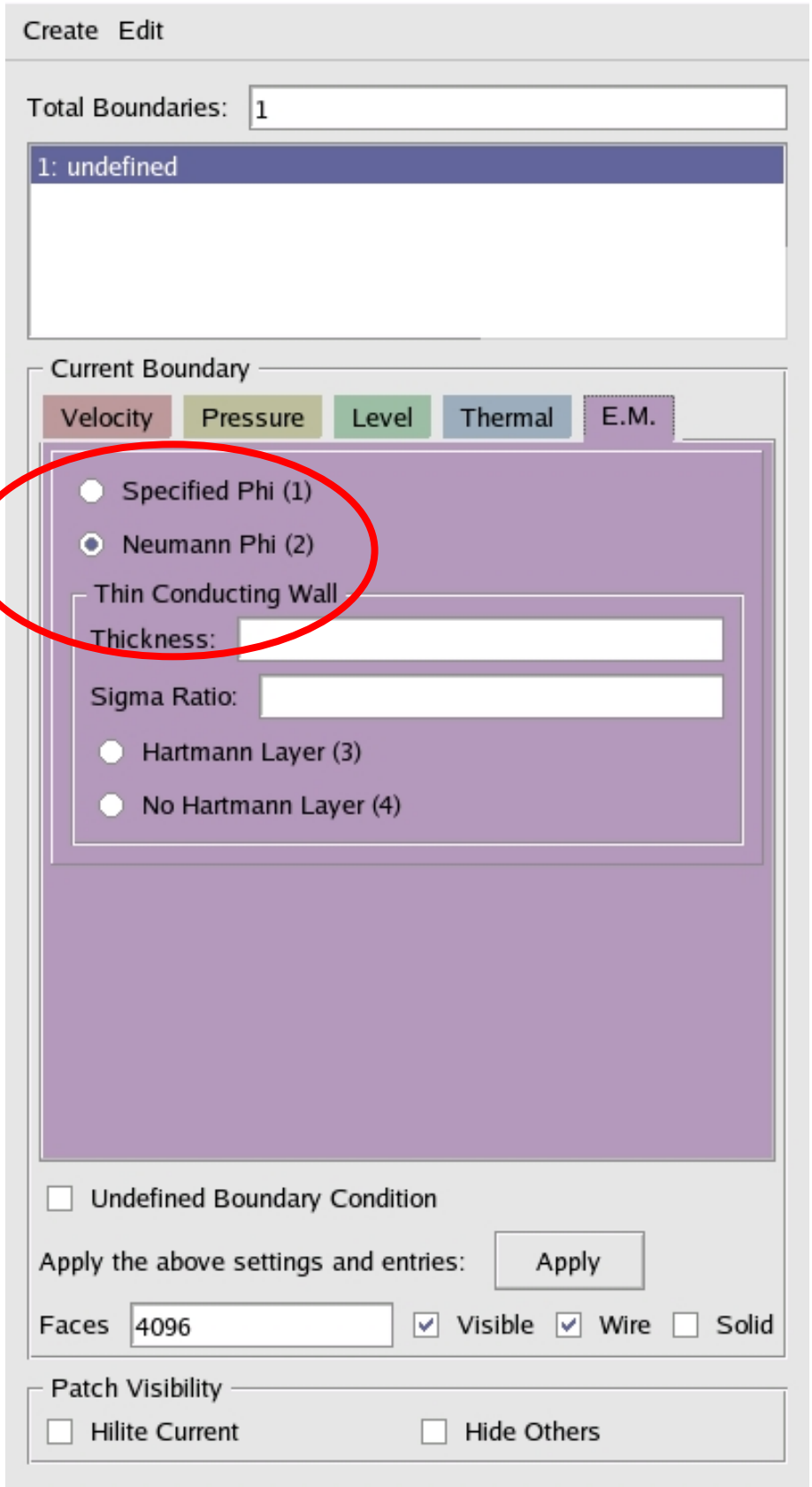
Create Edit
Total Boundaries: 1
1: undefined
Current Boundary
Velocity Pressure Level Thermal E.M.
Specified Phi (1)
Neumann Phi (2)
Thin Conducting Wall
Thickness:
Sigma Ratio:
Hartmann Layer (3)
No Hartmann Layer (4)
Undefined Boundary Condition
Apply the above settings and entries: Apply
Faces 4096 Visible Wire Solid
Patch Visibility
Hilite Current Hide Others

25. With all five aspects defined; click the “Apply” button to set this boundary condition to the current patch.

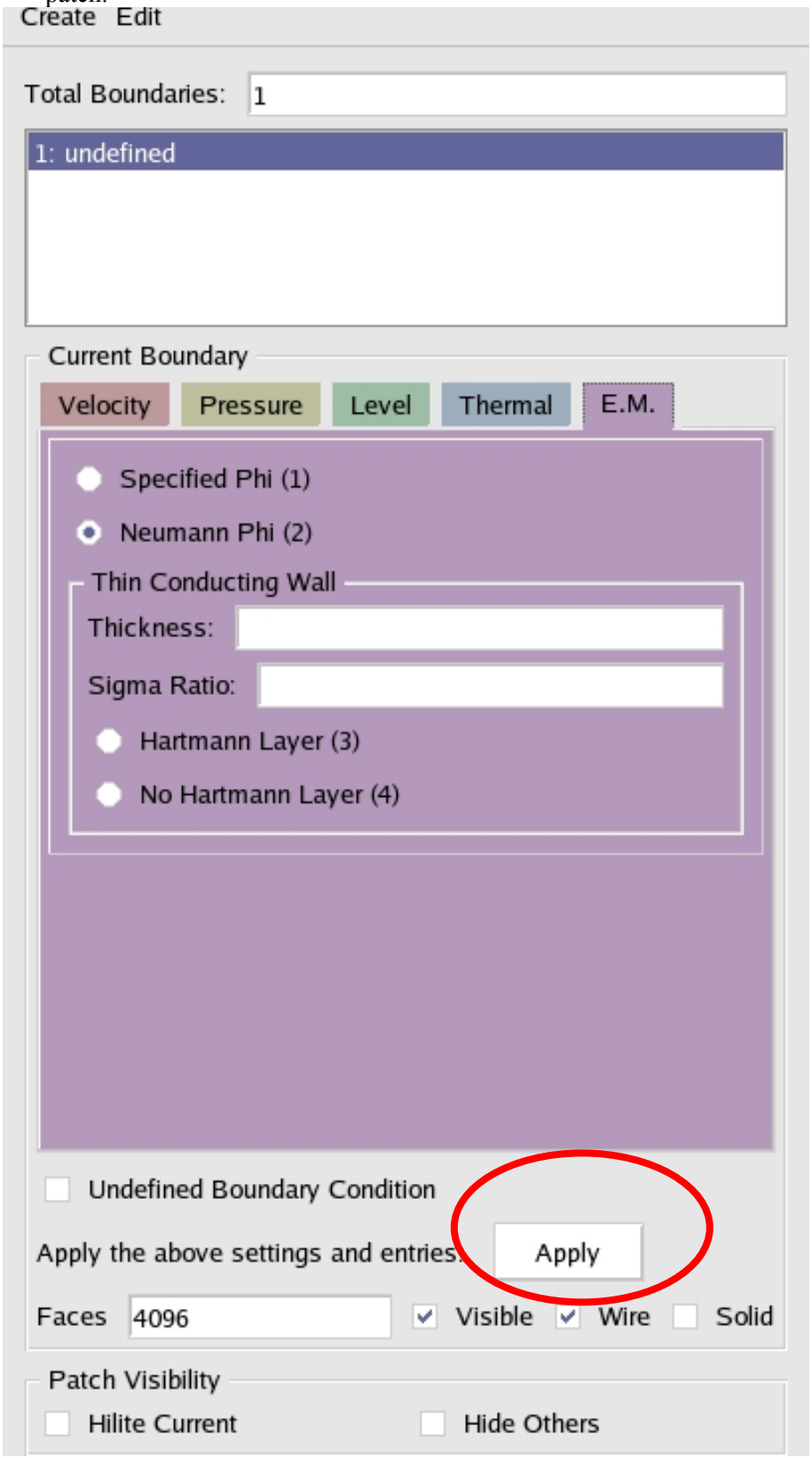

26. The panel will update, showing the z=1 plane patch to be 2:2:2:2:2. These numbers indicate the combination of aspects from the five tabs. Within each tab the options are numbered 1, 2,…,n in parenthesis next to that option. The numbers in list box entry are in the same order from left to right as the five aspect tabs. This makes 2:2:2:2:2 shorthand for Constant Velocity, Neumann, Neumann, Neumann, and Neumann Phi.
27. Notice the "Undefined Boundary Condition" checkbox. This checkbox is automatically unchecked as a boundary is being defined by the user. Conversely, the user can check the box and hit "Apply" to make patch undefined.
28. Next the user will create a patch from all the faces that aren't already part of an existing patch. These are called "free faces."
29. Select "Create From Free Faces" from the Boundary Condition panel's "Create" menu. This creates a new patch made up of the free faces in the current geometry.
30. Selecting "From Free Faces:"


31. The panel should now look like this:

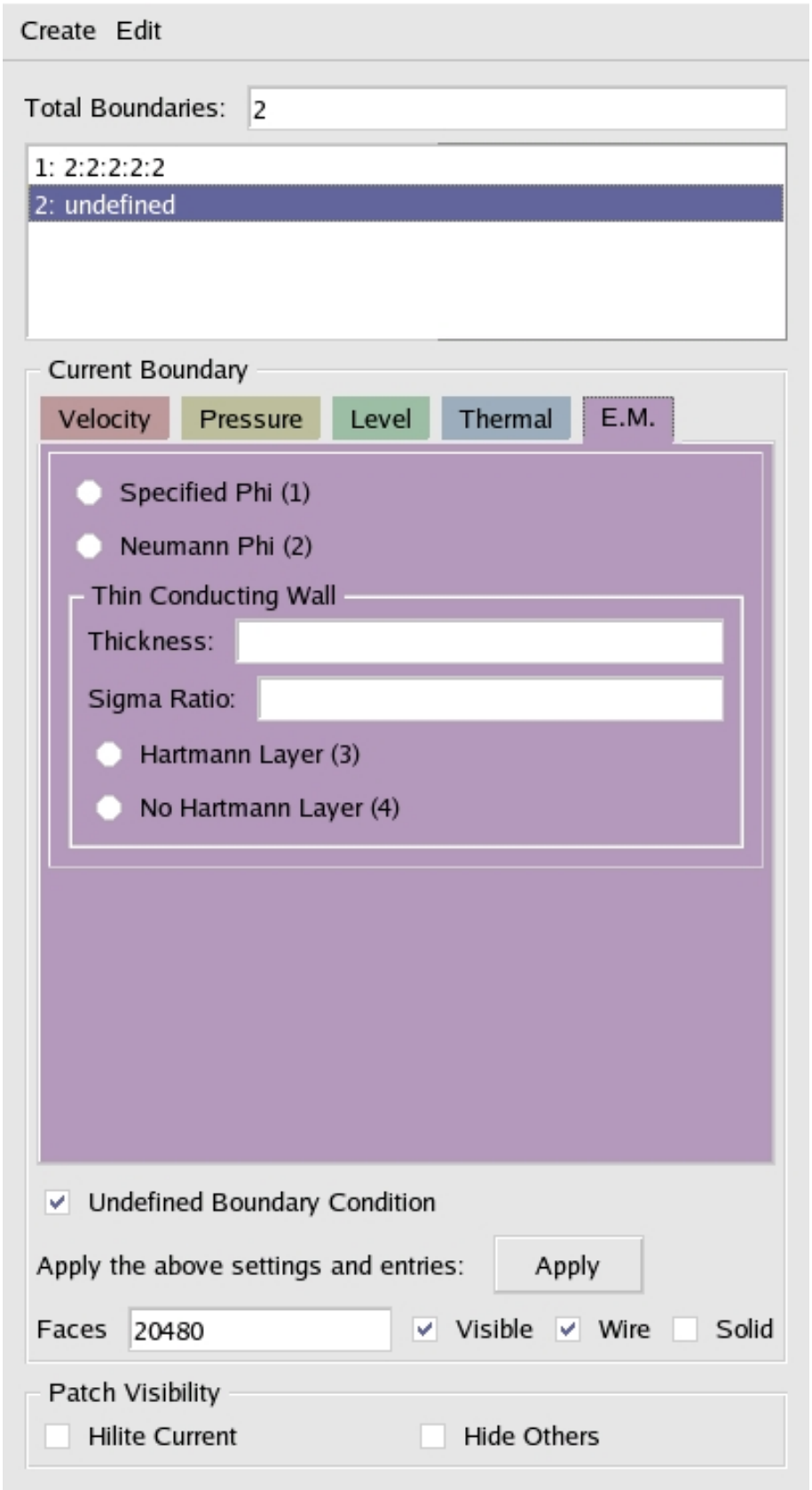


32. Notice that the "Total Boundaries" field indicates that there are now 2 patches.

33. Next the new boundary will be assigned a boundary condition in the same fashion as the first one.
34. Select the “Velocity” tab; and then select the “No Slip / Viscous Wall” button within it. Note that the option for “No Slip / Viscous Wall” is 5.
35. The panel should now look like this:

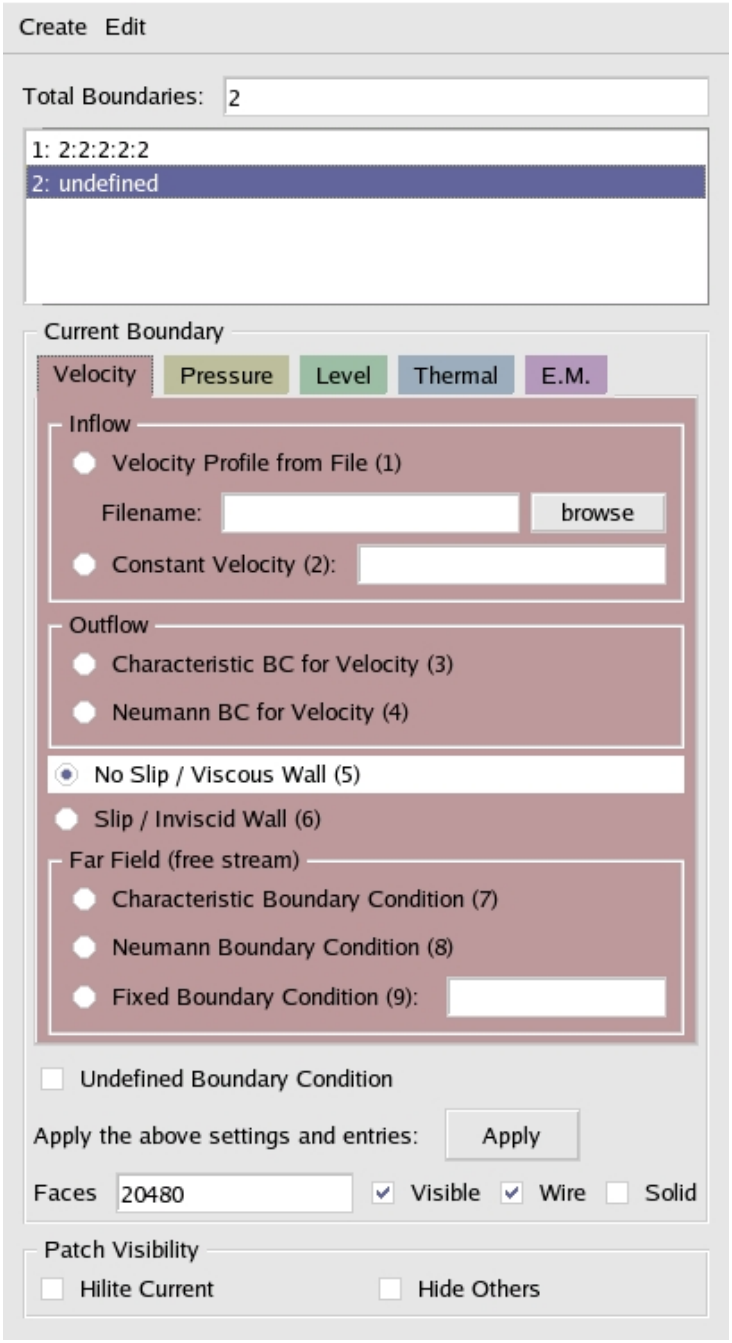


36. Select the “Pressure” tab; and then select the “Neumann” button within it.
37. Select the “Level” tab; and then select the “Neumann” button within it.
38. Select the “Thermal” tab; and then select the “Neumann” button within it.
39. Select the “E.M.” tab; and then select the “Neumann Phi” button within it.
40. With all five aspects of the boundary condition defined, hit the “Apply” button to assign it to the current patch.
41. The panel should now look like this:

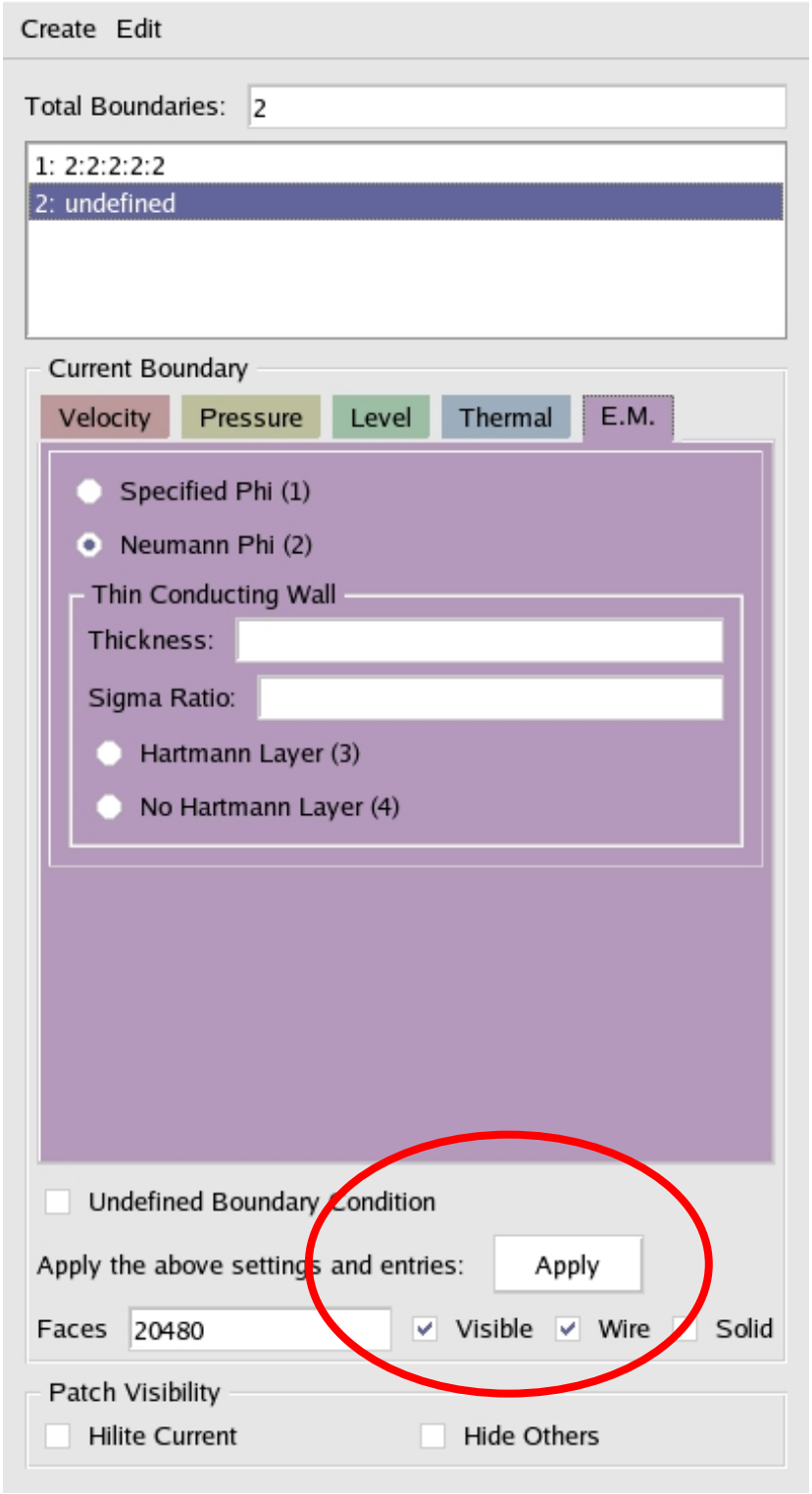


42. PATCH COLORS: After each boundary condition assignment a specific color is assigned to that patch in the main window. The color will have a hue, saturation, and value based upon the type of boundary condition assigned. In this example, you will notice that the z=1 plane is a light shade of green while the remainder of the cube is pale blue.
43. MANIPULATING THE GEOMETRY: The geometry can be scaled, rated, and translated to aid in the viewing of the geometry as well as the boundary condition assignment of its patches.

44. SCALING / ZOOMING: On a three button mouse, dragging upward (toward the monitor) with the ********** mouse button depressed will scale / zoom ****; dragging downward (toward the user) with the same button depressed will scale / zoom *****.
45. SCALED OUT:

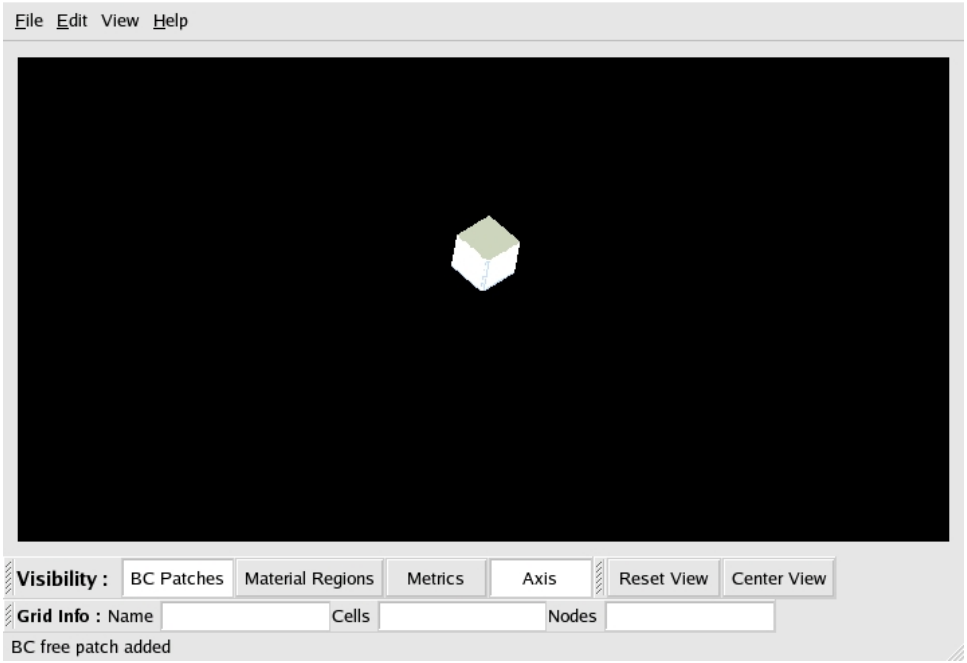


46. SCALED IN:

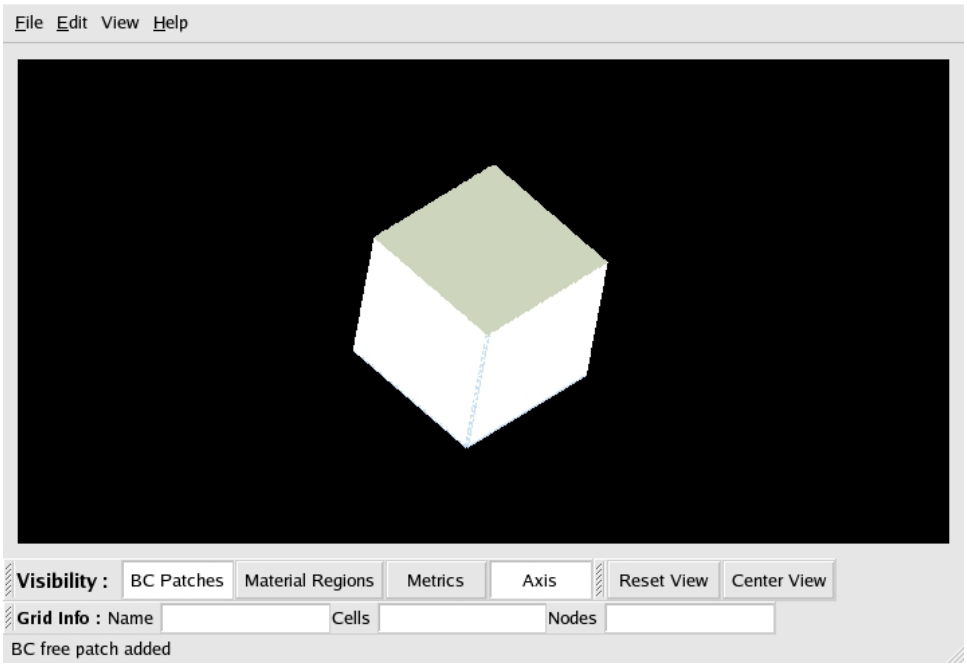


47. TRANSLATION: On a three button mouse, dragging the mouse in any direction while depressing the ******* button will translate the geometry in the same direction along the plane facing the user.

48. Translating by dragging to the left:

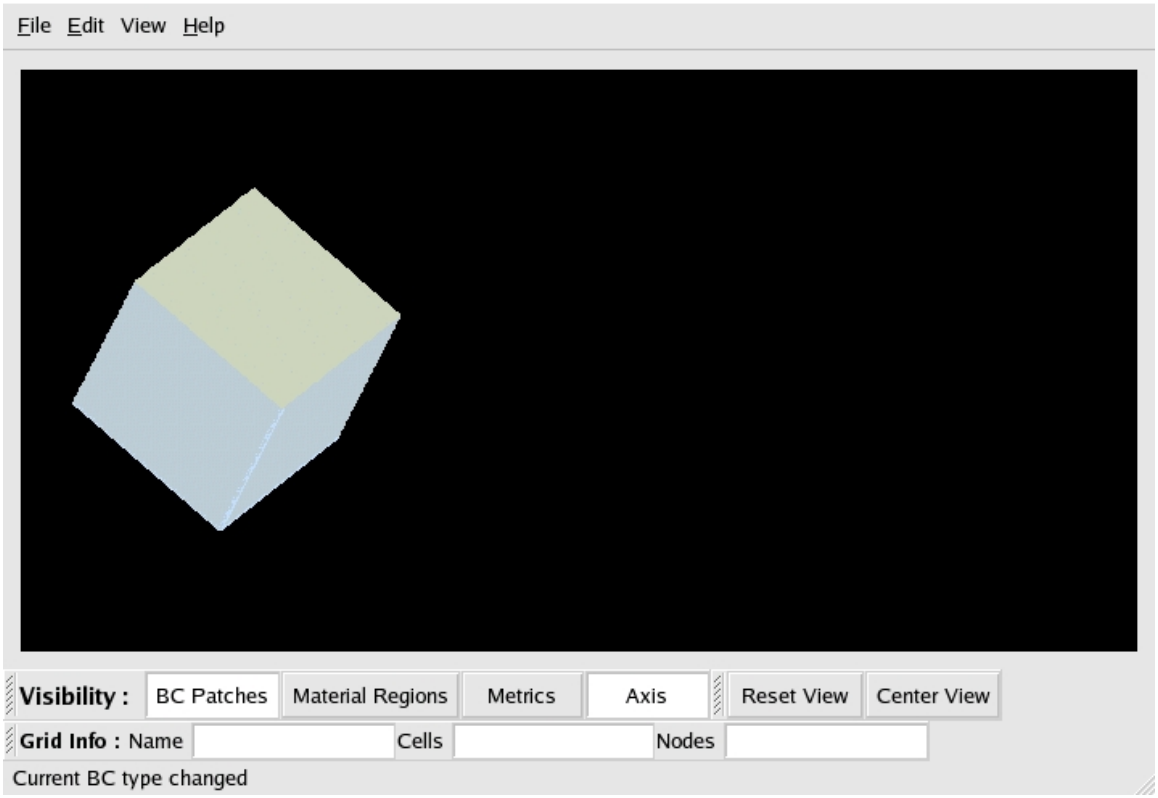


49. ROTATION: On a three button mouse, dragging upward (toward the monitor) with the ********** mouse button depressed will rotate ****; dragging downward (toward the user) with the same button depressed will rotate *****.
50. FILE SAVING: Saving in HIMAG-prep writes the boundary condition, patch information, and materials information of a geometry to a file. The file usually has the same root name as the current geometry but ends with the .ugm extension. This special file is searched for by HIMAG-prep whenever a geometry is loaded. By naming the file after the geometry, the user can conveniently load the .ugm information and the geometry file at the same time.
51. SAVE: If no .ugm file exists for the current geometry, selecting "Save" from the "File" menu on the top menu bar on the main window will save the .ugm file the same root name as the current geometry. If a .ugm is already loaded, the file is saved with the name unchanged.

52. Select "Save" from the "File" menu. If the tutorial has not been completed before and no cube.ugm loaded when the cube.ux geometry file was loaded, then HIMAG-prep will automatically create a file called "cube.ugm" and save patch related information in it. If the tutorial has been completed before, then HIMAG-prep will simply rewrite to the .ugm file already loaded (which should be "cube.ugm").

53. SAVE AS: It is also useful to have multiple sets of boundary condition / material information .ugm files for single geometry, therefore the user can name the .ugm themselves. Selecting "Save As" from the "File" menu opens a file save dialog that allows the user to save the current boundary condition, materials information, and patch information under a new name.

54. Select "Save As" from the "File" menu. A file save dialog will pop up prompting you to save the current .ugm file under a name of your choosing. Save the file as "cube2.ugm." The dialog should now look like this:

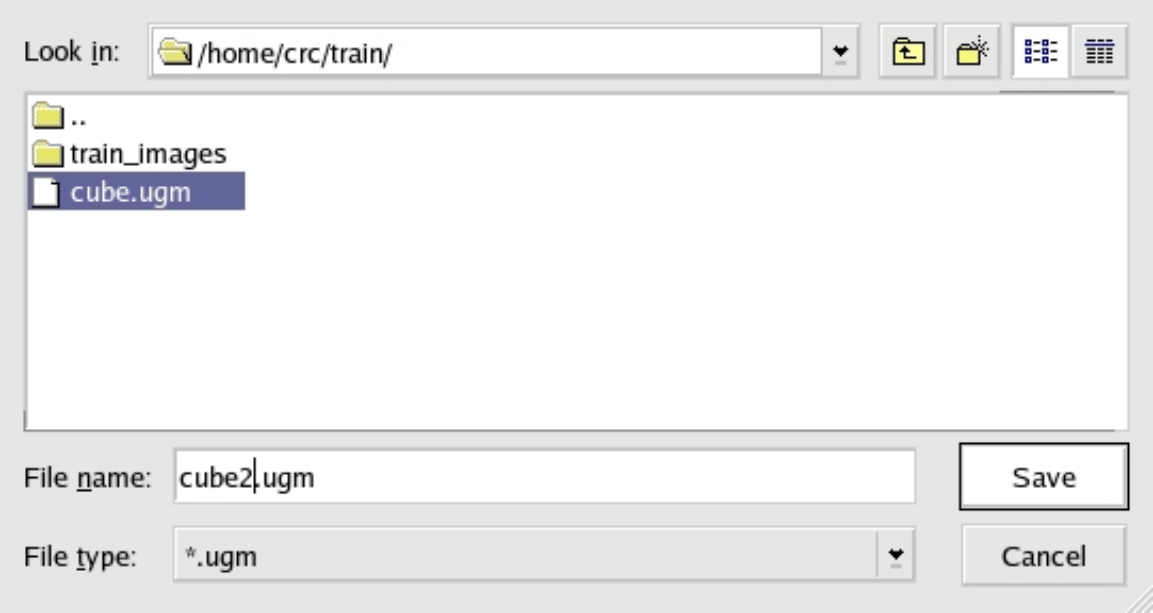


55. OPEN: If there are multiple .ugm files for a particular geometry, the user can swap the .ugm file (thus changing the boundary condition information, etc.) once the geometry is loaded. This is done by selecting "Open" from the "File" menu. Doing so opens a file open dialog which allows the user to select a different .ugm file from the one currently loaded.
56. Select "Exit" from the "File" menu. This closes the HIMAG-prep program.
57. Run HIMAG-prep again by repeating step one.
    a. Host:> prep

58. This time when you load cube.ux the cube.ugm file will automatically load along with it resulting in your cube appearing in the main window.

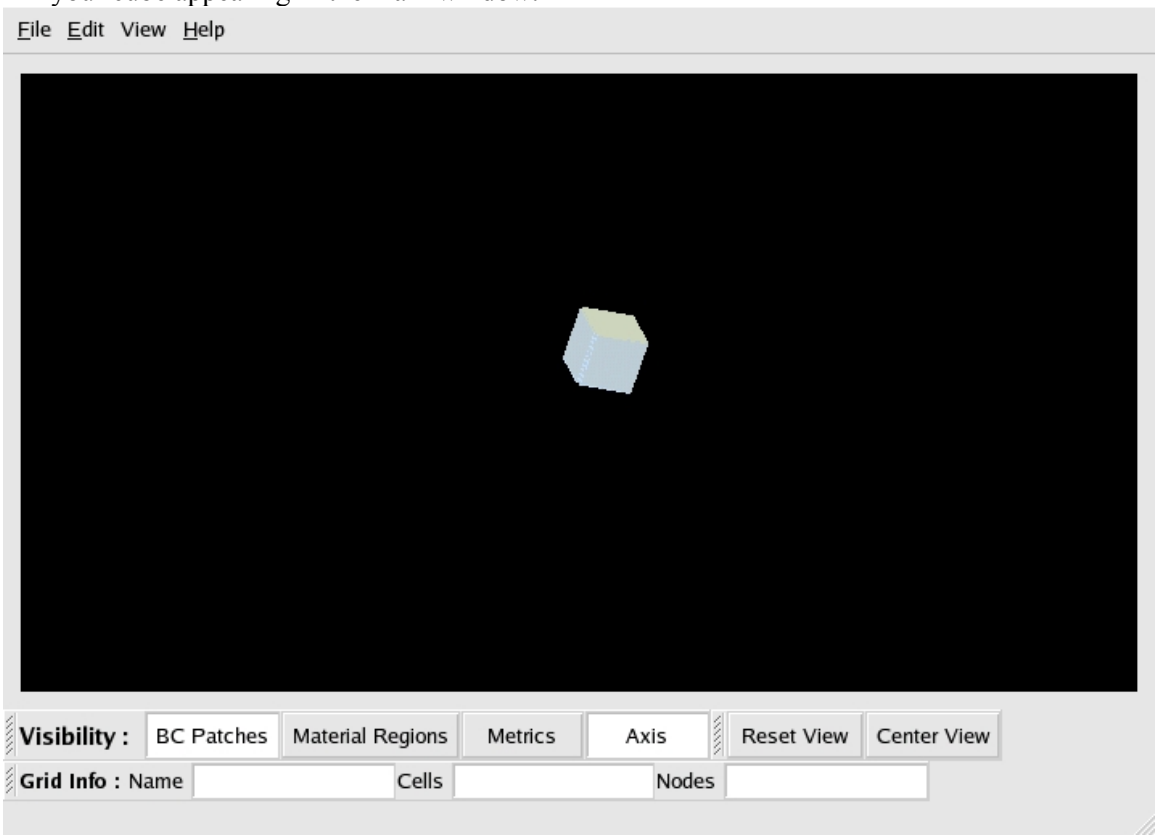


59. Open the Boundary Condition panel and you will notice that the panel is set with the information from the session you just completed.

60. Select “Open” from the “File” menu. You may now choose “cube2.ugm” from the file open dialog. If you made any changes between cube.ugm and cube2.ugm, they would be reflected after loading.

61. This concludes the Cube Tutorial.

**Fully Developed Flow in a Square Duct**

- Get grid input data file: JOB.inp (huntful.inp)
- Run xyz (input as required: nopt=1, filename, nout=0)
- univbk (univ.cemgrd → fort.21)
- move fort.21 JOB.ux
- prep (saved as JOB.ugm)
- ux2part (partitioning, for multi-CPUs only, → JOB.NN.color)
- colormhd (→ partition.NN.ux, etc.)

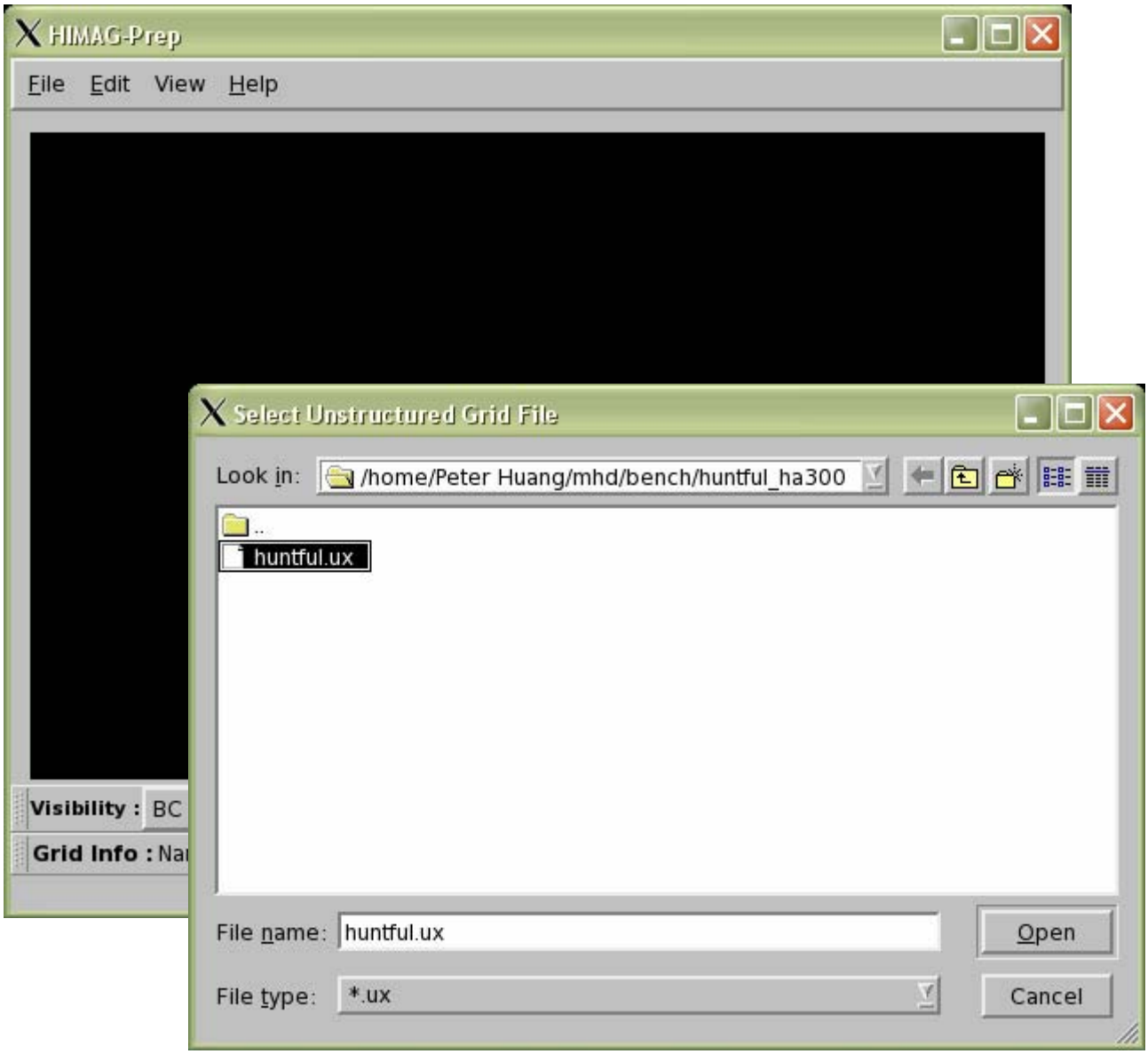

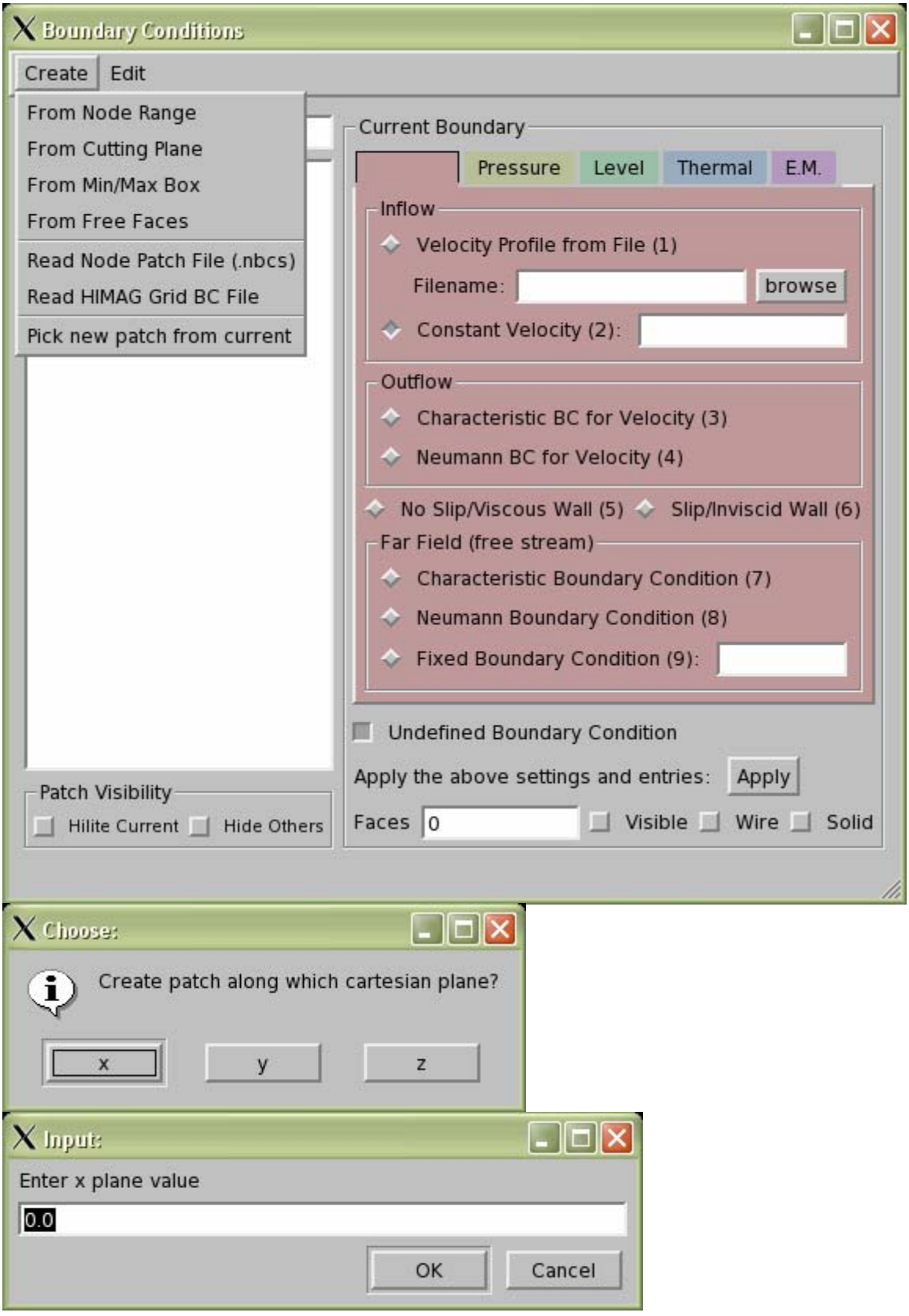
Boundary Conditions
Create
Edit
From Node Range
From Cutting Plane
From Min/Max Box
From Free Faces
Read Node Patch File (.nbcs)
Read HIMAG Grid BC File
Pick new patch from current
Current Boundary
Pressure
Level
Thermal
E.M.
Inflow
Velocity Profile from File (1)
Filename:
browse
Constant Velocity (2):
Outflow
Characteristic BC for Velocity (3)
Neumann BC for Velocity (4)
No Slip/Viscous Wall (5)
Slip/Inviscid Wall (6)
Far Field (free stream)
Characteristic Boundary Condition (7)
Neumann Boundary Condition (8)
Fixed Boundary Condition (9):
Undefined Boundary Condition
Apply the above settings and entries:
Apply
Faces
0
Visible
Wire
Solid
Patch Visibility
Hilite Current
Hide Others
Choose:
Create patch along which cartesian plane?
x
y
z
Input:
Enter x plane value
0.0
OK
Cancel

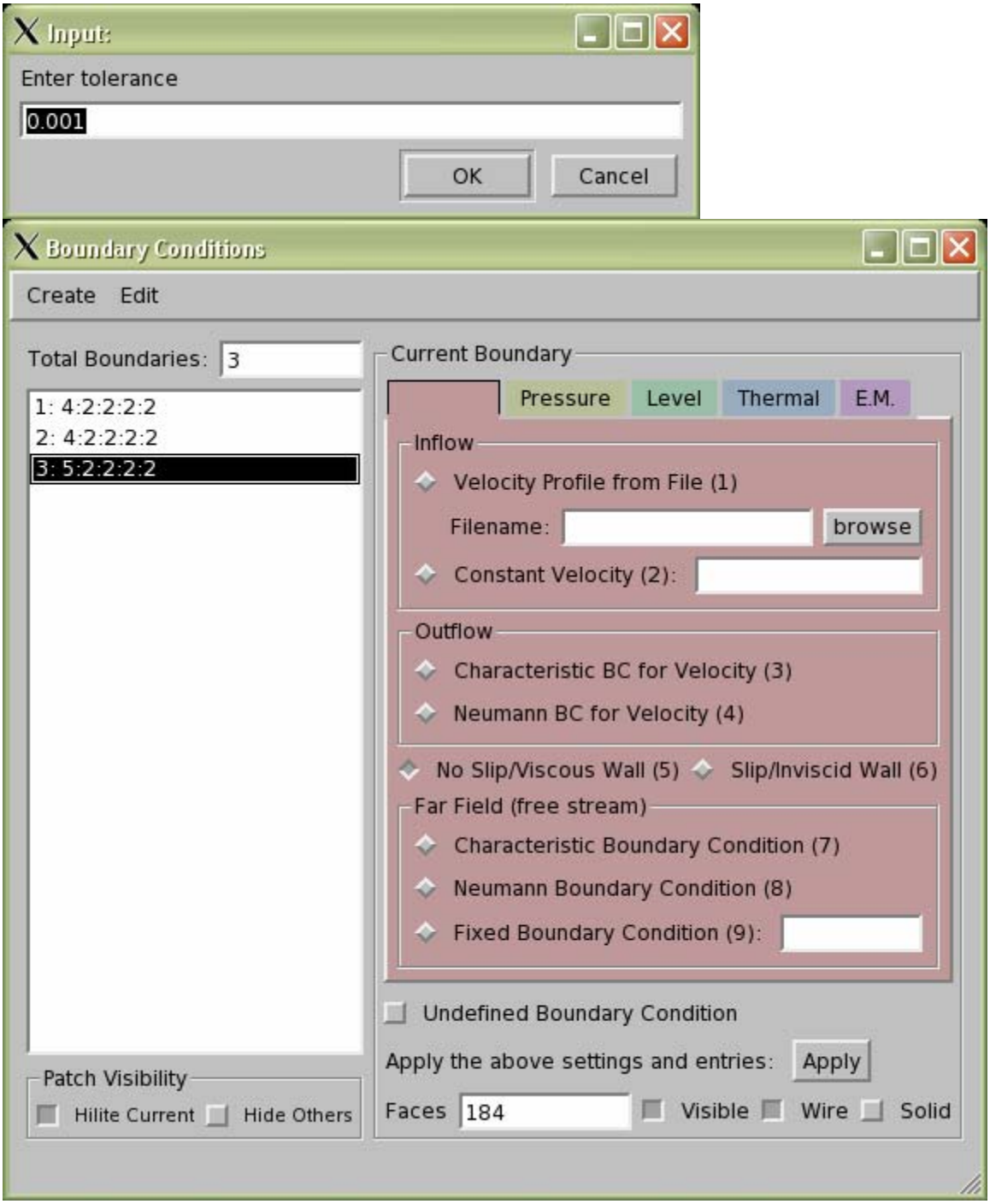
Input:
Enter tolerance
0.001
OK
Cancel
Boundary Conditions
Create
Edit
Total Boundaries: 3
1: 4:2:2:2:2
2: 4:2:2:2:2
3: 5:2:2:2:2
Current Boundary
Pressure
Level
Thermal
E.M.
Inflow
Velocity Profile from File (1)
Filename:
browse
Constant Velocity (2):
Outflow
Characteristic BC for Velocity (3)
Neumann BC for Velocity (4)
No Slip/Viscous Wall (5)
Slip/Inviscid Wall (6)
Far Field (free stream)
Characteristic Boundary Condition (7)
Neumann Boundary Condition (8)
Fixed Boundary Condition (9):
Undefined Boundary Condition
Apply the above settings and entries:
Apply
Patch Visibility
Hilite Current
Hide Others
Faces 184
Visible
Wire
Solid

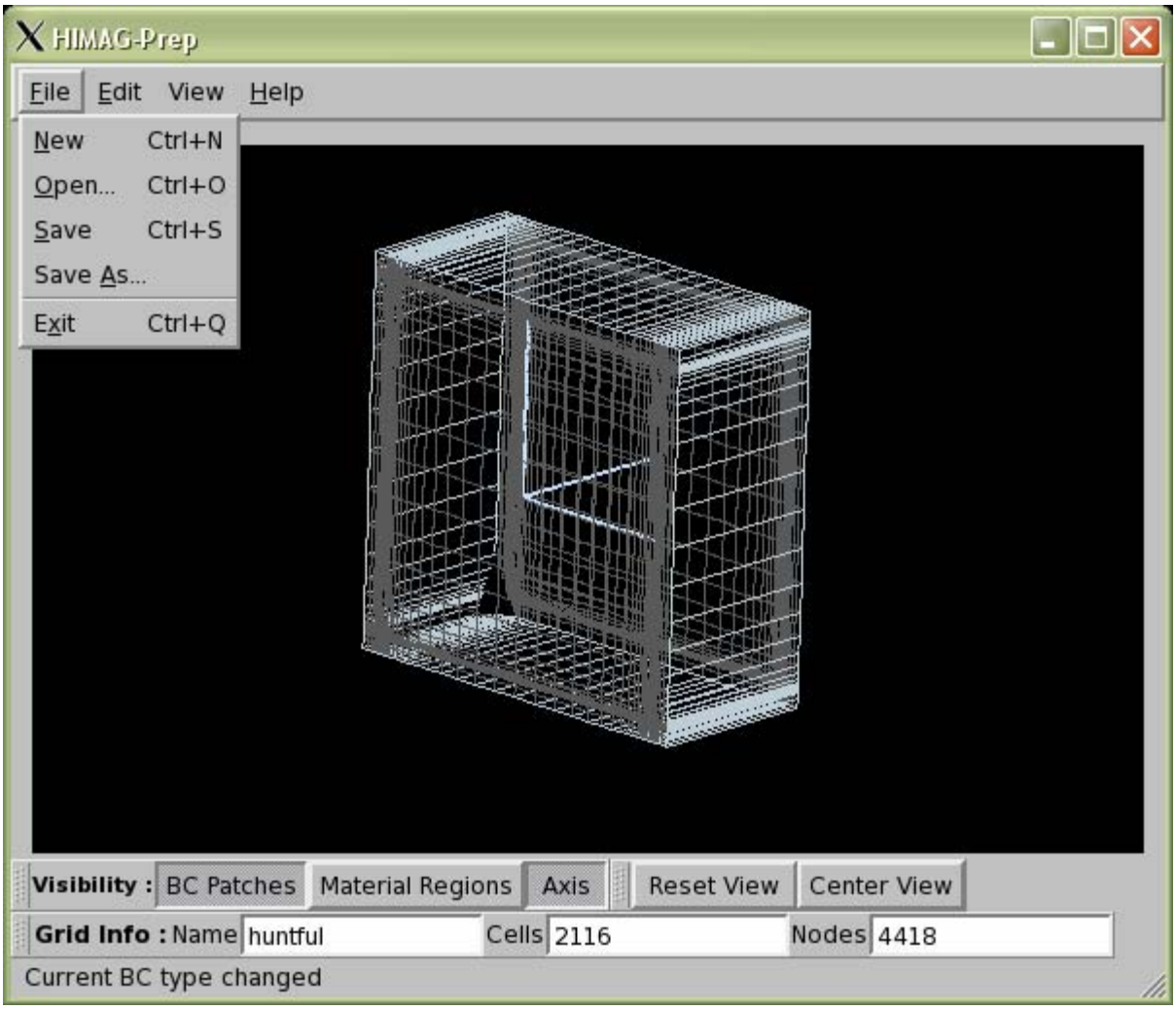
HIMAG-Prep
File
Edit
View
Help
New Ctrl+N
Open... Ctrl+O
Save Ctrl+S
Save As...
Exit Ctrl+Q
Visibility :
BC Patches
Material Regions
Axis
Reset View
Center View
Grid Info : Name
huntful
Cells
2116
Nodes
4418
Current BC type changed

**UX2PART**

This utility "colors" a given mesh into nearly equal partitions, following the KMETIS algorithm. Following screenshots represent the stages of execution, at the end of which a .color file is created.

1. Select the UX file
2. Select the number of partitions to create
3. Select a weighting factor: Use 1 for HIMAG
4. Select PEC cell weight: Use 0 for HIMAG

1

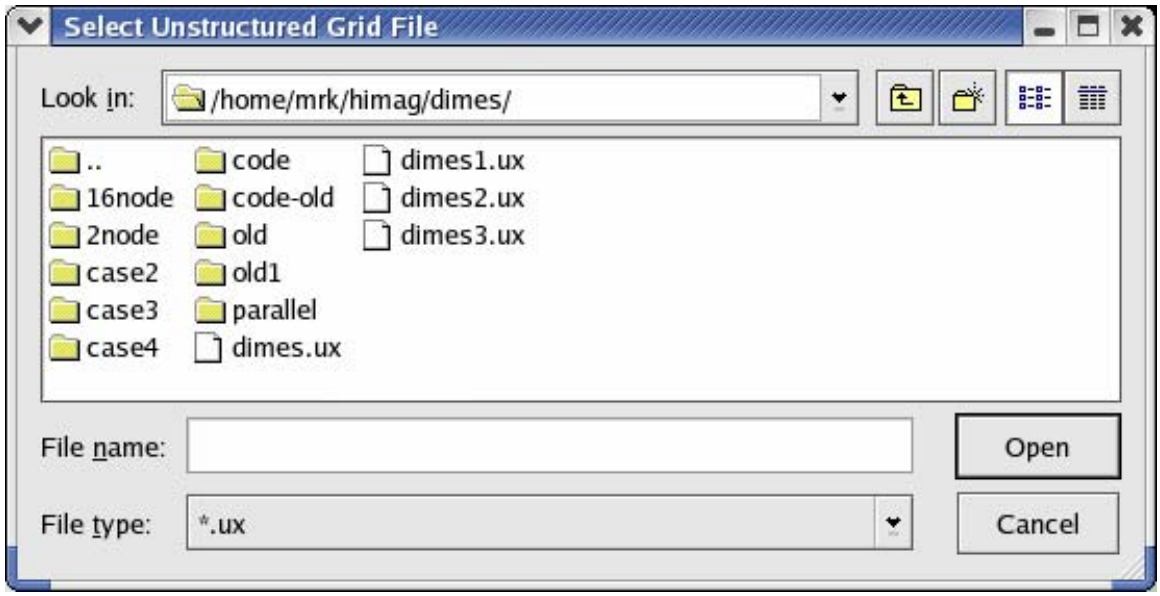


2

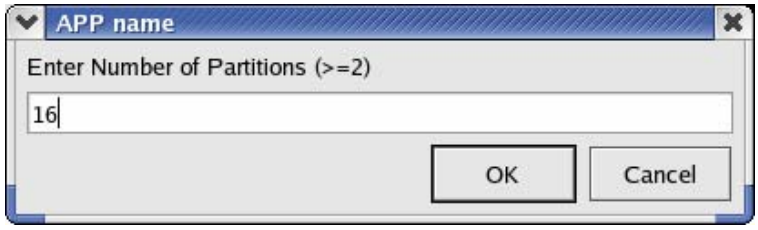


3

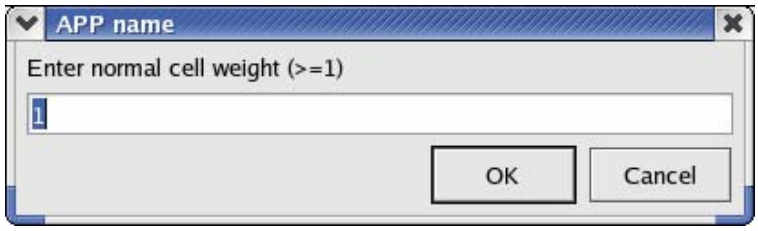


4

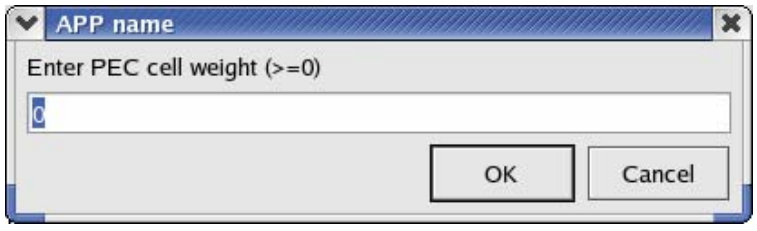

**COLORMHD**

This utility uses the color file generated by UX2PART and creates partitioned grid and BC files for each CPU. The partitions will be numbered from 0 to N-1 where N is the number of CPUs. Following screenshots depict stages of execution, at the end of which a set of files named partition.?.patch, partition.?.ux and partition.?.ugm will be created where ? runs from 0 to N-1.

1. Select the UX file
2. Select the .color file name

1. 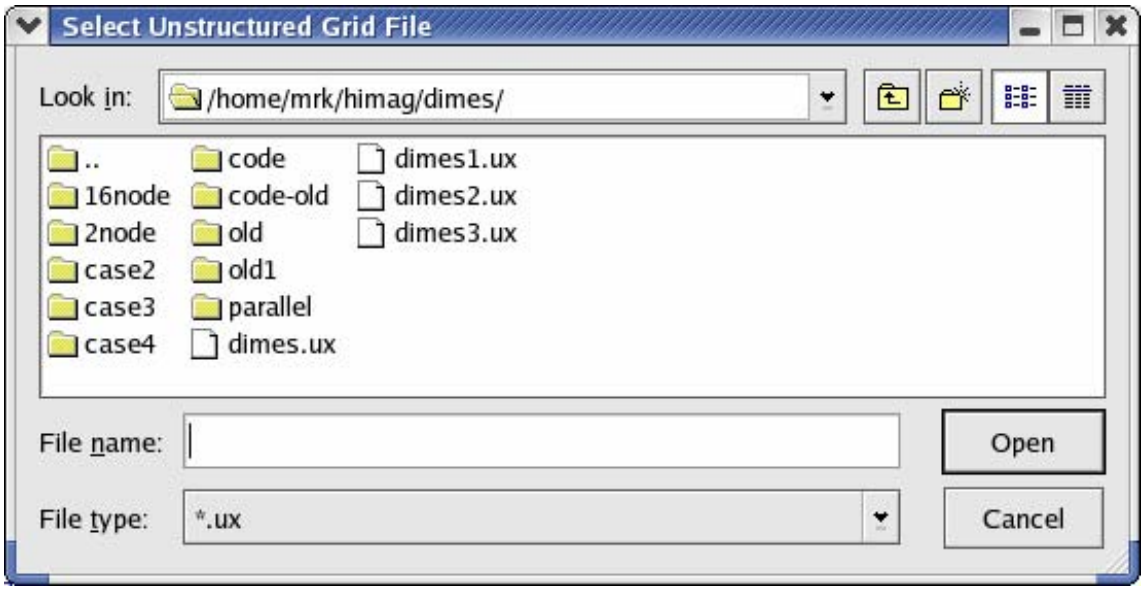


2. 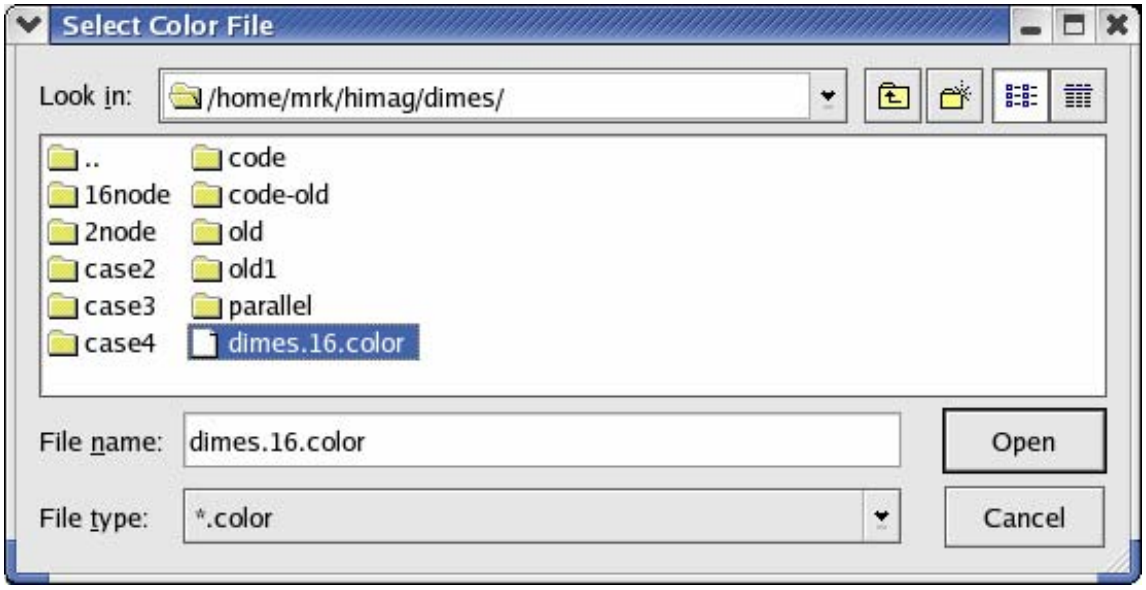

## INPUT FILE

The following is a detailed list of parameters used in the input file to HIMAG.

```
  * Default file name: mhd.input
  * If value is not defined in the input data file, a default value is used
```

| Variable | Values | Description |
|---|---|---|
| nodes | Integer >0 | Number of CPUs |
| iread | Integer | Start/Restart<br>= 0: Fresh start<br>= 1: restart from qrestart.*.unf<br>= 2: restart from qrestart2.*.unf<br>= 10: restart from Tecplot file interpolation |
| grid_scale | Real > 0. | scale x-y-z coordinates from UX file |
| istart | Integer >=0 | First step to output solution, default to iskip |
| nmax | Integer | Maximum number of steps to run<br>= 0: write initial values for check and stop<br>< 0: iread=0: write material region data only<br>iread><0: reset nstart and nmax=\|nmax\| |
| iskip | Integer >0 | skip steps to output solution, default to nmax+1 |
| nwrite | Integer | skip steps to write restart files<br>= -1: for nvel=23 only (reset to \|nmax\|)<br>write fully developed solution for restart<br>> nmax: no restart files written<br><= nmax: write qrestart*.*.unf every nwrite step |
| dtime | Real | > 0.0: constant dt=dtime<br>< 0.0: variable time-step, minimum dt=\|dtime\| |
| cfl | Real | parameter used for variable time-step |
| dratio | Real | Fluid density ratio = rho1/rho2 |
| vratio | Real | Fluid viscosity ratio = v1/v2 |
| hkrat | Real | Heat conductivity ratio = k1/k2 |
| visc1 | Real | Fluid viscosity v1 |
| vss | Real | Solid viscosity vss (default=1.e10*v1) |
| rho1 | Real | Fluid density |
| rhos | Real | Solid density (default=2*rho1) |
| sgmf1 | Real | Fluid electrical conductivity sigma1 |
| sgmw1 | Real | Solid electrical conductivity (for imtype=3) |
| sgmw2 | Real | Solid electrical conductivity (for imtype=4) |
| alpha | Real <=1. | Pre-conditioning factor |
| omega | Real >=1. | Acceleration factor (default=1.92) |

| | | |
|---|---|---|
| ubar | Real | mean inflow velocity<br>> 0.0: along axis<br>< 0.0: opposite to axis |
| bval | Real | B-field strength |
| bx0 | Real | <= xmin: B-field all constant<br>> xmin: B-field ramped from bx0 |
| twal | Real >0. | Conducting wall thickness (for Cw and ymax, ymin) |
| dpdx | Real | dp/dx, used for fully-developed<br>or used to calculate initial Hunt's solution |
| c_rest | Real | Coefficient of contact resistance |
| lambda | Real <=1. | =1.0: No upwinding (default)<br><1.0: Upwing scheme parameter |
| epsln | Real | epsilon for level-set (default=0.1) |
| hk1 | Real | Fluid thermal Conductivity k1 |
| cp1 | Real | Fluid specific heat capacity Cp1 |
| hkw1 | Real | Solid thermal Conductivity (for imtype=3) |
| cpw1 | Real | Solid specific heat capacity (for imtype=3) |
| tref | Real | Reference temperature (initial temperature) |
| deltT | Real | Temperature difference (for Boussinesq fluid) |
| gras | Real | Grashof number |
| dfu1 | Real | Fluid diffusivity d1 (for Tritium) |
| ad12 | Real | Fluid diffusion coefficient d1/d2 (for Tritium) |
| ak12 | Real | Fluid Solubility ratio k1/k2 (for Tritium) |
| qht1 | Real | Fluid heat source Q (for tritium) |
| web | Real <1.e6 | Weber number (for level-set) |
| iortho | Integer | =1: for orthogonal grid, without correction<br>=2: Non-orthogonal correction |
| nvel | Integer | Initial velocity option if imtype=0<br>=0: initially at rest (except inflow faces)<br>=1: uniform (=ubar)<br>=2: parabolic profile<br>=3: duct flow profile<br>=4: Shercliff's flow profile<br>=5: Hunt's flow profile<br>=23: Use fully developed solution for 3-D<br>=-1: add perturbation to current solution |
| nmomt | Integer | =0: Momentum equation not solved<br>=1: Momentum equation solved |
| nppe | Integer | =0: Not solve Pressure Poisson equation<br>=1: Solve Pressure Poisson eq with CG<br>=2: Solve Pressure Poisson eq with relaxation |
| solver | | |

| | | |
|---|---|---|
| nmhd | Integer | =0: Not solve MHD Poisson equation<br>=1: Solve MHD equation with CG<br>=2: Solve MHD equation with relaxation solver<br>=3: Solve 2-D MHD with d/dz=0, with source term<br>=4: Solve MHD B-formulation equation |
| nheat | Integer | =0: Heat equation not solved<br>=1: Heat equation solved |
| ilaw | Integer | =0: Constant density and viscosity (default)<br>=1: Sutherland's form<br>=2: Arrhenius form<br>=3: Linear inverse variation with temperature |
| ilevels | Integer | =0: Single phase flow<br>=1: Two-phase flow, level-set equation solved |
| iuvw | Integer | Option for inflow/outflow direction<br>= 1-3: Both inflow/outflow along x-, y-, z-axis<br>=11-13: Outflow along x-, inflow along x-, y-, z-axis<br>=21-23: Outflow along y-, inflow along x-, y-, z-axis<br>=31-33: Outflow along z-, inflow along x-, y-, z-axis |
| ntrit | Integer | =0: Tritium transport not solved<br>=1: Tritium transport solved |
| iwall | Integer | =0: Normal solution at Hartmann layer<br>=1: Use wall function at Hartmann layer |
| ineump | Integer | =0: Defined some Dirichlet Pressure BC<br>=1: All Neumann Pressure BC |
| ineumm | Integer | =0: Defined some Dirichlet MHD BC<br>=1: All Neumann MHD BC |
| ngrad | Integer | =1: grad(phi) from subr. gradient<br>=2: grad(phi) from face values averaged (default)<br>=3: grad(phi) from face values and non-orth averaged<br>=4: grad(phi) by least-sqaure scheme<br>=5,6: grad(phi) by conservative scheme |
| ichan | Integer | Channel type<br>=0: Shercliff case (duct flow without walls)<br>=1: Hunt case (duct flow with walls)<br>=10: Circular duct (wall thickness = twal)<br>=2: Material regions from mat.bin file<br>=3: Modified Pb-Li concept (without mat.bin)<br>=5: Others: Special case by user |
| nskp | Integer | skip steps for output residuals, etc. |

```
ipmax       Integer          Number of iterations for Pressure Poisson
immax       Integer          Number of iterations for MHD Poisson
igmax       Integer          Number of non-orthogonal iteration
epsmin      Integer          Minimum Residual criterion (log)

ibuoy       Integer          =0: without buoyancy term
                             =1: with buoyancy term

igravt      Integer          =0: without Gravity term
                             =1: with Gravity term

idissp      Integer          =0: without Viscous dissipation term
                             =1: with Viscous dissipation term

gx          Real             Gravity x-component
gy          Real             Gravity y-component
gz          Real             Gravity z-component

iforce      Integer          =0: do not calculate force/moment
                             =1: calculate force (Fx,Fy,Fz) on ivel=8 BC
                             =2: calculate force and moment (Mx,My,Mz) on
ivel=8
xcent       Real             Torque center x-coordinate
ycent       Real             Torque center y-coordinate
zcent       Real             Torque center z-coordinate

Output data
===========
  * op.cur
    Reprint of most input or default parameters used for the run
    Check the data to see if there are any unexpected/incorrect values

  * qrestart.*.unf or qrestart2.*.unf or qrest2d.unf (nvel=23)
    Restart binary data file

  * tec.nnn.*.dat
    Output solution for every nwrite steps (nnn is node_id)

Other data files needed
=======================
  * JOBNAME.ux, JOBNAME.ugm, [mat.bin]
    grid and BC patches, [and material patches]

  * JOBNAME.N.color
    partitioning color file (N is number of CPU nodes)

  * partition.0NN.ux, partition.0NN.ugm, partition.0NN.patch
    partitioned grid and BC and patch files for each node_id=0NN
```

**MHD2TEC**

This utility converts the raw output data created by each CPU into a consolidated and smoothly interpolated TECPLOT data file. Following screenshots depict the various steps involved, leading to the creation of files named <casename>.<timestep>.dat:

1. Select the UX file
2. Respond to the parallel/non-parallel question. If parallel select the color file
3. Respond "Yes" to "use face list?" question if you wish to extract data at a material interface. You will need a .list file generated by PREP in order to use this feature. You will be then prompted to select this file.
4. Select the starting time step for creating tecplot files, followed by increments in time step and the final time step when to stop the data conversion process.

1

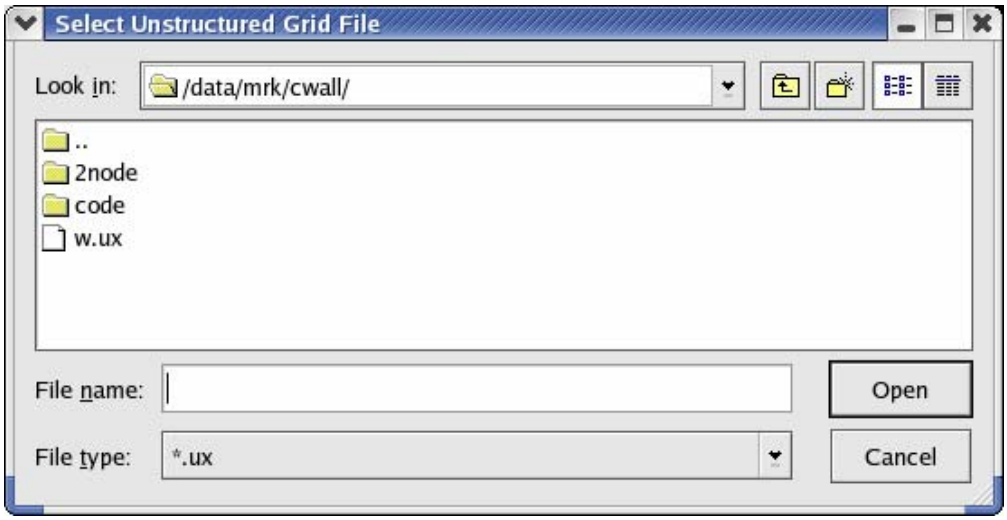


2

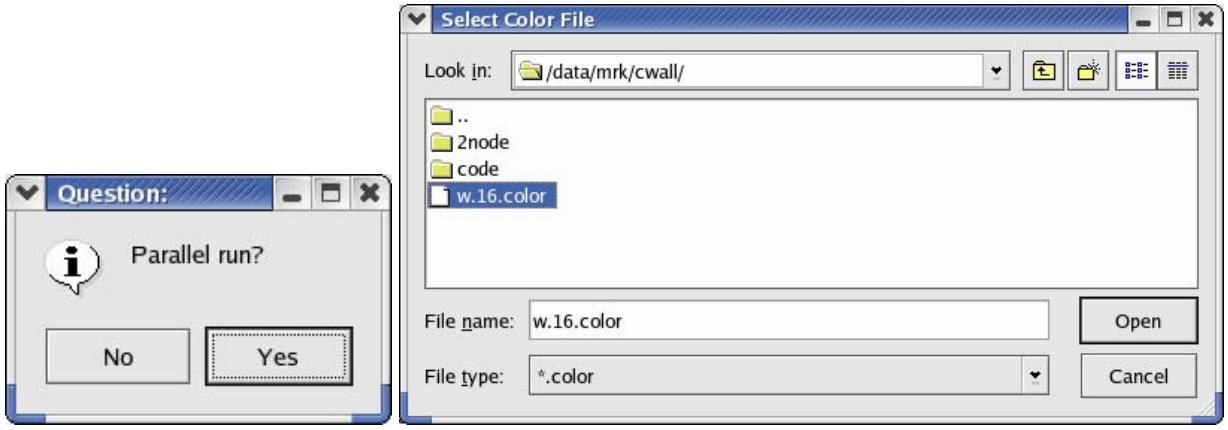

3

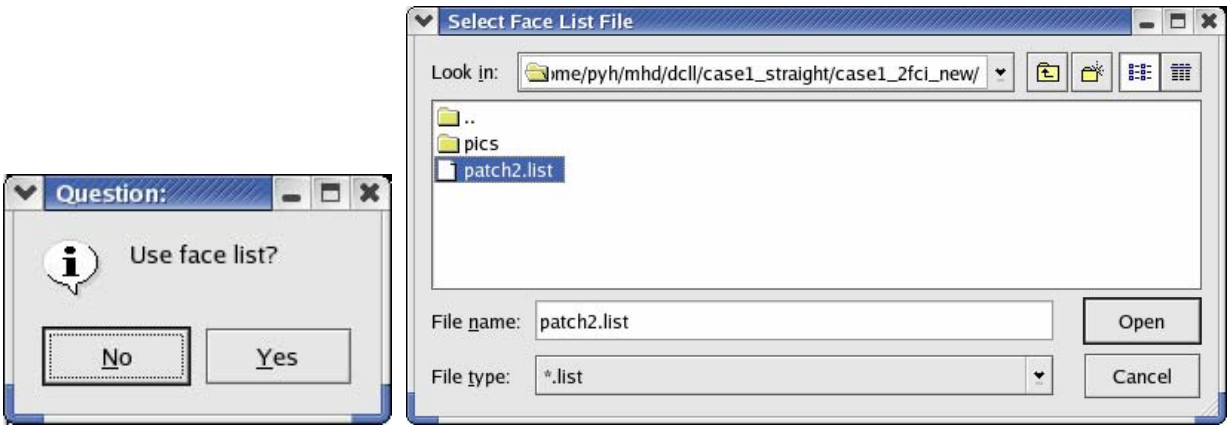
Question:
Use face list?
No
Yes
Select Face List File
Look in:
me/pyh/mhd/dcll/case1_straight/case1_2fci_new/
..
pics
patch2.list
File name:
patch2.list
Open
File type:
*.list
Cancel

4

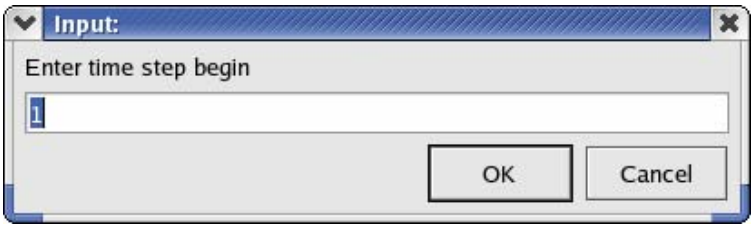
Input:
Enter time step begin
1
OK
Cancel

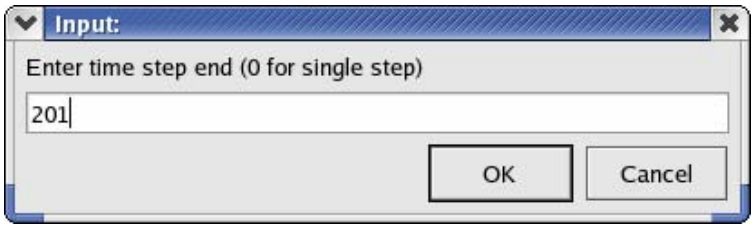
Input:
Enter time step end (0 for single step)
201
OK
Cancel

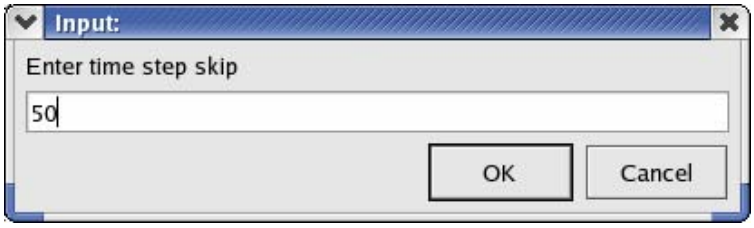
Input:
Enter time step skip
50
OK
Cancel

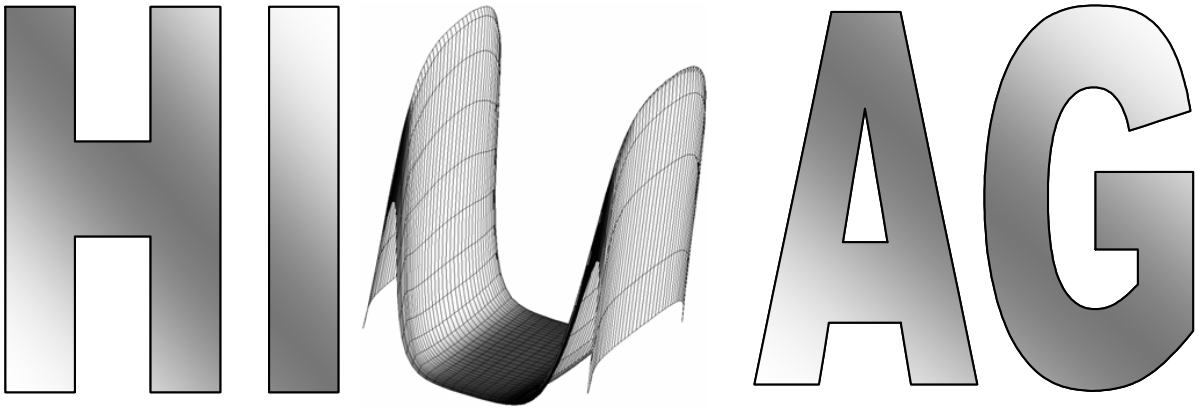

**H**yPerComp **I**ncompressible **M**HD solver for **A**rbitrary **G**eometry



# Test Cases

**Case-1: 2-D Flow in a rectangular duct**

In this case, we model the flow in a 2-D rectangular duct in the x-y plane, where the flow is in the x-direction and a magnetic field varying with x is applied along the y-direction. A schematic is shown below.

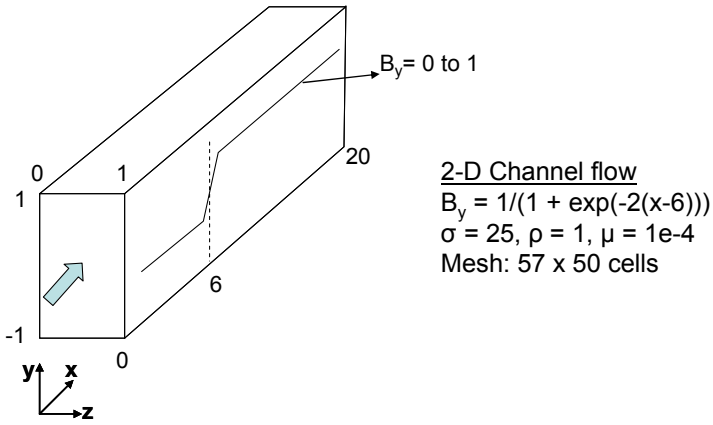


2-D Channel flow
$B_y = 1/(1 + \exp(-2(x-6)))$
$\sigma = 25$, $\rho = 1$, $\mu = 1e\text{-}4$
Mesh: 57 x 50 cells

The following input file is used to generate the grid:

```
* Rotation (irot), translation x-, y-, z-
      0           0.0   0.0   0.0
* x-axis: Number of segments (nxsgm), isymx,    xmin,   xmax
                        3     0     0.0   25.0
* #1: nxcel, segment-xmax
      30    7.5
*     Stretch_option, stretching_factor
      0
* #2: nxcel, segment-xmax
      20    20.0
*     Stretch_option, stretching_factor
      1
      1.18
* #3: nxcel, segment-xmax
      7     25.0
*     Stretch_option, stretching_factor
      2
      5.0
* y-axis: Number of segments (nysgm), isymy,    ymin,   ymax
                        3     1     -1.0  1.0
* #1: nycel, segment-ymax
      7     -0.998
*     Stretch_option, stretching_factor
      0
* #2: nycel, segment-ymax
      36    0.998
*     Stretch_option, stretching_factor
      3
      1.0007
* z-axis: Number of segments (nzsgm), isymz,    zmin,   zmax
                        1     0     0.00  1.00
* #1: nzcel, segment-zmax
      1     1.0
*     Stretch_option, stretching_factor
      0
```

Boundary conditions:

Inflow and outflow boundary patches are defined and given appropriate BC numbers in prep. The constant-y walls are viscous walls in the calculation. A single cell is used in the z-direction since this is a 2-D problem. The constant-z boundaries are defined as inviscid walls with Neumann-type BCs on all other quantities.

Input file:
The following input file is used in this calculation.

```
nodes = 1,
iread = 0,
grid_scale = 1.0,

istart = 1000,
nmax   = 10000,
iskip  = 5000,
nwrite = 5000,
dtime  = 5.0e-4,
cfl    = 2.70,

visc1 = 1.0e-4,
rho1  = 1.0,
sgmf1 = 25.,
sgmw1 = 1.0e-10,
sgmw2 = 1.0e-2,
alpha = 1.0,
omega = 1.00,

ubar  = 1.0,
bval  = 1.0,
bx0   = 6.0,
twal  = 0.0,
dpdx  = -0.0,

iortho = 1,
nvel   = 20,
nmomt  = 1,
nppe   = 1,
nmhd   = 3,
nheat  = 0,

ineump = 0,
ineumm = 0,
ichan  = 0,
nskp   = 10,
ipmax  = 20,
immax  = 20,
epsmin = -16.0,
```

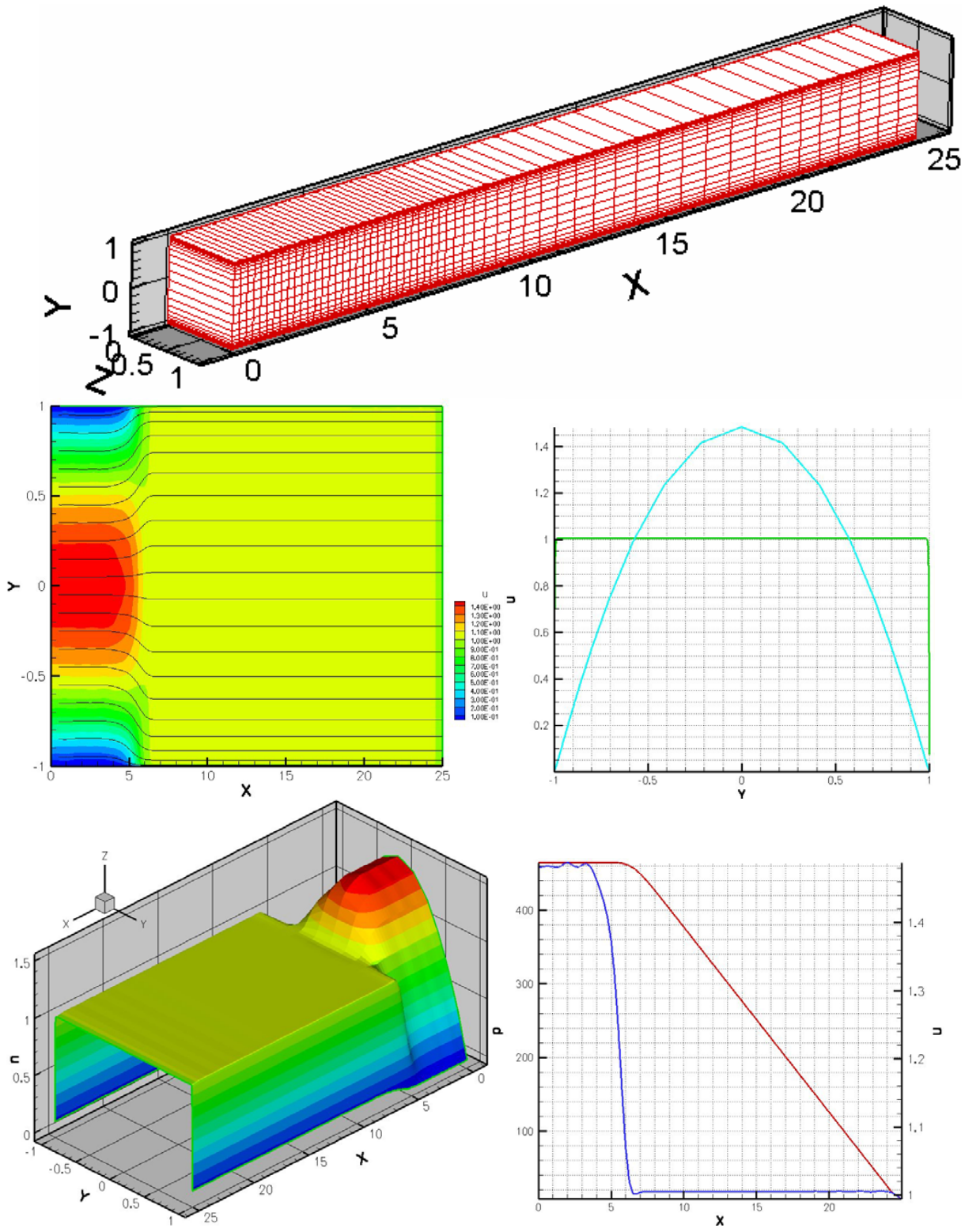


**Figure 1:** Sample results. Grid, velocity contour, extracted velocity profiles, velocity development in the channel and lengthwise variation of pressure and peak velocity

**Case-2: Fully developed flow in a square channel**

In this case, we model flow emerging from a square duct cross section in the y-z plane. Magnetic field is applied in the y-direction and the flow has a x-velocity and a pressure gradient is applied in the x-direction.

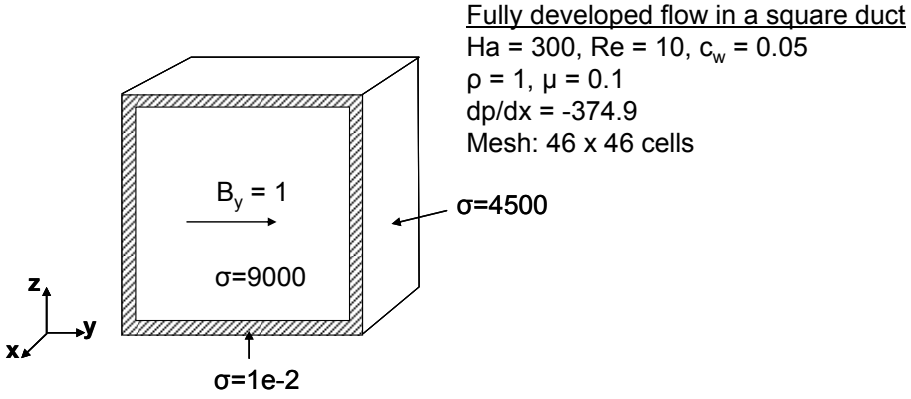


The following input file is used to generate the grid:

```
* x-axis: Number of segments (nxsgm),  isymx,  xmin,   xmax
                        1     0     0.0   1.0
* #1: nxcel, segment-xmax
      1     1.0
*     Stretch_option, stretching_factor
      0
* y-axis: Number of segments (nysgm),  isymy,  ymin,   ymax
                        5     1     -1.1  1.1
* #1: nycel, segment-ymax
      5     -1.0
*     Stretch_option, stretching_factor
      2
      1.005
* #2: nycel, segment-ymax
      5     -0.9965
*     Stretch_option, stretching_factor
      1
      1.400
* #3: nycel, segment-ymax
      26    0.9965
*     Stretch_option, stretching_factor
      3
      1.007
* z-axis: Number of segments (nzsgm),  isymz,  zmin,   zmax
                        5     1     -1.1  1.1
* #1: nzcel, segment-zmax
      5     -1.0
*     Stretch_option, stretching_factor
      2
      1.070
* #2: nzcel, segment-zmax
      5     -0.94
*     Stretch_option, stretching_factor
      1
      1.200
```

```
* #3: nzcel, segment-zmax
      26    0.94
*     Stretch_option, stretching_factor
      3
      1.040
```

Boundary Conditions:
Neumann BCs are used for velocity for the constant x-faces. This is because the flow is fully developed in this direction, and indeed, there is only one cell in the x-direction. All other faces are set to viscous walls. Interior fluid-solid boundaries are always treated as viscous.

Input file:
The following input file is used for the flow solution.

```
   nodes = 1,
   iread = 0,
   grid_scale = 1.0,

   nmax   = 3000,
   iskip  = 3000,
   nwrite = 3000,
   dtime  = 2.0e-4,
   cfl    = 2.70,

   visc1 = 1.0e-1,
   rho1  = 1.0,
   sgmf1 = 9000.,
   sgmw1 = 4500.,
   sgmw2 = 1.0e-2,
   alpha = 1.0,
   omega = 1.92,

   ubar  = 1.0,
   bval  = 1.0,
   twal  = 0.1,
   dpdx  = -374.896134,
   c_rest= 0.0,
   lambda= 1.0,

   iortho = 1,
   nvel   = 0,
   nmomt  = 1,
   nppe   = 0,
   nmhd   = 1,
   nheat  = 0,
   ilevels= 0,

   ineumm = 1,
   ngrad  = 2,
   ichan  = 1,
   nskp   = 10,
   immax  = 20,
   epsmin = -16.0,
```

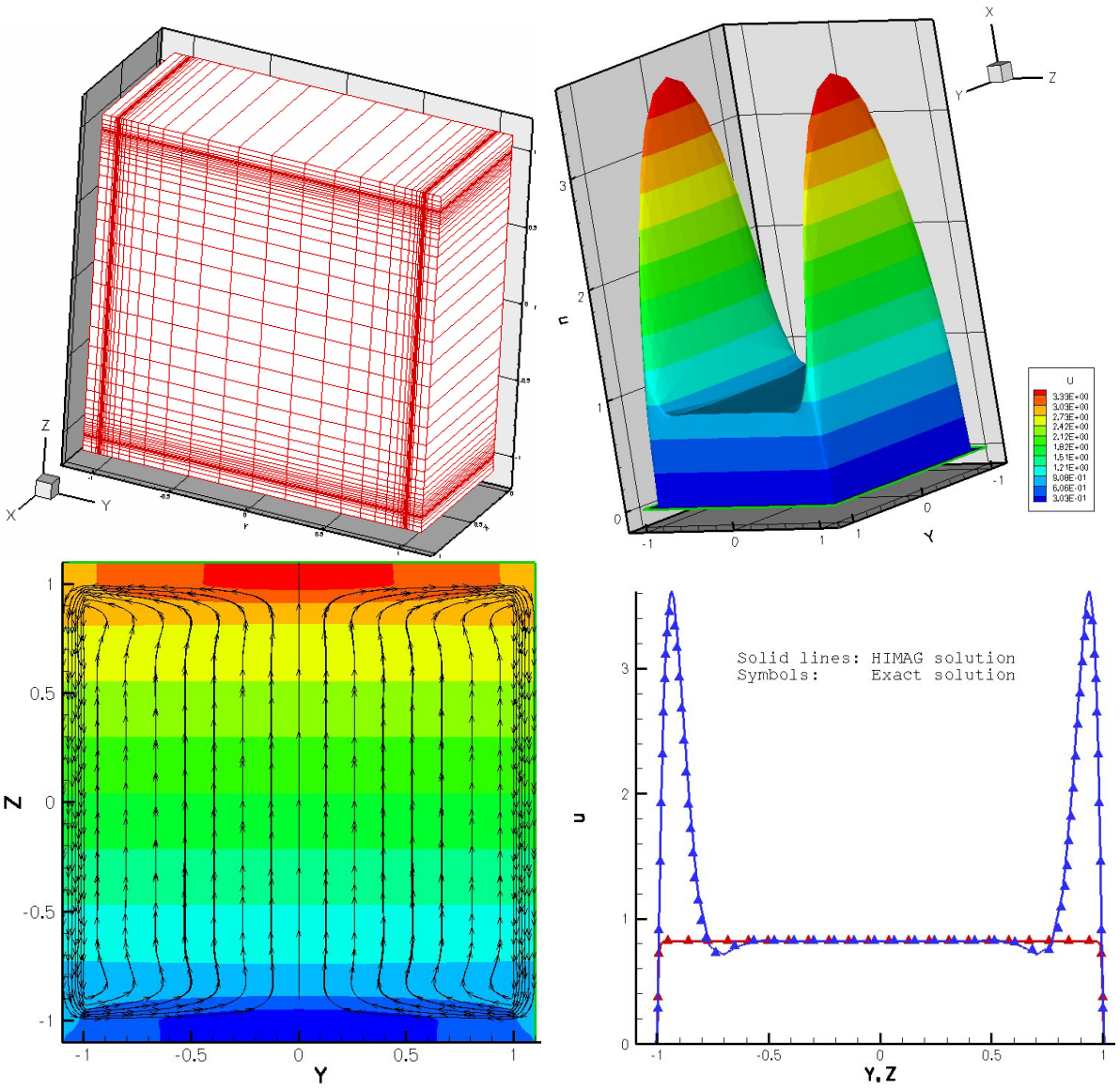


**Figure 2:** Sample results. Mesh used, velocity profile, potential contours with current lines and comparison with Hunt's exact solution